Unraveling the Chemical Nature of the 3D "Hollow" Hybrid Halide Perovskites

Ioannis Spanopoulos[†], Weijun Ke[†], Constantinos C. Stoumpos[†], Emily C. Schueller[||], Oleg Y. Kontsevoi[§], Ram Seshadri[||] and Mercouri G. Kanatzidis*[,†]

[†]*Department of Chemistry, Northwestern University, Evanston, IL 60208, United States*

[||]*Materials Research Laboratory, Materials Department, and Department of Chemistry and Biochemistry, University of California, Santa Barbara, CA 93106, United States*

[§]*Department of Physics and Astronomy, Northwestern University, Evanston, IL 60208, United States*

ABSTRACT

The newly introduced class of 3D halide perovskites, termed "hollow" perovskites, has been recently demonstrated as light absorbing semiconductor materials for fabricating lead-free perovskite solar cells with enhanced efficiency and superior stability. Hollow perovskites derive from three-dimensional (3D) AMX_3 perovskites (A = methylammonium (MA), formamidinium (FA); M = Sn, Pb; X = Cl, Br, I) where small molecules such as ethylenediammonium cations (*en*) can be incorporated as the dication without altering the structure dimensionality. We present in this work the inherent structural properties of the hollow perovskites and expand this class of materials to the Pb-based analogues. Through a combination of physical and spectroscopic methods (XRD, gas pycnometry, ^{1}H-NMR, TGA, SEM/EDX), we have assigned the general formula $(A)_{1-x}(en)_x(M)_{1-0.7x}(X)_{3-0.4x}$, to the hollow perovskites. The incorporation of *en* in the 3D perovskite structure leads to massive M and X vacancies in the 3D [MX_3] framework, thus the term hollow. The resulting materials are semiconductors with significantly blue-shifted direct band gaps from 1.25-1.51 eV for Sn-based perovskites and from 1.53-2.1 eV for the Pb-based analogues. The increased structural disorder and hollow nature were validated by single crystal X-ray diffraction analysis as well as pair distribution function (PDF) analysis. Density functional theory (DFT) calculations support the experimental trends and suggest that the observed widening of the band gap is attributed to the massive M and X vacancies which create a less connected 3D hollow structure. The resulting hollow materials have superior air stability, where in the case of Sn-based hollow perovskites it exceeds two orders of temporal magnitude compared to the conventional full perovskites of $MASnI_3$ and

FASnI$_3$. The hollow perovskite compounds pose as a new platform of highly promising light absorbers that can be utilized in single junction or tandem solar cells.

Keywords: optoelectronic materials, photoluminescence, air stability, photovoltaics

INTRODUCTION

Perovskite based photovoltaic solar cells have emerged recently as excellent light absorbers, with unique inherent optoelectronic properties. Among the numerous synthetic perovskite compounds, halide perovskites, with general formula *AMX$_3$* (A = Cs$^+$, CH$_3$NH$_3$$^+$, HC(NH$_2$)$_2$$^+$; M = Ge^{2+}, Sn^{2+}, Pb^{2+} ; X = Cl$^-$, Br$^-$, I$^-$) have been tested extensively and successfully for the assembly of devices with high power conversion efficiencies (PCEs).[1-3] Their high absorption coefficients,[4] high charge-carrier mobilities,[5] long carrier diffusion lengths,[6] and low recombination losses,[7] have allowed solution-based fabrication of devices with record verified energy conversion efficiencies higher than 22%.[8-9]

Recent high throughput computational studies evaluating the electronic properties of hundreds of stable *AMX$_3$* perovskites, revealed that only the optoelectronic properties of lead and tin compounds are unmatched.[10-13] Out of all the lead based perovskites the hybrid inorganic-organic MAPbI$_3$ (MA = methylammonium) and FAPbI$_3$ (FA = formamidinium) materials have achieved the highest photovoltaic performance.[14-15] In pursuing the quest of a single junction device assembly that could reach eventually the theoretical Shockley-Queisser PCE limit of 31%,[16-18] there is a plethora of studies exploiting different synthetic methodologies and strategies to enhance the electronic properties of those hybrid compounds. Most of them involve the use of a mixture of cations (MA, FA, Cs), anions (Br, I) or a combination of them, as additives in the structure. In the case of (FAPbI$_3$)$_{1-x}$(MAPbBr$_3$)$_x$ material, Jeon et al. have used a mixture of FAPbI$_3$ and MAPbBr$_3$ as the light absorbing layer in a solar cell reaching a PCE of 18%,[19] Li et al. was able to achieve a certified PCE of 19.6% by using a mix cation and anion compound formulated as FA$_{0.81}$MA$_{0.15}$PbI$_{2.51}$Br$_{0.45}$,[20] Zong et al. fabricated a perovskite film containing a mixture of cations (FA, Cs, Pb and Sn) with a subsequent formula (FAPbI$_3$)$_{1-x}$(CsSnI$_3$)$_x$, which gave rise to a device with a PCE of 14.6%,[21] while Saliba et al. fabricated a film containing three A site cations (Cs, MA, FA) formulated as Cs$_x$(MA$_{0.17}$FA$_{0.83}$)$_{(100-x)}$Pb(I$_{0.83}$Br$_{0.17}$)$_3$ where the corresponding

device achieved a PCE of 21%.[22]

On the other hand, tin hybrid halide compounds $FASnI_3$ and $MASnI_3$ have been proposed as an ideal replacement of their lead counterparts as light absorbing layers in solar cells.[23-24] Although promising, as they are the top performers among all lead-free halide candidates, the Sn^{2+} analogues (desired as lead-free low toxicity alternatives[25]) have been less successful in demonstrating commercially viable photovoltaic efficiencies (up to 9%),[26] due to the instability of the metal towards oxidation and the consequent problems associated with tuning the electronic band alignment in devices.[27-28]

Towards this end, our group and others have shown that the device performance can be substantially improved by using small molecules such as ethylenediammonium cations (*en*) as additives.[29-30] The original intent of adding *en* in the solutions of $MASnI_3$ and $FASnI_3$ was to improve the morphology of the deposited films and achieve surface passivation. We did not expect the *en* cation to be incorporated to the *AMX₃* structure because its size is too large and violates the geometric tolerance factor rules regarding 3D perovskite structure stabilization. Despite this, the addition of *en* in these solutions does result in deposited films with the 3D perovskite structure that in fact contain *en* in the lattice.[31] When *en* gets incorporated as the dication in the perovskite structure, it causes *M* and *X* atoms to be expelled from the structure, forming large discontinuities in the perovskite lattice, producing a highly disrupted "hollow" perovskite structure. The irregularly connected perovskite framework leads to blue shift in the bandgap, proportional to the loading of *en* in the material, in a similar fashion with the reduced dimensionality perovskites due to the elimination of several *M-X* connections. Unlike the 2D perovskites, the "hollow" perovskites retain their isotropic three-dimensional (3D) structure, which is beneficial for fabricating electronic devices.

In this work, we report a detailed structural and physical characterization of the *en*-based hollow iodide perovskites and investigate the special physical properties of this novel class of perovskite materials. We formulate the hollow perovskites as $(A)_{1-x}(en)_x M_{1-0.7x} X_{3-0.4x}$, where x is the amount of *en* incorporated in the perovskite and was determined from ^1H-NMR measurements. Hereon for convenience by *en* we mean the dication of ethylene diamine i.e. $[NH_3CH_2CH_2NH_3]^{2+}$. We describe three different types of materials based on $MASnI_3$ $((MA)_{1-x}(en)_x(Sn)_{1-0.7x}(I)_{3-0.4x})$, $MAPbI_3$ $((MA)_{1-x}(en)_x Pb_{1-0.7x} I_{3-0.4x})$, and $FAPbI_3$ $((FA)_{1-x}(en)_x(Pb)_{1-0.7x}(I)_{3-0.4x})$. We studied these systems for various amounts of ethylene diamine (*en*) ranging between x = 0-44%

loading. Above a certain *en* loading the perovskites undergo nondestructive structural transitions between the cubic α-phase and the tetragonal β-phase while retaining the 3D motif. Using a broad range of experimental techniques including single crystal X-ray diffraction, ^{1}H-NMR, pycnometry, energy dispersive X-ray spectroscopy (EDX), thermogravimetric analysis (TGA) and Pair Distribution Function (PDF) analysis we show that the continuity of the 3D perovskitic frameworks of all compounds is disrupted by massive *M* and I vacancies. Such vacancies are not known to exist in the pristine MAMI$_3$ and FAMI$_3$ (M = Sn, Pb) materials. The missing *M* and I atoms create hollow space which is then filled by the extra *en* cations, which occupy space in the *A* site, but because of their longer length than MA and FA, they protrude into the space of the vacant *M* sites. Density Functional (DFT) theory calculations suggest the disruption of *MX*$_3$ perovskite continuity leads to significant bandgap widening in both the Pb and Sn analogs. All compounds have significantly blue-shifted bandgaps which directly correlate to the *en* loadings between (0-44%) (such as 2.1 eV for (MA)$_{1-x}$(*en*)$_x$(Pb)$_{1-0.7x}$(I)$_{3-0.4x}$) the largest ever observed for a 3D lead iodide perovskite).[32-33] Importantly, the Sn-based hollow perovskites with high *en*-loading, exhibit unmatched air stability, maintaining their compositional integrity in air for more than one week.

RESULTS AND DISCCUSSION

Synthetic Aspects

      All three families of the (A)$_{1-x}$(*en*)$_x$M$_{1-0.7x}$X$_{3-0.4x}$ perovskites were synthesized using a HI/H$_3$PO$_2$ solvent mixture, that can produce uniform and high quality single crystals. Especially in the case of conventional MASnI$_3$ compounds, the presence of H$_3$PO$_2$ is essential as it prevents the formation of Sn^{4+} moieties.[34] Their presence could alter the stoichiometry of the reaction and lead to the formation of SnI$_4$ and black MA$_2$SnI$_6$ crystals that are impossible to separate from the main product. Their existence can be identified through powder X-ray diffraction (PXRD) measurements, as peaks at $2\theta = 12.6^0$ and 14.6^0 for MA$_2$SnI$_6$ and $2\theta = 25.1^0$ for SnI$_4$, start to appear upon exposure of the tin compounds to air.[35-37]

      During synthesis optimization, we found that the order of the addition of the reactants, as well as their concentration in the reaction media is crucial for obtaining hollow perovskites. The ratios of the starting materials are based on the stoichiometric formula, targeting the *AMX*$_3$ compositions. The targeted nominal *en*:*A*:*M* ratios were in

the range of: (0.1-1):1:1. Addition of higher amounts of *en* leads to the co-precipitation of light-colored secondary byproducts, identified by single-crystal diffraction to be the ethylenediammonium iodide, *en*I_2, and ethylenediammonium lead iodide, *en*PbI_4·$2H_2O$, for the cases of Sn- and Pb-based perovskites, respectively. In the case of *en*I_2 the molecular structure is 0D and consists of single I atoms that are charge balanced by ethylenediammonium cations (Figures S1 and Table S1). In the case of *en*PbI_4·$2H_2O$ the structure consists of 1D $[PbI_4]^{2-}$ chains, that are separated and charge balanced by ethylenediammonium cations. Water molecules also reside in the structure (Figures S2 and Table S1). Interestingly this structure is totally different to the previously reported compound $(en)_2PbBr_6$, which consists of fragmented 2D layers of corner-sharing $[PbBr_6]^{4-}$ octahedra separated by ethylenediammonium cations and free bromine anions, that are charge balancing the structure, residing between the fragments.[38] The maximum amount of *en* that was incorporated in the structure was found not to exceed x = 0.44, obtained for the $(MA)_{0.56}(en)_{0.44}(Pb)_{0.692}(I)_{2.824}$ composition. Initially, the metal source was dissolved in the boiling solvent mixture, followed by the addition of *en*. If the perovskitizer (A-site cation that can stabilize the perovskite structure) is added before *en*, then the pristine compounds are formed instantly and the addition of *en* has no effect on the already formed perovskite crystals. Upon addition of the perovskitizer (MA or FA) to the hot reaction solution, black crystals form immediately, while uniform red or orange crystals are formed upon cooling of the reaction solution. The color of the crystals, $(MA)_{1-x}(en)_x(Pb)_{1-0.7x}(I)_{3-0.4x}$, x = 0.35-0.44 and $(FA)_{1-x}(en)_x(Pb)_{1-0.7x}(I)_{3-0.4x}$, x = 0.39, depends on the amount of *en*, and the metal ion. When an amount of *en* with x ≥ 0.35 is incorporated in the framework it triggers a color change from black to red and orange (Tables S2-S4). Note that the color change only occurs in the Pb perovskites as only in that instance is the band gap change large enough to cause this effect (see below).

In the case of $(MA)_{1-x}(en)_x(Sn)_{1-0.7x}(I)_{3-0.4x}$ six analogs were synthesized with *en* loading x = 0.05, 0.09, 0.21, 0.24, 0.36, 0.40. Uniform black crystals of α-$MASnI_3$ (non-centrosymmetric tetragonal structure, *P4mm* space group, or as centrosymmetric cubic structure, *Pm-3m* space group) were obtained in all cases.[39] Six $(FA)_{1-x}(en)_x(Pb)_{1-0.7x}(I)_{3-0.4x}$ analogues were synthesized with *en* concentrations x = 0.07, 0.11, 0.21, 0.27, 0.29, 0.39. Following the established synthetic methodology for the isolation of the conventional pristine perovskite α-$FAPbI_3$ (non-centrosymmetric orthorhombic structure, *Amm2* space group, or centrosymmetric cubic structure, *Pm-3m* space

group),[39] yellow crystals of the δ-FAPbI$_3$ perovskitoid phase were initially precipitated,[40] which were subsequently converted to the black α-phase upon further heating at the solvent's boiling point. Removing the black crystals from the hot solution, using suction filtration, and drying them in an oven at 110 ^{0}C, enabled the stabilization of the pristine black α phase of FAPbI$_3$ at room temperature for more than 1 week (Figure S3), while absence of the heat treatment step can lead to swift transformation to the yellow δ-phase in 24 hours.[41-42] Unlike the pristine perovskite FAPbI$_3$, addition of *en* in the reaction medium gave rise to stable, uniform, black (FA)$_{1-x}$(*en*)$_x$(Pb)$_{1-0.7x}$(I)$_{3-0.4x}$ crystals in up to x = 0.29 *en* loading. The presence of *en*, even in a small amount as x = 0.07, stabilizes the α-phase of FAPbI$_3$ (i.e. (FA)$_{0.93}$(*en*)$_{0.07}$(Pb)$_{0.951}$(I)$_{2.972}$). Interestingly, by increasing the amount of *en* to x = 0.39, red crystals of the β-phase (non-centrosymmetric tetragonal structure, *P4bm* space group, or as centrosymmetric tetragonal structure, *P4/mbm,* space group) precipitate. Regarding the (MA)$_{1-x}$(*en*)$_x$(Pb)$_{1-0.7x}$(I)$_{3-0.4x}$ hollow perovskites, we examined six *en* loadings with, x = 0.03, 0.10, 0.29, 0.35, 0.40 and 0.44. At room temperature the stable MAPbI$_3$ phase is the tetragonal β-phase (tetragonal structure, *I4/mcm* space group).[43] The presence of *en* dication enables the stabilization of the α-MAPbI$_3$ phase at room temperature (non-centrosymmetric tetragonal structure, *P4mm* space group, or as centrosymmetric cubic structure, *Pm*-3*m* space group). We observed that *en* loadings higher than 0.10 gave rise to uniform black α-MAPbI$_3$ crystals. Remarkably, at x = 0.35-0.40 *en* loading, the α-MAPbI$_3$ phase precipitates as uniform red crystals, while in the case of x = 0.44 *en* the crystals were orange (Figure 1b).

The phase purity of the resulting materials was confirmed by X-ray powder diffraction (PXRD). All (MA)$_{1-x}$(*en*)$_x$(Sn)$_{1-0.7x}$(I)$_{3-0.4x}$ perovskites have exactly the same PXRD pattern and are isostructural to the pristine α-MASnI$_3$ material (x = 0) (Figure 1a). PXRD studies of the (FA)$_{1-x}$(*en*)$_x$(Pb)$_{1-0.7x}$(I)$_{3-0.4x}$ compounds verified their uniform phase and purity. For x values up to 0.29 the hollow perovskites are isostructural to the pristine α-FAPbI$_3$, whereas at x = 0.39 the appearance of additional diffraction peaks at 2θ = 22.3^0 and 26.4^0 are characteristic of the formation of the pure β-FAPbI$_3$ (Figure S4). (MA)$_{1-x}$(*en*)$_x$(Pb)$_{1-0.7x}$(I)$_{3-0.4x}$ hollow perovskites crystallize at the β phase for x = 0-0.10, while for x values up to 0.44 all materials are isostructural to the pristine α-MAPbI$_3$. This is clear by the disappearance of the diffraction peak at 2θ = 23.7^0, which is characteristic of the β phase MAPbI$_3$, giving rise to uniform α-MAPbI$_3$ crystals (Figure S5). The calculated PXRD patterns of the single crystal structures are presented

for comparison to the experimental ones from the hollow perovskites (Figures S6, S7). Except for the evaluation of phase purity, PXRD measurements revealed that there is a gradual expansion in the unit cell volume with increasing amount of *en* in the structure. Indexing of the PXRD patterns of all materials shed light to this observation in all cases (Figures S8-S10 and Tables S2-S4).

The highest amount of *en* loading found among all of the hollow perovskites was for orange $(MA)_{0.56}(en)_{0.44}(Pb)_{0.692}(I)_{2.824}$. For the Pb-based compounds, x values above 0.35 of *en* incorporation in the structure was critical for the formation of red crystals. However, in the case of Sn hollow perovskites, with x values up to 0.40 in the crystal structure, there was no deposition of red crystals since the wider bandgap is still ~1.51 eV. All $(MA)_{1-x}(en)_x(Sn)_{1-0.7x}(I)_{3-0.4x}$ crystals are black and form immediately upon addition of the perovskitizer, while the red $(MA)_{1-x}(en)_x(Pb)_{1-0.7x}(I)_{3-0.4x}$ and $(FA)_{1-x}(en)_x(Pb)_{1-0.7x}(I)_{3-0.4x}$ crystals form after some time, when the solution gets cooler. The remarkable fact in the chemistry presented above is that the dication of *en* is not known to stabilize the 3D perovskite AMX_3 structure. The compound $enPbI_4·2H_2O$ does not have a perovskite structure (Figure S2) and the analogous compound $enSnI_4$ has not yet been reported.

The presence of *en* in the crystal structure and the exact amount of *en* loading in a given composition was determined by ^{1}H-NMR spectroscopy, by dissolving the crystals of all the $(A)_{1-x}(en)_x M_{1-0.7x}X_{3-0.4x}$ materials in a polar solvent and determining the cations ratios based on their NMR signatures. The quantification is based on both the methyl ($-CH_3$, $\delta = 2.39$ ppm) and the ammonium ($-NH_3^+$, $\delta = 7.49$ ppm) protons of the methylammonium cation versus the methylene ($-CH_2-$, $\delta = 3.02$ ppm) and the ammonium ($-NH_3^+$, $\delta = 7.77$ ppm) protons of the ethylenediammonium (*en*) cations. In methylammonium, the integration of those peaks reveals a ratio of 1:1, since there are three protons from the methyl group ($-CH_3$) and three protons from the amine cation ($-NH_3^+$). In ethylenediammonium, the ratio of the 2 peaks is 4:6, arising from four $-CH_2-$ protons and six ammonium ($-NH_3^+$) protons, suggesting that *en* is doubly protonated in solution. Under the current synthetic conditions, in the highly acidic environment (57% HI) it is unlikely that only one amine group would be protonated. We expect therefore that indeed ethylenediamine was double protonated, in the structure, before dissolution of the crystals in DMSO-d$_6$. The same methodology was used for all samples. The ^{1}H NMR spectra are presented in figures S11-S30 whereas the resulting compositions are tabulated in Table 1.

Scanning electron microscopy (SEM) imaging revealed that the morphology of the crystals also changes upon incorporation of *en* (Figure 2 and Figures S31-S32). The pristine full perovskite materials (x = 0) exhibit the typical rhombic dodecahedral morphology, whereas all *en* containing crystals appear as regular octahedra. The octahedral morphology observed here in the hollow perovskites is unprecedented. Interestingly, it has been observed in perovskite oxides.[44] To the best of our knowledge, this is the first time this crystal morphology is observed in 3D halide perovskites and it possibly constitutes one of the signature characteristics of hollow perovskites. The octahedral morphology requires the growth of the perovskite to occur along its body diagonal ((111) direction in the cubic aristotype), driven by the organization of the cations residing at the *A*-site. The involvement of the *A*-site cations in the crystal growth of the hollow perovskites suggests that the solids tend to terminate their surface at the *en* cations, thereby helping to improve the stability of the perovskites towards humidity in a similar fashion to the two-dimensional (2D) halide perovskites which tend to terminate at the organic spacers (see below).

Air stability

The incorporation of *en* into the perovskite structure imparts a remarkable improvement in air stability in the tin systems. For example, the $(MA)_{0.6}(en)_{0.4}(Sn)_{0.72}(I)_{2.84}$ composition is stable for at least 9 days at ambient atmosphere. As shown in Figure 1c, the PXRD pattern of the highly hollow perovskite after 9 days in air is exactly the same with the fresh as made sample with no traces of crystalline decomposition products. However, after 16 days in air, traces of crystalline decomposition products start to form, as small diffraction peaks, which do not belong to the α-MASnI$_3$ crystal structure, appear at 2θ values of 12.5^0, 22^0, 29^0 and 42^0. For comparison, the compound $(MA)_{0.76}(en)_{0.24}(Sn)_{0.832}(I)_{2.904}$ which incorporates approximately half the amount of *en* in the framework, is stable in air for ~1 day only, Figure 1d. In this case decomposition products start to appear on the second day, based on the PXRD measurements, whereas the pristine MASnI$_3$ analogue itself starts to decompose after 10 minutes of air exposure (see Figure S33). The enhanced air stability is partly also attributed to the "dilution" of the Sn^{2+} ion content and the disconnected nature of the perovskite framework, which presumably slows down the oxidation kinetics. The markedly improved air stability appears to be a common feature of the hollow perovskites. Weiss et al. have synthesized MASnI$_3$ films that were stable for

half an hour in air and after 20 days being stored in a nitrogen filled glove box,[45] while Lee et al. reported $FASnI_3$ based devices that maintained their performance after 100 days exposure in air for an encapsulated device.[46] To the best of our knowledge, the air stability of $(MA)_{1-x}(en)_x(Sn)_{1-0.7x}(I)_{3-0.4x}$ appears to be the highest so far among all the $ASnX_3$ perovskites,[47-48] either in single crystal form or as deposited films.

In the case of the red $(FA)_{0.61}(en)_{0.39}(Pb)_{0.727}(I)_{2.844}$ crystals, PXRD measurements revealed that the material is stable in air for 300 days so far, stabilized at the β phase (Figure S34). This stability is unparalleled for a 3D $FAPbI_3$ phase, as the most stable, heat treated, α phase maintains its integrity in air for around 7 days[49] or more than 8 days in our case (see Figure S3).

Regarding the orange crystals of $(MA)_{0.56}(en)_{0.44}(Pb)_{0.692}(I)_{2.824}$ compound, PXRD measurements revealed that the material is stable in air for less than 330 days (Figure S35), as an additional diffraction peak at $2\theta = 11.9^0$ and another one, appearing as a "shoulder" at $2\theta = 20^0$ coming from crystalline decomposition by-product/s appeared. The resulting air stability is among the highest reported for single $MAPbI_3$ crystals[50] and far superior than $MAPbI_3$ thin films.[51-52]

Structural properties

A good empirical rule of thumb to check whether the *en* cation can be incorporated in the 3D structure of the AMX_3 perovskites without deforming it, is the approximation of the Goldschmidt's tolerance factor (t)[53-54] for the hollow perovskites. The tolerance factor is defined as $t = (r_{(A)} + r_{(X)})/\sqrt{2}(r_{(M)} + r_{(X)})$ where $r_{(A)}$, $r_{(M)}$ and $r_{(X)}$ are the ionic radii of the constituent A-, M- and X-site ions respectively. According to the model proposed by Kieslich et al,[55] we estimated that the effective radius of *en* is 3.33 Å. The respective ionic radii of $MA^+ = 2.17$ Å, $FA^+ = 2.53$ Å,[55] $Pb^{2+} = 1.03$ Å, $Sn^{2+} = 0.97$ Å[56] and $I^- = 2.20$ Å .[57] If the *en* dication occupies exclusively the *A* site then the tolerance factor will be $t = 1.21$ and 1.23 for the Pb and Sn perovskites respectively. These values largely deviate from the perovskite forming range of $0.8 < t < 1.0$ required for the acquisition the 3D perovskite structure.[58] Indeed, in the case of $enPbI_4 \cdot 2H_2O$, the structure is composed of 1-D $[PbI_3]^-$ chains that are separated and charge balanced by *en* dications (Figure S2). In the case of hollow perovskites there are 2 different A site cations. Therefore, the calculated t factors for $(MA)_{0.6}(en)_{0.4}(Sn)_{0.72}(I)_{2.84}$, $(FA)_{0.61}(en)_{0.39}(Pb)_{0.727}(I)_{2.844}$ and $(MA)_{0.56}(en)_{0.44}(Pb)_{0.692}(I)_{2.824}$ are $t = 1.08$, 1.10 and

1.07 respectively, which also lay outside the optimum range for the 3D perovskite acquisition. However, in our case single crystal and powder X-ray diffraction analysis verifies the 3D nature of all synthesized materials. This means that the structure, in order to maintain its dimensionality, had to replace some A and/or B and/or I site atoms to accommodate the large *en* molecules, which is supported by the results of the rest of the characterization techniques used in this work.

The crystal structure of selected hollow perovskites was determined by single-crystal X-ray diffraction. The crystallographic parameters are shown in Table 2, and the detailed structural information is given in tables S5-20. As mentioned above, the X-ray powder diffraction patterns indicate that all these compounds retain the 3D structure of the pristine perovskite, having only small differences in the respective lattice parameters which tend to increase due to the lattice expansion caused by the inclusion of *en* in the unit cell (see above).

The presence of *en* in the lattice could not be crystallographically detected because of disorder and mixed occupancy with the MA and FA cations. Since we couldn't resolve the mixed occupancy of the organic cations, only the major MA or FA components were modeled in the structure refinement as has been done previously in the refinement of conventional perovskites.[39] The local structure within a single unit cell is also very characteristic for the chemical properties of each individual perovskite (Cs-, MA- or FA-based), with parameters such as octahedral titling and octahedral distortion being particularly relevant for the semiconducting properties of each perovskite. In this aspect, the local structure, represented by the non-centrosymmetric assignments, is also valuable and we choose it intentionally in order to better illustrate the chemical environment of the perovskite unit. This option allows the structural resolution of the organic molecules without disorder. This is a chemically intuitive model which captures well the static structure of the perovskite; however, as typically done when refining $MAPbI_3$ and $FAPbI_3$ structures[39] which exhibit dynamic disorder, the position of the cations was averaged out leading to a dynamic centrosymmetric structure.

In order to probe the vacancies in the structures, we refined the occupancy of all heavy atoms freely while keeping the occupancy of the A-site cations to 1. The refinements clearly show that the occupancies of Pb atoms are well below the full levels required by the ideal crystal structure. In Table 3, the occupancy refinement results are summarized, along with some indicative refinement statistics. Initially, only the

occupancy of the Pb atoms was refined, column A. The resulting refined occupancy was much less than unity in all cases (down to 0.74). This large decrease was accompanied by a significant improvement of the refinement statistics, up to 37% lower R_{obs} values, columns D and E. When all I atoms (I1, I2) were refined individually (columns B, C), while keeping the Pb occupancy to 1, physically meaningless results were obtained, since the iodide occupancy increased to values >1 in all cases. In a third refinement scenario the occupancies of the lead and iodide atoms were refined simultaneously. This gave unrealistic occupancies down to 0.41 for Pb and 0.47 decrease for the total I content arising from too many correlated refinable parameters. However, the formation of I atom vacancies, in addition to *M* vacancies, cannot be excluded and this issue will be examined in the following sections, using methods that rely on the properties of the bulk material and not a single crystal (see below).

The presence of massive heavy atom vacancies in the inorganic perovskite framework is a new structural configuration for perovskites. The excess positive charges introduced from the incorporation of *en* evidently are compensated by the elimination of M^{2+} atoms which result in discontinuities in the 3D framework. A related example was only seen very recently in the ordered-vacancy structures of "hollow", deficient d-MAPbI$_3$ where the hydoxy-ethylalmmonium cations (HEA)$^+$ selectively substitute (PbI)$^+$ units to create octahedral holes in the lattice,[59] and in the mixed-valent compound $[H_3N(CH_2)_7NH_3]_8(MA)_2(Sn^{4+})(Sn^{2+})_{12}I_{46}$ reported by Guan et al., where heptamethylenediamine resides in ordered defect sites in the lattice; the latter is only enabled by the partial oxidation of the perovskite lattice.[60] In both these cases the resulting defects in the structure are ordered and can be identified crystallographically, whereas in the case of "hollow" perovskites the resulting defects are highly disordered and randomly oriented in the perovskite structure.

$(FA)_{0.61}(en)_{0.39}(Pb)_{0.727}(I)_{2.844}$ adopts the β-phase and crystalizes in the tetragonal space group, *P4bm*. It has a larger normalized unit cell volume (261.0(1) Å^3) than the pristine β-FAPbI$_3$ (249.1(3) Å^3). It is based on in-phase tilted [PbI$_6$] octahedra with Pb-I-Pb angles 171^0 and 169^0 along the ab plane and c-axis, respectively. Furthermore, there is a discernible difference in the Pb-I bond lengths. In the pristine β-phase the Pb-I bond distances are 3.1624(12) Å and 3.1741(14) Å along the ab plane and c-axis, respectively, whereas in the hollow β-phase these values are longer at 3.169(12) Å and 3.229(3) Å, respectively.

Taking a closer look at the single crystal structure of the hollow MAPbI$_3$ material with the highest *en* loading, (MA)$_{0.56}$(*en*)$_{0.44}$(Pb)$_{0.692}$(I)$_{2.824}$, it is clear that it is the α-MAPbI$_3$ perovskite structure type. The unit cell dimensions are larger than the pristine α-MAPbI$_3$, since the hollow one has larger normalized unit cell volume (255.1(2) Å^3) than the pristine one (251.60(2) Å^3). As in the case of FAPbI$_3$, the Pb-I bond lengths are elongated in the hollow material with values of 3.172(3) Å along the ab plane and 3.237(12) Å along the c axis, compared to the pristine one with values of 3.1559(10) Å and 3.213(3) Å respectively.

A remarkable feature of the hollow perovskites is that they can induce compositionally-controlled structural phase transitions based on the MA/*en* and FA/*en* ratio (Figure 3). Interestingly, *en* incorporation into the framework can stabilize the β-FAPbI$_3$ at RT (298 K) which was reported to be stable below 250 K,[39, 61] and the α-MAPbI$_3$ which is stable at high temperatures (>330 K).[62-63] The phase transition for MAPbI$_3$ progresses from the initial tetragonal β-phase (*I4/mcm* space group) to the α-phase (non-centrosymmetric tetragonal structure, *P4mm* space group, or as centrosymmetric cubic structure, *Pm-3m* space group) above an *en* loading of x = 0.10 (Figure S5). The transition is aided both by the expansion of the perovskite lattice as well as the increasing degree of disorder in the structure, introduced by the displacement of the inorganic framework components by the *en* dication. A similar compositionally induced transition could be observed when HI was used as an additive in the fabrication of MAPbI$_3$ films.[64] Conversely, FAPbI$_3$ starts as a metastable α-phase (non-centrosymmetric orthorhombic structure, *Amm*2 space group, or centrosymmetric cubic structure, *Pm-3m* space group), adopts the stable α-phase for small *en* loading, and upon further *en* loading (x = 0.39) it converts to the tetragonal β-phase (non-centrosymmetric structure, *P4bm* space group, or as centrosymmetric structure, *P4/mbm,* space group) (Figure S4). This paradoxical behavior of FAPbI$_3$, which tends to "lock" to a lower symmetry structure as the degree of structural disorder increases, highlights the different nature of the MA and FA cations. The different dynamics in the structure derive from the different shape of the two cations, with the linear MA cations preferring to oscillate along tetragonal axis (β-phase), whereas the more rigid, bent FA cations favors a configurational disorder along all three dimensions (α-phase).[65] These effects are amplified by the additional disorder introduced by *en*.

Hollow perovskites have lower density

Another independent method we used to assess the content of *en* in the solids and the "hollowness" of the structure was gas pycnometry, using He as the gas displacement medium.[66] Using the $(MA)_{1-x}(en)_x(Sn)_{1-0.7x}(I)_{3-0.4x}$ series as an example, we found that the density of the solids decreases systematically as a function of (x), starting from $\rho = 3.640$ (1) g cm^{-3} for the pristine full perovskite to $\rho = 3.255(1)$ g cm^{-3} for the x = 0.40 composition, corresponding to an overall 11% decrease (Figure 4a). Such a drastic decrease cannot by accounted for by a simple substitution of two MA molecules with one *en* cation since the mass difference in this case is negligible. Therefore, it becomes evident that *en* indeed displaces part of the heavy atoms in the inorganic framework, including both Sn^{2+} and I^- ions. This is a logical result, since it is unlikely that a large cation such as *en* can fit in the perovskite cage without a compensating mechanism allowing its accommodation in the structure. Theoretical calculations also support this hypothesis (see below). The same trend was also observed for the Pb analogs with maximum *en* loading, reaching a 12% and 15% density decrease for $(FA)_{0.61}(en)_{0.39}(Pb)_{0.727}(I)_{2.844}$ (Figure S36) and $(MA)_{0.56}(en)_{0.44}(Pb)_{0.692}(I)_{2.824}$ (Figure 4b), respectively (Tables S29-S31). A perspective of how this hollow structure could be envisioned is shown in Figure 5.

Based on the above results, we can formulate the general composition of the materials. However, there are several chemical formula possibilities to consider. For example, it is possible to conceive compositions where all M^{2+} is displaced by en^{2+} in a stoichiometric manner, or where en^{2+} displaces two MA^+ molecules and a neutral MX_2 unit. In order to estimate which chemical compositions describe best the preponderance of experimental results we have cross-tested ten possible chemical formulae that could potentially arise from the incorporation of *en* in the hollow perovskites and compared them with the combined array of experimental results. The theoretical density of each compound, ρ_{calc}, was calculated by using the molecular weight of the formula and the volume of the unit cell that was determined from indexing the powder XRD patterns. In all cases the charge of *en* is considered to be (2+), based on the ^{1}H-NMR spectra, while in one case we examined also the possibility to be (+1). In order to compare efficiently the results of the ten proposed formulas and select the most accurate one for our materials, an arbitrary crystal density difference value, that works as a threshold limit had to be introduced. For that purpose, a difference between the calculated and experimental crystal density ($\rho_{calc} - \rho_{exp}$) above 0.1 g cm^{-3} was set to be the cut off limit.

The formula which had the fewest compounds below this limit was considered to be the most representative and correct one. By implementing this rule, of all the ten formulas only three seemed to be the most promising, each one describing different possible substitution mechanisms (Tables S32-41). The first one, is formula number 8 in Table 4, namely (A)$en_{(x)}$M$_{(1-x)}$I$_3$. In this case en replaces only M^{2+} cations in the structure, no A^+ and no I$^-$ moieties. Using this formula only two materials out of the eighteen were above the threshold limit of 0.1 g cm^{-3} between the calculated and the experimental crystal density. The corresponding crystal density difference values of the rest of the compounds was lower than the threshold limit, and exhibited standard deviations of σ = 0.049 g cm^{-3}, 0.047 g cm^{-3} and 0.067 g cm^{-3} for the MA$en_{(x)}$Sn$_{(1-x)}$I$_3$, MA$en_{(x)}$Pb$_{(1-x)}$I$_3$ and FA$en_{(x)}$Pb$_{(1-x)}$I$_3$ families of materials respectively (Table S38). However, if we take a closer look at the 3D structure of a AMI$_3$ perovskite (Figure 3), then it is highly unlikely for an en molecule to replace only M^{2+} ions in the structure, since due to its larger size than the M^{2+} ions (see effective radii above), it cannot fit in the position of an M^{2+} ion without deforming the 3D structure. This can only be possible by the additional removal of either an A^+ cation (en orientation vertical to the inorganic M-I-M chains, Figure 5) or a I$^-$ ion (en molecule orientation across the inorganic M-I-M chains). The second examined formula of Table 4, is formula number 9, namely A$_{(1-x/2)}$$en_{(x/2)}M_{(1-x/2)}I_{(3-x/2)}$, where en replaces I$^-$, M^{2+} and A^+ equally. Under this formulation only one material exhibited an unacceptably large difference of 0.1 g cm^{-3} between the calculated and the experimental crystal density. All other materials match pretty well, with calculated standard deviations of σ = 0.031 g cm^{-3}, 0.043 g cm^{-3} and 0.061 g cm^{-3} for the MA$_{(1-x/2)}$$en_{(x/2)}Sn_{(1-x/2)}I_{(3-x/2)}$, MA$_{(1-x/2)}$$en_{(x/2)}Pb_{(1-x/2)}I_{(3-x/2)}$ and FA$_{(1-x/2)}$$en_{(x/2)}Pb_{(1-x/2)}I_{(3-x/2)}$ families of materials respectively (Table S39).

The third most suitable formula of Table 4, is formula number 10, namely A$_{(1-x)}$$en_{(x)}M_{(1-0.7x)}I_{(3-0.4x)}$, where en replaces A^+ equally and in lower amounts the I$^-$, and M^{2+} ions. In this case en addition can replace M^{2+} ions, A^+ organic cations, MI$_2$ and MAI moieties in a statistical manner in any combination that can afford a charge balanced compound. Interestingly, the crystal density difference for all materials was below the threshold density limit, exhibiting a very good agreement among the calculated and the experimental crystal densities (Table S41), surpassing in match the previous two formulas (formulas number 8 and 9).

Based on the fact that with this formula the calculated crystal densities of the eighteen materials, exhibit the best match with the experimental determined ones and

resembles a reasonable structural configuration of *en* in the framework, we chose this formula as the most precise one to describe the hollow perovskites. This conclusion is further supported by the fact that those results are based on the combination of three independent measurements (PXRD, NMR and crystal density), which are based on the bulk materials' properties and not a mere single crystal. Therefore the optimized charged balanced chemical formulae for each family are the following: $(MA)_{1-x}(en)_x(Sn)_{1-0.7x}(I)_{3-0.4x}$, $(MA)_{1-x}(en)_x(Pb)_{1-0.7x}(I)_{3-0.4x}$, $(FA)_{1-x}(en)_x(Pb)_{1-0.7x}(I)_{3-0.4x}$ (this work) and $(FA)_{1-x}(en)_x(Sn)_{1-0.7x}(I)_{3-0.4x}$ from our previous work.[31]

The above conclusions are also consistent with energy-dispersive X-Ray spectroscopy (EDX) analysis measurements which show that the I/Pb ratio, which is close to 3 for the pristine material, shifts closer to 4 for the hollow materials (Figure S37 and Table S42) showing the metal deficiency of the hollow compounds. Noticeably based on the proposed formula for the most hollow $(FA)_{0.61}(en)_{0.39}(Pb)_{0.727}(I)_{2.844}$, the calculated ratio I/Pb is 3.91 which is close to experimental one of 4.06, while for the $(MA)_{0.56}(en)_{0.44}(Pb)_{0.692}(I)_{2.824}$ calculated ratio I/Pb is 4.08 which is almost the same with the experimental one of 4.11 (Table S42). Thermogravimetric analyses (TGA) are also in agreement with those results. All $(MA)_{1-x}(en)_x(Sn)_{1-0.7x}(I)_{3-0.4x}$ perovskites show two distinct decomposition steps at ~300 ^{0}C and ~400 ^{0}C (Figures S38-42). The first weight loss corresponds to the decomposition of the organic part of the perovskite; that is MAI in the case of pristine compound, or MAI and *en*I_2 in the case of the hollow perovskites. The second step corresponds to the evaporation of the inorganic part of the structure, SnI_2. The mass loss at the first step increases gradually from 45% weight loss in the pristine MASnI$_3$, to 55.7% for the x = 0.36 member. Similarly, the inorganic weight loss step gradually decreases from 50.3% to 42.3% respectively (Table S43). The Pb-based perovskites show analogous behavior with FAPbI$_3$ hollow perovskites exhibiting a mass loss from 28.5% for x = 0 to 41.4% for x = 0.39 at ~330 ^{0}C and from 71.5% to 48.7% at ~450 ^{0}C (Figures S43-48 and Table S44). MAPbI$_3$ hollow analogues follow a similar trend (Figures S49-55 and Table S45). Those results clearly verify that with increasing amount of *en* in the structure the organic part increases and the inorganic part is diminished, consistent with vacancies induced by the entry of *en* dications.

PDF measurements

Pair distribution function (PDF) analysis is a widely used and established method for characterizing the atomic-scale structure of materials that exhibit limited structural coherence.[67-68] The synchrotron powder X-ray diffraction patterns for pristine β-MAPbI$_3$ and MAPbI$_3$ with x = 0.44 amount of *en* added, were compared with the intent of elucidating the effect of *en* addition on the structure. Other techniques (PXRD, NMR and density measurements) suggest the formula (MA)$_{0.56}$(*en*)$_{0.44}$(Pb)$_{0.692}$(I)$_{2.824}$ for the highest doped sample, which has vacancies on every site. However, due to the reduced scattering factors of the organic species compared to the inorganic lattice and correlations between refined parameters, the formula was only refined with vacancies on the Pb-site as those seemed to fit the scattering data the best. Therefore, while the molecular formula is likely to be (MA)$_{0.56}$(*en*)$_{0.44}$(Pb)$_{0.692}$(I)$_{2.824}$, in this analysis the *en* doped sample from XRD will be referred to as (MA)(*en)*$_x$(Pb)$_{1-x}$(I)$_3$ to represent the parameters that were actually refined. The extra peaks in the (MA)(*en)*$_x$(Pb)$_{1-x}$(I)$_3$ sample, indicated by "x" marks, come from a small (approximately 8%) *en*PbI$_4$ impurity. All materials were best fit by the prototypical *I*4/*mcm* room-temperature structure of pristine MAPbI$_3$ (due to dynamic disorder, high-symmetry centrosymmetric space groups were used that do not orient the *A*-site cations). Refinement of Pb occupancy indicates that Pb is leaving the structure upon addition of *en*. Pb occupancy is highly correlated with the scale factor as Pb is the largest element in the system and therefore contributes the most to the X-ray scattering, making determination of exact occupancy difficult. However, estimated standard deviations suggest that some level of Pb vacancy is real with an approximate occupancy of 0.8 at an *en* fraction of 0.44. Furthermore, the lower intensity of peaks and the faster decay of signal with Q for the hollow MAPbI$_3$ sample (Figure 6a), compared to the pristine MAPbI$_3$ (Figure 6d), imply a high level of disorder in the *en* containing sample. Similarly, from the PDF data, the lower intensity and broader peaks in the PDF pattern of the hollow material (Figure 6b) compared to the pristine one (Figure 6e) are indicative of its more disordered local structure. The peaks around 6.3 and 8.9 Å change noticeably upon doping and correspond to Pb-Pb peaks in the PDF, further corroborating disorder and/or vacancies on the Pb site. This can be viewed more clearly in the partial Pb-Pb PDF, which dramatically decreases in intensity and significantly broadens upon doping in the case of the hollow material (Figure 6f, green line), compared to the pristine one (Figure 6c, green line). Because the area under the curve in the partial PDF corresponds to the

total number of Pb-Pb pair correlations, the lower integrated intensity of the partial PDF for the hollow compound (Figure 6f) compared to the pristine one (Figure 6c) indicates a decrease of Pb in the system with the addition of *en*. The I-I partial PDFs do not change as much as the Pb-Pb partials upon doping (Figures 6f and c, red lines). This is partly because the occupancy of the I atoms was not refined. However, in the case of the I-I partial PDF the peaks of the hollow material are not significantly broadened compared to the pristine one, indicating that the I site is less disordered upon *en* addition than the Pb site. Overall, the reciprocal and real-space diffraction data suggest the *en* substitution is inducing disorder in the system and, more specifically, affecting the Pb site of the material. Due to previously mentioned constraints, a more specific mechanism for *en* substitution cannot be determined from X-ray diffraction alone. The *en*-substituted FAPbI$_3$ materials, analyzed in the Supporting Information, show the same trends as MAPbI$_3$, although without the formation of a detectable impurity phase (Figure S56).

Optical absorption and photoluminescence

Optical absorption spectra for all the hollow perovskites show that with increasing amount of *en* the band gap shifts to higher energy values (Figure 7). At the maximum *en* loading in the framework we observed a ~40% increase in the energy bandgap. The parameter that controls the optical properties in 3D perovskite compounds is s/p orbitals overlap among the metal and the halide ions.[69] This overlap relates directly to the *M-X-M* φ angle. However the shape and the nature of the A cation(s) can indirectly affect this angle causing distortions to the metal octahedra.[70] As it has been reported previously with decreasing φ angle the band gap increases and this trend is observed also during phase transitions, from α to γ and δ phases.[71] Especially in the case of MAPbI$_3$ during its phase transitions over a wide temperature range (4.2 K to 400 K) the observed blue shift in the bandgap is relatively small (0.08 eV difference) and it arises from thermal expansion.[72] This effect is more pronounced (0.58 eV difference) during the compositionally induced phase transitions and it is attributed to the disruption of the crystal lattice by *en* and possibly due to an "emphanisis-like" behavior (strongly amplified by *en* incorporation) rather than a thermal expansion mechanism of the band gap widening.[73] As *en* is incorporated in the structure and *M* and I atoms are removed from the 3D framework, they create discontinuities in the *M-X-M-X* bridges as they are replaced by *M-X-vacancy-X*

moieties. Because of the presence of a large number of these M^{2+} and I^- vacancies the orbital overlap among the remaining M/X atoms is reduced and as a consequence the widths of the VBM and CBM narrow, leading to the experimentally observed increase in the bandgap.[31] This is explained in detail below in the band structure calculations section.

All the eighteen (18) hollow perovskite compounds presented in this work are direct band semiconductors as it was verified by the sharp band edge in the absorption spectra and DFT calculations (see below). $(MA)_{1-x}(en)_x(Sn)_{1-0.7x}(I)_{3-0.4x}$ materials exhibit band gaps ranging from 1.25 eV to 1.51 eV for x values starting from 0.05 to 0.40 (Figure 7b). For the $(MA)_{1-x}(en)_x(Pb)_{1-0.7x}(I)_{3-0.4x}$ materials the band gaps increase from 1.56 eV to 2.1 eV for x values spanning from 0.03 to 0.44 (Figure 7a). Similarly, the $(FA)_{1-x}(en)_x(Pb)_{1-0.7x}(I)_{3-0.4x}$ hollow perovskites revealed bang gaps in the range of 1.53 eV to 1.94 eV for x values from 0.07 to 0.39 (Figure S57). This corresponds to a significant increase of ~20%, ~40% and ~35% in the band gap energy, respectively. The band gap trend is reflected in the crystal color change from black to red and orange observed for the Pb-based hollow perovskites. A similar color change was observed in the case of the dimensionally reduced 2D Ruddlesden-Popper $(BA)_2(MA)_{n-1}Pb_nI_{3n+1}$ perovskites, where by decreasing the number of inorganic layers, from $n = \infty$ (MAPbI$_3$) to $n = 1$ ((BA)$_2$PbI$_4$) an analogous change in the crystal color is observed.[74] However, in the case of the hollow perovskites the 3D structure is maintained and the band gap increase is attributed to the "hollowing out" of the perovskite framework which is a form of aperiodic dimensional reduction of the crystal lattice.

The hollow perovskites exhibit photoluminescence (PL) at room temperature that is blue shifted with increasing fraction of en (Figure 7), which is consistent with the presented bandgap trends. Photoluminescence is an important property for photovoltaic applications, as an optimum light absorbing candidate should not only absorb light efficiently but also emit light in the same manner.[75] Interestingly the red and orange crystals of compounds $(MA)_{1-x}(en)_x(Pb)_{1-0.7x}(I)_{3-0.4x}$ and $(FA)_{1-x}(en)_x(Pb)_{1-0.7x}(I)_{3-0.4x}$ exhibit no PL for reasons we refer to below. All the Sn-based analogues exhibit strong PL emission that cover a range from 991 nm for the pristine MASnI$_3$ to 718 nm for the $(MA)_{0.6}(en)_{0.4}(Sn)_{0.72}(I)_{2.84}$ (Figure 7d). The PL emission peak of the pristine compound (no en) is centered at 1.25 eV, which matches the band gap energy (1.21 eV) from the absorption spectrum, in agreement with what was reported in the

literature.[76] With increasing fraction of *en* the two values start to diverge significantly reaching a maximum absorption/emission energy difference of 0.22 eV for the $(MA)_{0.6}(en)_{0.4}(Sn)_{0.72}(I)_{2.84}$ composition, revealing an above band gap photoluminescence (Table 5 and Figure S58). Taking into account that this material contains the highest amount of *en* among all hollow perovskites, it is likely that due to the existence of a large number of defects, there could be some spatially confined domains in the structure that cause lattice strain, and give rise to stable excitonic states.[77-78] Those states can contribute to the increase of the energy of the emission spectrum.

The Pb-based analogs exhibit a similar blue shift with increasing amount of *en*, accompanied by an analogous divergence between the absorption/emission energy. The PL peak maxima of the $(FA)_{1-x}(en)_x(Pb)_{1-0.7x}(I)_{3-0.4x}$ perovskites range between 799 nm for the pristine α-FAPbI$_3$ to 678 nm for the $(FA)_{0.71}(en)_{0.29}(Pb)_{0.797}(I)_{2.884}$ (Figure S59). Likewise, the PL peaks of the $(MA)_{1-x}(en)_x(Pb)_{1-0.7x}(I)_{3-0.4x}$ compounds range between 766 nm for the pristine β-MAPbI$_3$ to 644 nm for $(MA)_{0.65}(en)_{0.35}(Pb)_{0.755}(I)_{2.86}$ (Figure 7c). In both cases, all Pb based materials exhibit an above band gap PL, with a maximum energy difference of 0.12 eV and 0.13 eV for $(FA)_{0.71}(en)_{0.29}(Pb)_{0.797}(I)_{2.884}$ and $(MA)_{0.65}(en)_{0.35}(Pb)_{0.755}(I)_{2.86}$ respectively, which is significantly smaller than that observed for the Sn-based hollow perovskite (0.22 eV), which contains much higher amount of *en* (Table 5 and Figures S60-61). The blue shift of the PL emission relative to the bandgap is a known phenomenon in Pb halide perovskites. It can be associated with surface lattice strain that cause energetic inhomogeneity across the crystal,[79-81] while in other cases it was ascribed to the recombination via a bound exciton involving halide vacancy defects.[82] It is therefore reasonable to observe a similar trend in the hollow perovskites, since they contain a large number of random oriented defects.

The unusual feature of the PL in hollow perovskites is that with increasing *en* loading, the intensity gradually diminishes and vanishes (at room temperature) for the materials with x > 0.35, Figures 7c and f. All $(FA)_{0.61}(en)_{0.39}(Pb)_{0.727}(I)_{2.844}$, $(MA)_{0.6}(en)_{0.4}(Pb)_{0.72}(I)_{2.84}$ and $(MA)_{0.56}(en)_{0.44}(Pb)_{0.692}(I)_{2.824}$ compositions exhibit no light emission. This could be attributed to the special crystal growth of the hollow perovskites (along (111) direction, see above) which exposes specifically the A-site cations at the crystal edges. The presence of significant amounts of *en* in the crystal surface leads to an effective disconnection of the perovskite structure which may be responsible for the loss of PL emission when the local concentration of *en* at the surface

exceeds a certain limit. Because of the disorder in the structure, the presence of charged point defects, that may act as nonradiative recombination centers (traps), cannot be ruled out. Furthermore, the absence of PL emission may be attributed to phonon quenching by the large number of vacancies, as it was observed in the case of vacancy ordered double perovskite Cs_2SnI_6 reported by Maughan et al, although in this case the oxidation state of Sn is (4+).[83]

Electronic band structure DFT calculations

To gain further insights regarding the origin of the band gap opening in the hollow perovskites we performed theoretical band structure calculations using $FAPbI_3$ as the model system. The initial configuration was represented by the 2x2x2 supercell of the conventional orthorhombic unit cell ($Amm2$, $Z = 2$, $FA_{16}Pb_{16}I_{48}$ composition) of α-$FAPbI_3$ corresponding to the lowest energy structure of a similar compound, $FASnI_3$.[31] In order to mimic the hollow perovskite structures we constructed two hollow structures from the same supercell by removing one or two PbI_2 units creating neutral vacancy sites, which can be occupied by *en* cations (being represented by FA in the calculations). The corresponding compositions were $(FA)_{16}Pb_{16}I_{48}$, $(FA)_{16}Pb_{15}I_{46}$, and $(FA)_{16}Pb_{14}I_{44}$, respectively. The calculated trend in the band gap (Figure 8) shows that as metal halide fragments are eliminated from the perovskite structure and the effective dimensionality decreases, the bands themselves become less disperse (i.e. narrower) due to the reduced lengths of fragments with *M-X* overlap. Therefore, the band gaps increase proportionally to the eliminated Pb and I atoms, in which in the actual hollow perovskite systems, it occurs as the *en* content increases. This is the same trend that was observed previously in the case of hollow $(FA)_{1-x}(en)_x(Sn)_{1-0.7x}(I)_{3-0.4x}$ system. Despite the elimination of the MI_2 units, the nature of the band gap does not change and it remains direct in the case of the hollow perovskites as well. The calculated band gaps and trends capture well the experimental observations in the absorption spectra of all hollow compounds.

CONCLUSIONS

The dication of *en* is not known to stabilize the 3D perovskite AMX_3 structure yet we see that it seemingly does. The only compound characterized is enPbI$_4$·2H$_2$O (see SI) which does not have a perovskite structure. If the hollow perovskites presented

above were mere analogs of the AMX_3 materials (A= MA, FA, Cs), where the A cations were partially replaced by *en* then we would expect only minor changes in the optical properties. The fact that variable amounts of *en* can enter the structure and dramatically change the bandgaps but retain the overall 3D perovskite structure suggests that we have a new way to manipulate their intrinsic properties without changing the dimensionality to a 2D or making mixed solid solutions among the halides (e.g. I/Br). Since we have gone beyond Cs, MA and FA and have demonstrated the introduction of a fourth cation in the 3D structure and at the same time created a family of perovskites that can dramatically change their optical properties in a controlled and systematic manner, we regard the hollow perovskites a new type of perovskite rather than as analogs of the known AMX_3 materials. Apparently, the incorporation of *en* in the 3D perovskite AMX_3 lattice violates the tolerance factor rules which generally are pretty well obeyed in the halides. The materials accomplish this by generating space for the larger *en*, by removing *M* and *X* moieties from their structure. We have formulated these compounds as $(A)_{1-x}(en)_x(M)_{1-0.7x}(X)_{3-0.4x}$ where the small *en* cation disrupt the perovskite lattice by displacing molecular fragments out of the 3D structure. The consequences from this subtle change are macroscopic effects in the semiconducting properties of the perovskites, opening up of the band gap by up to 0.6 eV observed for x ~ 0.44. The increased organic content and unique morphology of the crystals lend the hollow perovskites remarkably improved air stability possibly by slowing down that decomposition kinetics, as seen in the case of $(MA)_{0.6}(en)_{0.4}(Sn)_{0.72}(I)_{2.84}$ where stability exceeds 9 days, compared to any 3D $ASnI_3$ perovskite system which tend to last for mins or hours. The present work sheds new light to the chemistry of the hollow perovskites, which we regard here as a new category of perovskite materials separate from the normal 3D AMX_3 versions. These materials open new horizons in applying 3D perovskites in various optoelectronics applications.

Finally, an intriguing question that arises from the above results is why do the MAMX_3 and FAMX_3 systems themselves not generate hollow structures by compensating with the loss of M atoms (e.g. $MA_{1+x}Pb_{1-x/2}I_3$) and instead require a second cation such as *en* to do so. Or do they? Is it possible that some of the literature observations regarding MAPbI$_3$ and FAPbI$_3$, such as slight blue shift of the bandgap from their expected value or PL shift, are caused by difficult to detect by PXRD, hollow $MA_{1+x}Pb_{1-x/2}I_3$ versions? One indication for such a scenario may come from careful and accurate X-ray crystal structure refinements of the atomic occupancies and

experimental measurements of the crystal density. Future experiments aimed at achieving deeper understanding of perovskites should focus on exploring such possibilities.

ASSOCIATED CONTENT

Supporting Information

Materials and methods, synthetic details, computational details, additional supplementary figures and tables about material characterization, SEM images, EDX spectra, X-ray diffraction measurements, absorption spectroscopy measurements, photoluminescence measurements, ^{1}H-NMR Spectroscopy & crystal density measurements, determination of chemical formulae, thermogravimetric analysis and crystallographic tables.

This material is available free of charge via the Internet at http://pubs.acs.org.

AUTHOR INFORMATION

Corresponding Authors

m-kanatzidis@northwestern.edu

Notes

The authors declare no competing financial interest.

REFERENCES

1. Marshall, K. P.; Walker, M.; Walton, R. I.; Hatton, R. A., *Nat. Energy* **2016,** *1*, 16178.
2. Edri, E.; Kirmayer, S.; Cahen, D.; Hodes, G., *J. Phys. Chem. Lett.* **2013,** *4*, 897.
3. Krishnamoorthy, T.; Ding, H.; Yan, C.; Leong, W. L.; Baikie, T.; Zhang, Z.; Sherburne, M.; Li, S.; Asta, M.; Mathews, N.; Mhaisalkar, S. G., *J. Mater. Chem. A* **2015,** *3*, 23829.
4. De Wolf, S.; Holovsky, J.; Moon, S.-J.; Löper, P.; Niesen, B.; Ledinsky, M.; Haug, F.-J.; Yum, J.-H.; Ballif, C., *J. Phys. Chem. Lett.* **2014,** *5*, 1035.
5. Ponseca, C. S.; Savenije, T. J.; Abdellah, M.; Zheng, K.; Yartsev, A.; Pascher, T.; Harlang, T.; Chabera, P.; Pullerits, T.; Stepanov, A.; Wolf, J.-P.; Sundström, V., *J. Am. Chem. Soc.* **2014,** *136*, 5189.
6. Stranks, S. D.; Eperon, G. E.; Grancini, G.; Menelaou, C.; Alcocer, M. J. P.; Leijtens, T.; Herz, L. M.; Petrozza, A.; Snaith, H. J., *Science* **2013,** *342*, 341.
7. Oga, H.; Saeki, A.; Ogomi, Y.; Hayase, S.; Seki, S., *J. Am. Chem. Soc.* **2014,** *136*, 13818.
8. Green, M. A.; Emery, K.; Hishikawa, Y.; Warta, W.; Dunlop, E. D., *Prog. Photovoltaics Res. Appl.* **2016,** *24*, 905.
9. National Renewable Energy Laboratory. Research Cell Record Efficiency Chart, **2018**, https://www.nrel.gov/pv/assets/images/efficiency.
10. Filip, M. R.; Giustino, F., *J. Phys. Chem. C* **2016,** *120*, 166.
11. Chakraborty, S.; Xie, W.; Mathews, N.; Sherburne, M.; Ahuja, R.; Asta, M.; Mhaisalkar, S. G., *ACS Energy Lett.* **2017,** *2*, 837.
12. Ma, Z.-Q.; Pan, H.; Wong, P. K., *J. Electron. Mater.* **2016,** *45*, 5956.
13. Korbel, S. M.; Botti, S.; Marques, M. A. L., *J. Mater. Chem. A* **2018**, DOI: 10.1039/C7TA08992A.
14. Yang, W. S.; Noh, J. H.; Jeon, N. J.; Kim, Y. C.; Ryu, S.; Seo, J.; Seok, S. I., *Science* **2015,** *348*, 1234.
15. Zhou, H.; Chen, Q.; Li, G.; Luo, S.; Song, T.-b.; Duan, H.-S.; Hong, Z.; You, J.; Liu, Y.; Yang, Y., *Science* **2014,** *345*, 542.
16. Shockley, W.; Queisser, H. J., *J. Appl. Phys.* **1961,** *32*, 510.
17. Sha, W. E. I.; Ren, X.; Chen, L.; Choy, W. C. H., *Appl. Phys. Lett.* **2015,** *106*, 221104.
18. Henry, C. H., *J. Appl. Phys.* **1980,** *51*, 4494.
19. Jeon, N. J.; Noh, J. H.; Yang, W. S.; Kim, Y. C.; Ryu, S.; Seo, J.; Seok, S. I., *Nature* **2015,** *517*, 476.
20. Li, X.; Bi, D.; Yi, C.; Décoppet, J.-D.; Luo, J.; Zakeeruddin, S. M.; Hagfeldt, A.; Grätzel, M., *Science* **2016**.
21. Zong, Y.; Wang, N.; Zhang, L.; Ju, M.-G.; Zeng, X. C.; Sun, X. W.; Zhou, Y.; Padture, N. P., *Angew. Chem. Int. Ed.* **2017,** *56*, 12658.
22. Saliba, M.; Matsui, T.; Seo, J.-Y.; Domanski, K.; Correa-Baena, J.-P.; Nazeeruddin, M. K.; Zakeeruddin, S. M.; Tress, W.; Abate, A.; Hagfeldt, A.; Gratzel, M., *Energ Environ Sci* **2016,** *9*, 1989.
23. Hao, F.; Stoumpos, C. C.; Cao, D. H.; Chang, R. P. H.; Kanatzidis, M. G., *Nat Photon* **2014,** *8*, 489.
24. Liao, W.; Zhao, D.; Yu, Y.; Grice, C. R.; Wang, C.; Cimaroli, A. J.; Schulz, P.; Meng, W.; Zhu, K.; Xiong, R.-G.; Yan, Y., *Adv. Mater.* **2016,** *28*, 9333.
25. Babayigit, A.; Ethirajan, A.; Muller, M.; Conings, B., *Nature Mater.* **2016,** *15*, 247.
26. Shao, S.; Liu, J.; Portale, G.; Fang, H. H.; Blake, G. R.; Brink, G. H. t.; Koster, L. J. A.; Loi, M. A., *Adv. Energy Mater.* **2018,** *8*.
27. Wang, F.; Ma, J.; Xie, F.; Li, L.; Chen, J.; Fan, J.; Zhao, N., *Adv. Funct. Mater.* **2016,** *26*, 3417.
28. Kumar, M. H.; Dharani, S.; Leong, W. L.; Boix, P. P.; Prabhakar, R. R.; Baikie, T.; Shi, C.; Ding, H.; Ramesh, R.; Asta, M.; Graetzel, M.; Mhaisalkar, S. G.; Mathews, N., *Adv. Mater.* **2014,** *26*, 7122.
29. Ke, W.; Stoumpos, C. C.; Spanopoulos, I.; Mao, L.; Chen, M.; Wasielewski, M. R.; Kanatzidis, M. G., *J. Am. Chem. Soc.* **2017,** *139*, 14800.
30. Lu, J.; Jiang, L.; Li, W.; Li, F.; Pai, N. K.; Scully, A. D.; Tsai, C.-M.; Bach, U.; Simonov, A. N.; Cheng, Y.-B.; Spiccia, L., *Adv. Energy Mater.* **2017,** *7*, 1700444.
31. Ke, W.; Stoumpos, C. C.; Zhu, M.; Mao, L.; Spanopoulos, I.; Liu, J.; Kontsevoi, O. Y.; Chen, M.; Sarma, D.; Zhang, Y.; Wasielewski, M. R.; Kanatzidis, M. G., *Sci. Adv.* **2017,** *3*.
32. Protesescu, L.; Yakunin, S.; Bodnarchuk, M. I.; Krieg, F.; Caputo, R.; Hendon, C. H.; Yang, R. X.; Walsh, A.; Kovalenko, M. V., *Nano Lett.* **2015,** *15*, 3692.
33. McMeekin, D. P.; Sadoughi, G.; Rehman, W.; Eperon, G. E.; Saliba, M.; Hörantner, M. T.; Haghighirad, A.; Sakai, N.; Korte, L.; Rech, B.; Johnston, M. B.; Herz, L. M.; Snaith, H. J., *Science* **2016,** *351*, 151.

34.   Li, W.; Li, J.; Li, J.; Fan, J.; Mai, Y.; Wang, L., *J. Mater. Chem. A* **2016,** *4*, 17104.

35.   Willey Gerald, R.; Woodman Timothy, J.; Deeth Robert, J.; Errington, W., *Main Group Chem.* **1998,** *21*, 583.

36.   Dang, Y.; Zhou, Y.; Liu, X.; Ju, D.; Xia, S.; Xia, H.; Tao, X., *Angew. Chem., Int. Ed.* **2016,** *128*, 3508.

37.   Liu, X.; Yang, Z.; Chueh, C.-C.; Rajagopal, A.; Williams, S. T.; Sun, Y.; Jen, A. K. Y., *J. Mater. Chem. A* **2016,** *4*, 17939.

38.   Lemmerer, A.; Billing, D. G., *CrystEngComm* **2012,** *14*, 1954.

39.   Stoumpos, C. C.; Malliakas, C. D.; Kanatzidis, M. G., *Inorg. Chem.* **2013,** *52*, 9019.

40.   Kaltzoglou, A.; Stoumpos, C. C.; Kontos, A. G.; Manolis, G. K.; Papadopoulos, K.; Papadokostaki, K. G.; Psycharis, V.; Tang, C. C.; Jung, Y.-K.; Walsh, A.; Kanatzidis, M. G.; Falaras, P., *Inorg. Chem.* **2017,** *56*, 6302.

41.   Saidaminov, M. I.; Abdelhady, A. L.; Maculan, G.; Bakr, O. M., *Chem. Commun.* **2015,** *51*, 17658.

42.   Saidaminov, M. I.; Abdelhady, A. L.; Murali, B.; Alarousu, E.; Burlakov, V. M.; Peng, W.; Dursun, I.; Wang, L.; He, Y.; Maculan, G.; Goriely, A.; Wu, T.; Mohammed, O. F.; Bakr, O. M., *Nat. Commun.* **2015,** *6*, 7586.

43.   Whitfield, P. S.; Herron, N.; Guise, W. E.; Page, K.; Cheng, Y. Q.; Milas, I.; Crawford, M. K., *Sci. Rep.* **2016,** *6*, 35685.

44.   Wu, J.; Xue, D., *CrystEngComm* **2011,** *13*, 3773.

45.   Weiss, M.; Horn, J.; Richter, C.; Schlettwein, D., *Phys. Status Solidi A* **2016,** *213*, 975.

46.   Lee, S. J.; Shin, S. S.; Kim, Y. C.; Kim, D.; Ahn, T. K.; Noh, J. H.; Seo, J.; Seok, S. I., *J. Am. Chem. Soc.* **2016,** *138*, 3974.

47.   Yokoyama, T.; Cao, D. H.; Stoumpos, C. C.; Song, T.-B.; Sato, Y.; Aramaki, S.; Kanatzidis, M. G., *J. Phys. Chem. Lett.* **2016,** *7*, 776.

48.   Song, T.-B.; Yokoyama, T.; Stoumpos, C. C.; Logsdon, J.; Cao, D. H.; Wasielewski, M. R.; Aramaki, S.; Kanatzidis, M. G., *J. Am. Chem. Soc.* **2017,** *139*, 836.

49.   Zhumekenov, A. A.; Saidaminov, M. I.; Haque, M. A.; Alarousu, E.; Sarmah, S. P.; Murali, B.; Dursun, I.; Miao, X.-H.; Abdelhady, A. L.; Wu, T.; Mohammed, O. F.; Bakr, O. M., *ACS Energy Lett.* **2016,** *1*, 32.

50.   Li, W.-G.; Rao, H.-S.; Chen, B.-X.; Wang, X.-D.; Kuang, D.-B., *J. Mater. Chem. A* **2017,** *5*, 19431.

51.   Hoye, R. L. Z.; Brandt, R. E.; Osherov, A.; Stevanović, V.; Stranks, S. D.; Wilson, M. W. B.; Kim, H.; Akey, A. J.; Perkins, J. D.; Kurchin, R. C.; Poindexter, J. R.; Wang, E. N.; Bawendi, M. G.; Bulović, V.; Buonassisi, T., *Chem. Eur. J.* **2016,** *22*, 2605.

52.   Zhang, T.; Meng, X.; Bai, Y.; Xiao, S.; Hu, C.; Yang, Y.; Chen, H.; Yang, S., *J. Mater. Chem. A* **2017,** *5*, 1103.

53.   Goldschmidt, V. M., *Naturwissenschaften* **1926,** *14*, 477.

54.   Green, M. A.; Ho-Baillie, A.; Snaith, H. J., *Nat. Photonics* **2014,** *8*, 506.

55.   Kieslich, G.; Sun, S.; Cheetham, A. K., *Chem. Sci.* **2014,** *5*, 4712.

56.   Travis, W.; Glover, E. N. K.; Bronstein, H.; Scanlon, D. O.; Palgrave, R. G., *Chem. Sci.* **2016,** *7*, 4548.

57.   Li, C.; Lu, X.; Ding, W.; Feng, L.; Gao, Y.; Guo, Z., *Acta Crystallogr., Sect. B* **2008,** *64*, 702.

58.   Li, Z.; Yang, M.; Park, J.-S.; Wei, S.-H.; Berry, J. J.; Zhu, K., *Chem. Mater.* **2016,** *28*, 284.

59.   Leblanc, A.; Mercier, N.; Allain, M.; Dittmer, J.; Fernandez, V.; Pauporté, T., *Angew. Chem., Int. Ed.* **2017,** *56*, 16067.

60.   Guan, J.; Tang, Z.; Guloy, A. M., *Chem. Commun.* **2005**, 48.

61.   Fabini, D. H.; Stoumpos, C. C.; Laurita, G.; Kaltzoglou, A.; Kontos, A. G.; Falaras, P.; Kanatzidis, M. G.; Seshadri, R., *Angew. Chem., Int. Ed.* **2016,** *55*, 15392.

62.   Baikie, T.; Fang, Y.; Kadro, J. M.; Schreyer, M.; Wei, F.; Mhaisalkar, S. G.; Graetzel, M.; White, T. J., *J. Mater. Chem. A* **2013,** *1*, 5628.

63.   Whitfield, P. S.; Herron, N.; Guise, W. E.; Page, K.; Cheng, Y. Q.; Milas, I.; Crawford, M. K., *Sci. Rep.* **2016,** *6*, 35685.

64.   Soe, C. M. M.; Stoumpos, C. C.; Harutyunyan, B.; Manley, E. F.; Chen, L. X.; Bedzyk, M. J.; Marks, T. J.; Kanatzidis, M. G., *ChemSusChem* **2016,** *9*, 2656.

65.   Even, J.; Carignano, M.; Katan, C., *Nanoscale* **2016,** *8*, 6222.

66.   Tamari, S., *Meas. Sci. Technol.* **2004,** *15*, 549.

67.   Jiang, B.; Grande, T.; Selbach, S. M., *Chem. Mater.* **2017,** *29*, 4244.

68.   Young, C. A.; Goodwin, A. L., *J. Mater. Chem.* **2011,** *21*, 6464.

69.   Mosconi, E.; Amat, A.; Nazeeruddin, M. K.; Grätzel, M.; De Angelis, F., *J. Phys. Chem. C* **2013,**

117, 13902.

70.   Motta, C.; El-Mellouhi, F.; Kais, S.; Tabet, N.; Alharbi, F.; Sanvito, S., *Nat. Commun.* **2015,** *6*, 7026.

71.   Stoumpos, C. C.; Kanatzidis, M. G., *Acc. Chem. Res.* **2015,** *48*, 2791.

72.   Quarti, C.; Mosconi, E.; Ball, J. M.; D'Innocenzo, V.; Tao, C.; Pathak, S.; Snaith, H. J.; Petrozza, A.; De Angelis, F., *Energ Environ Sci* **2016,** *9*, 155.

73.   Fabini, D. H.; Laurita, G.; Bechtel, J. S.; Stoumpos, C. C.; Evans, H. A.; Kontos, A. G.; Raptis, Y. S.; Falaras, P.; Van der Ven, A.; Kanatzidis, M. G.; Seshadri, R., *J. Am. Chem. Soc.* **2016,** *138*, 11820.

74.   Stoumpos, C. C.; Cao, D. H.; Clark, D. J.; Young, J.; Rondinelli, J. M.; Jang, J. I.; Hupp, J. T.; Kanatzidis, M. G., *Chem. Mater.* **2016,** *28*, 2852.

75.   Miller, O. D.; Yablonovitch, E.; Kurtz, S. R., *IEEE J. Photovoltaics* **2012,** *2*, 303.

76.   Parrott, E. S.; Milot, R. L.; Stergiopoulos, T.; Snaith, H. J.; Johnston, M. B.; Herz, L. M., *J. Phys. Chem. Lett.* **2016,** *7*, 1321.

77.   Smith, A. M.; Mohs, A. M.; Nie, S., *Nat. Nanotechnol.* **2008,** *4*, 56.

78.   Smith, A. M.; Nie, S., *Acc. Chem. Res.* **2010,** *43*, 190.

79.   Grancini, G.; D'Innocenzo, V.; Dohner, E. R.; Martino, N.; Srimath Kandada, A. R.; Mosconi, E.; De Angelis, F.; Karunadasa, H. I.; Hoke, E. T.; Petrozza, A., *Chem. Sci.* **2015,** *6*, 7305.

80.   Dong, Q.; Fang, Y.; Shao, Y.; Mulligan, P.; Qiu, J.; Cao, L.; Huang, J., *Science* **2015,** *347*, 967.

81.   Galisteo-López, J. F.; Li, Y.; Míguez, H., *J. Phys. Chem. Lett.* **2016,** *7*, 5227.

82.   Sebastian, M.; Peters, J. A.; Stoumpos, C. C.; Im, J.; Kostina, S. S.; Liu, Z.; Kanatzidis, M. G.; Freeman, A. J.; Wessels, B. W., *Phys. Rev. B* **2015,** *92*, 235210.

83.   Maughan, A. E.; Ganose, A. M.; Bordelon, M. M.; Miller, E. M.; Scanlon, D. O.; Neilson, J. R., *J. Am. Chem. Soc.* **2016,** *138*, 8453.
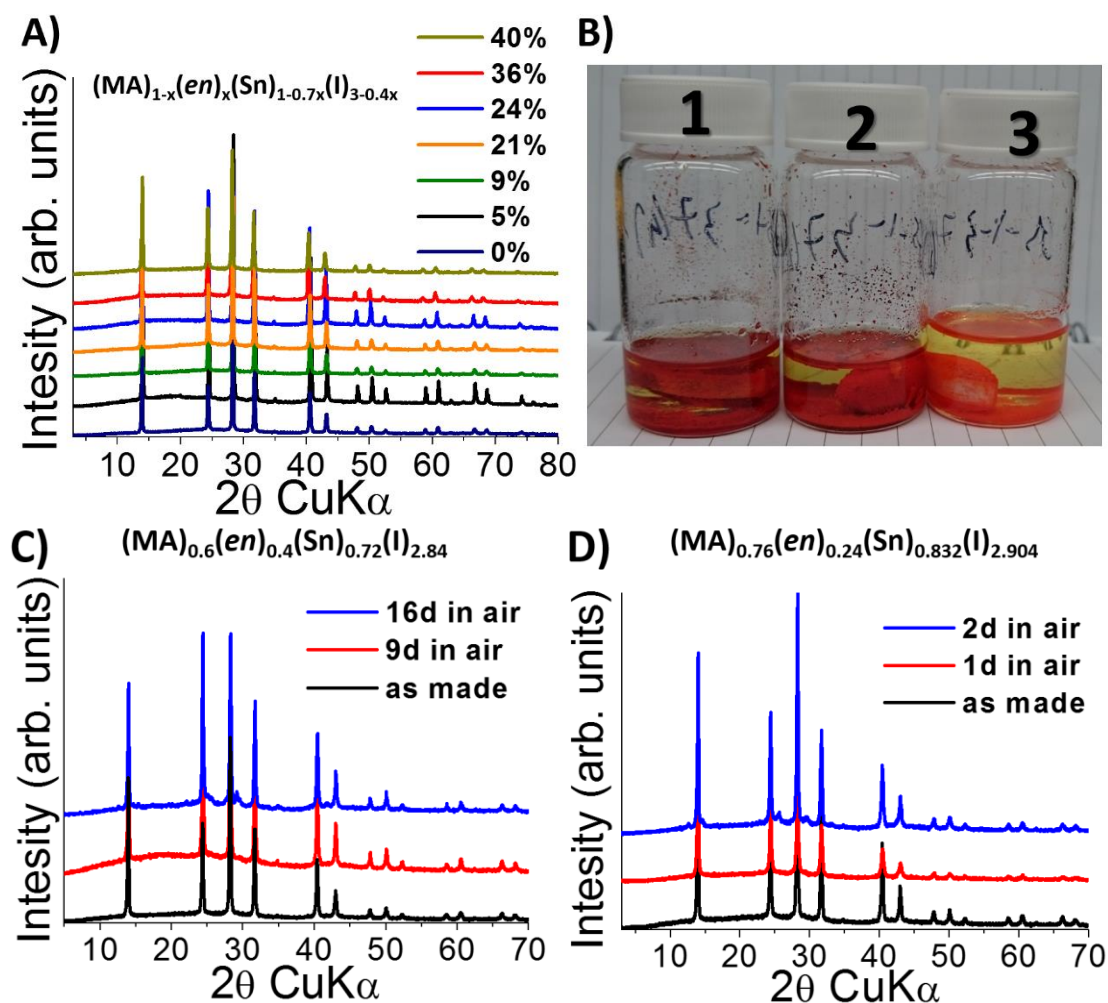
Figures

Figure 1. (A) Comparison of PXRD patterns of the $(MA)_{1-x}(en)_x(Sn)_{1-0.7x}(I)_{3-0.4x}$ compounds with increasing amount of *en* (x). All materials regardless of x-value are isostructural to the conventional, α-MASnI$_3$ pristine perovskite. (B) Photograph of the as made $(FA)_{0.61}(en)_{0.39}(Pb)_{0.727}(I)_{2.844}$ (1), $(MA)_{0.6}(en)_{0.4}(Pb)_{0.72}(I)_{2.84}$ (2) and $(MA)_{0.56}(en)_{0.44}(Pb)_{0.692}(I)_{2.824}$ (3) perovskite crystals. (C), (D) PXRD patterns of the $(MA)_{1-x}(en)_x(Sn)_{1-0.7x}(I)_{3-0.4x}$ compounds (x values 0.40 and 0.24 for *en*) under exposure to air for up to 16 days. The air stability increases with increasing amount of *en* cations in the structure (23 ^{0}C, 30% relative humidity).
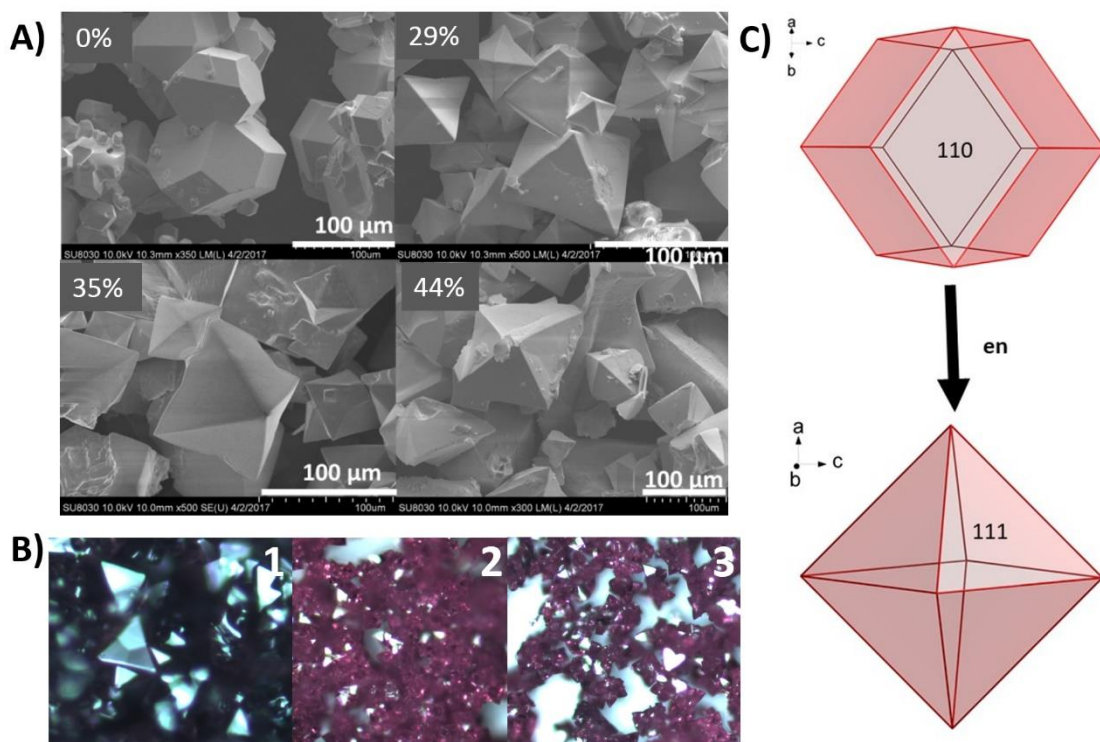
Figure 2. (A) Representative SEM images of compounds $(MA)_{1-x}(en)_x(Pb)_{1-0.7x}(I)_{3-0.4x}$, x = 0, 0.29, 0.35 and 0.44. (B) Optical microscope pictures of compounds $(FA)_{0.71}(en)_{0.29}(Pb)_{0.797}(I)_{2.884}$ (1), $(FA)_{0.61}(en)_{0.39}(Pb)_{0.727}(I)_{2.844}$ (2) and $(MA)_{0.6}(en)_{0.4}(Pb)_{0.72}(I)_{2.84}$ (3). (C) Schematic representation of the perovskite growth in rhombic dodecahedral and octahedral geometries. Relative to the idealized cubic perovskite, in rhombic dodecahedra the face diagonal of the perovskite (110 facets) are exposed, whereas the incorporation of *en* induces the perovskite growth from the body diagonal to expose the (111) facets in the octahedral morphology.
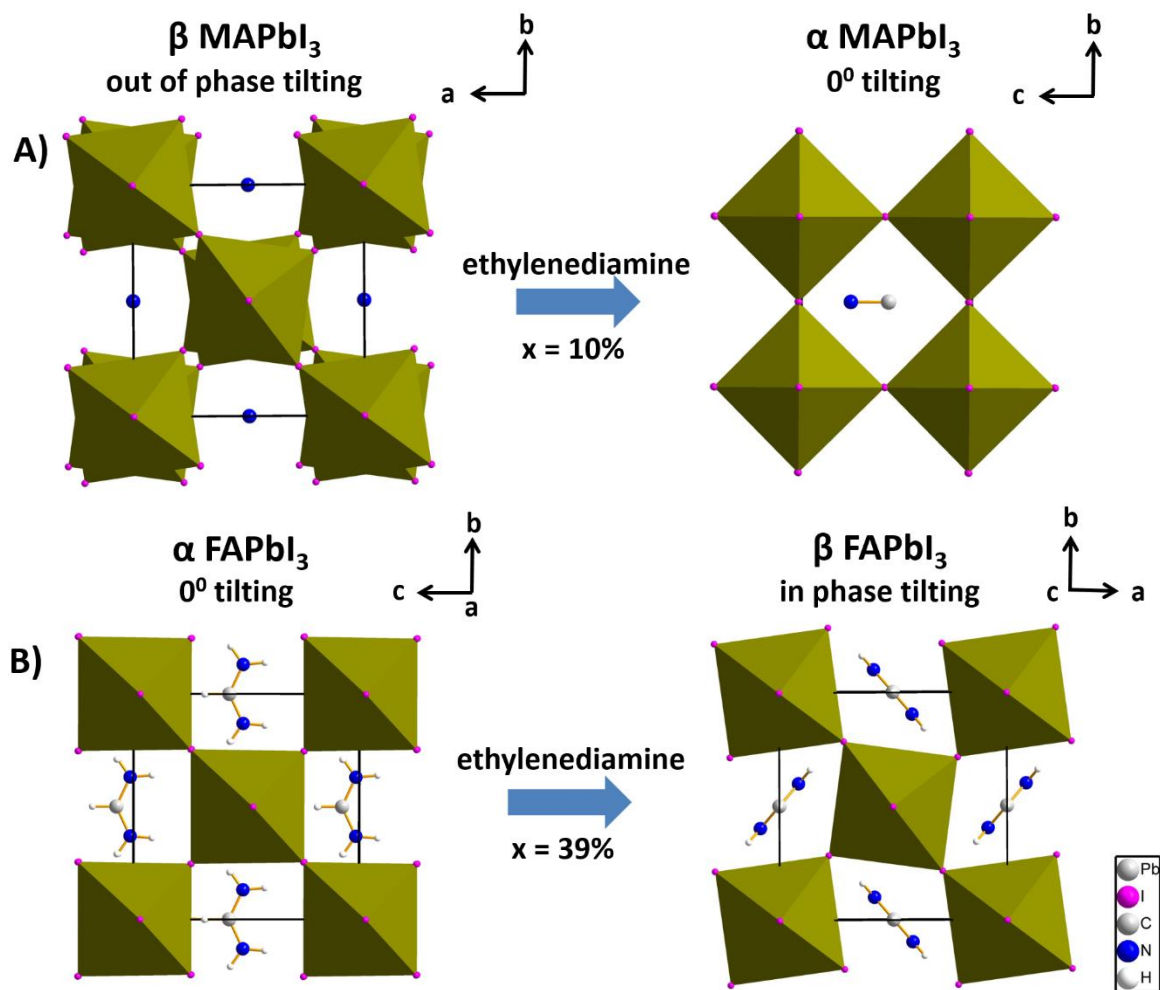
27

Figure 3. Views of the 3D structures of the lead iodide systems highlighting their phase transformations: A) x values higher than 0.10 of *en* into MAPbI$_3$ at RT, leads to a β to α phase transformation, B) whereas x values of 0.39 of *en* into FAPbI$_3$ at RT, leads to an α to β phase transformation.
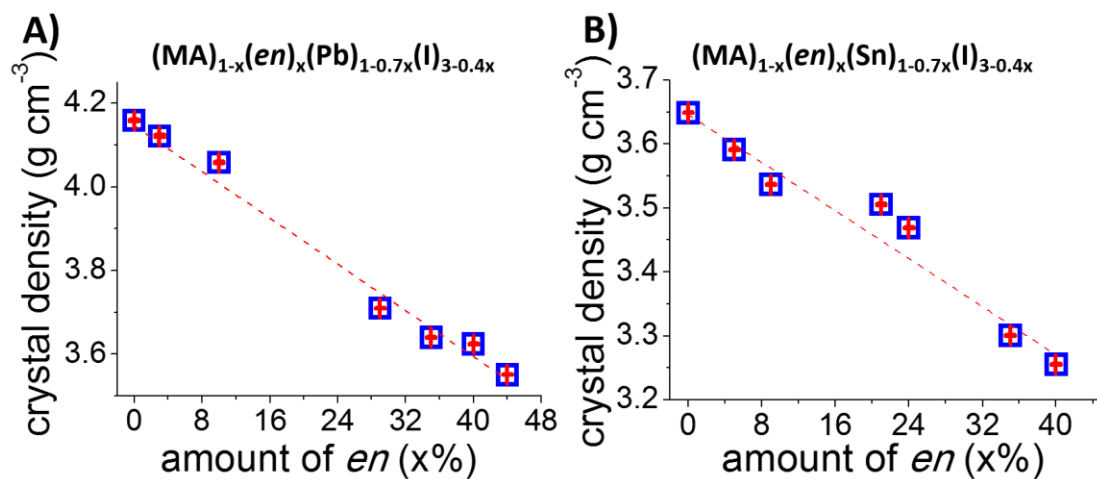
Figure 4. (A) Correlation of the percentage of *en* in $(MA)_{1-x}(en)_x(Pb)_{1-0.7x}(I)_{3-0.4x}$ and (B) $(MA)_{1-x}(en)_x(Sn)_{1-0.7x}(I)_{3-0.4x}$ samples towards the measured crystal density. There is an 15% and 11% decrease in the crystal density of the most hollow material in comparison to the pristine one, respectively (error bars are inside the blue squares).

Figure 5. Schematic illustration of the structure of the 3D pristine $MAPbI_3$ perovskite and its transformation from a dense proper perovskite structure to a hollow 3D structure with increasing amount of *en*. Black cubes: $[PbI_6]$ octahedra, green spheres: MA cations, orange rectangles: ethylenediammonium (*en*) cations.
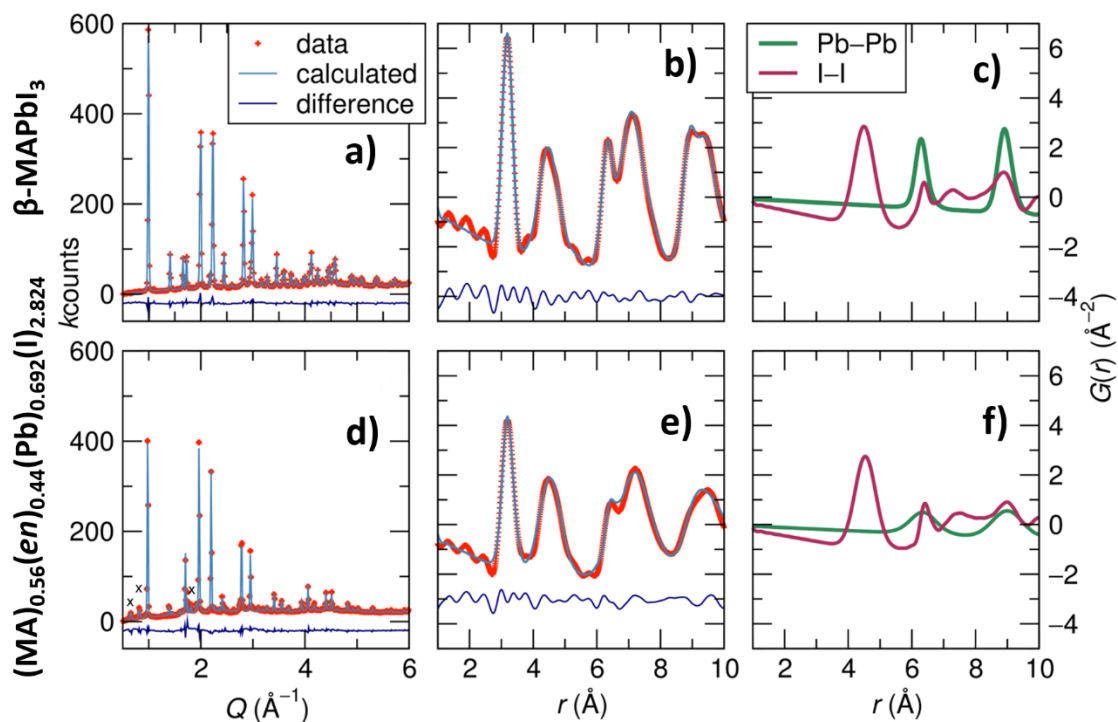
Figure 6. Experimental structure functions for the β-MAPbI$_3$ (a) and (MA)$_{0.56}$(en)$_{0.44}$(Pb)$_{0.692}$(I)$_{2.824}$ (d). Real space PDF refinement results, corresponding to the average structure of β-MAPbI$_3$ (b) and (MA)$_{0.56}$(en)$_{0.44}$(Pb)$_{0.692}$(I)$_{2.824}$ (e), Pb-Pb partial PDF (green line) and I-I partial PDF (red line) for the pristine (c) and the hollow material respectively (f). The extra peaks in the hollow sample (d), indicated by "x" marks, come from a small (approximately 8%) enPbI$_4$ impurity.
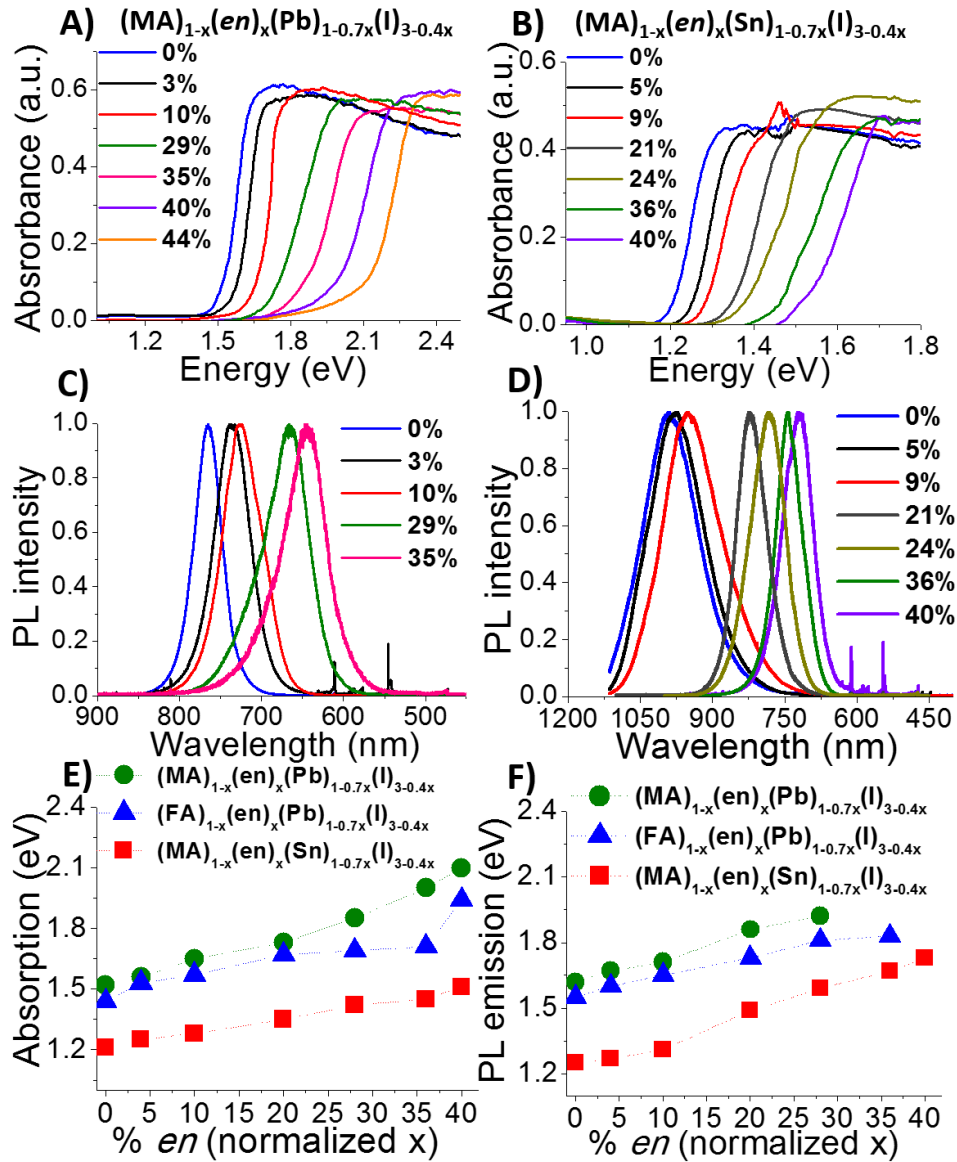
Figure 7. (A) Optical absorption spectra of compounds $(MA)_{1-x}(en)_x(Pb)_{1-0.7x}(I)_{3-0.4x}$, and (B) $(MA)_{1-x}(en)_x(Sn)_{1-0.7x}(I)_{3-0.4x}$, (C) emission spectra of compounds $(MA)_{1-x}(en)_x(Pb)_{1-0.7x}(I)_{3-0.4x}$ and (D) $(MA)_{1-x}(en)_x(Sn)_{1-0.7x}(I)_{3-0.4x}$ with increasing amount of *en* and correlation of amount of *en%* towards the recorded absorption (E) and emission spectra (F) for all hollow perovskites. For comparison purposes in figures (E) and (F) all various x values were normalized from 0 to 40 % for all materials.
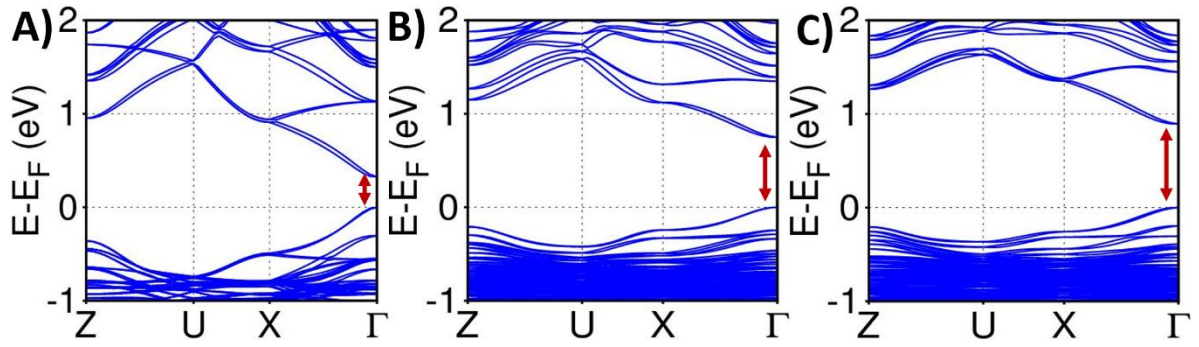
Figure 8. (A) The calculated band structure of the supercell for the full ($(FA)_{16}Pb_{16}I_{48}$) and (B) hollow ($(FA)_{16}Pb_{15}I_{46}$) and (C) ($(FA)_{16}Pb_{14}I_{44}$) perovskites. The red arrow indicates the band gap increase from 0.32eV for the pristine material to 0.89eV for the highly hollow one. The valence bandwidth (from U to G point) is 0.74 eV, 0.21 eV and 0.16 eV for (A), (B), (C) respectively. The conduction bandwidth (from U to G point) is 1.10 eV, 0.76 eV and 0.70 eV for (A), (B), (C) respectively.

Table 1. Comparison of the nominal ratio of *en*% used in the synthesis and the experimentally determined one (x) from ^{1}H-NMR spectroscopy for all 18 new materials. Extensive details about the determination of (x) from ^{1}H-NMR measurements are presented in the Materials and Methods section of the Supporting information.

nominal *en*%	10	20	50	60	70	80	100
$MASnI_3$ actual *en*% (x)	5	9	21	24	-	36	40
$MAPbI_3$ actual *en*% (x)	3	10	29	35	40	-	44
$FAPbI_3$ actual *en*% (x)	7	11	21	-	27	29	39

Table 2. Crystallographic Data of selected (FA)$_{1-x}$(*en*)$_x$(Pb)$_{1-0.7x}$(I)$_{3-0.4x}$ and (MA)$_{1-x}$(*en*)$_x$(Pb)$_{1-0.7x}$(I)$_{3-0.4x}$ compounds. Presented below are only the non-centrosymmetric crystal structures.

	(FA)$_{1-x}$(*en*)$_x$(Pb)$_{1-0.7x}$(I)$_{3-0.4x}$		(MA)$_{1-x}$(*en*)$_x$(Pb)$_{1-0.7x}$(I)$_{3-0.4x}$	
	x = 0.27	x = 0.39	x = 0.29	x = 0.44
Crystal phase/Color	α (black crystals)	β (red crystals)	α (black crystals)	α (orange crystals)
Formula weight	624.7	579.7	588.3	581.6
Temperature	293 K	293 K	293 K	293 K
Wavelength	0.71073 Å	0.71073 Å	0.71073 Å	0.71073 Å
Crystal system	orthorhombic	tetragonal	tetragonal	tetragonal
Space group	Amm2	P4bm	P4mm	P4mm
Unit cell dimensions	a = 6.3652(19) Å, α = 90° b = 9.002(2) Å, β = 90° c = 9.0065(13) Å, γ = 90°	a = 9.0452(8) Å, α = 90° b = 9.0452(8) Å, β = 90° c = 6.4036(11) Å, γ = 90°	a = 6.3361(17) Å, α = 90° b = 6.3361(17) Å, β = 90° c = 6.329(2) Å, γ = 90°	a = 6.343(3) Å, α = 90° b = 6.343(3) Å, β = 90° c = 6.340(3) Å, γ = 90°
Volume	516.0(2) Å^3	523.91(11) Å^3	254.09(13) Å^3	255.1(2) Å^3
Z	2	2	1	1
Density (calculated)	4.0202 g/cm^3	3.6748 g/cm^3	3.8444 g/cm^3	3.7866 g/cm^3
Absorption coefficient	24.598 mm^{-1}	20.757 mm^{-1}	23.107 mm^{-1}	22.493 mm^{-1}
F(000)	525	490	247	260
Crystal size (mm^3)	0.6632 x 0.0482 x 0.0330	0.0567 x 0.0403 x 0.0323	0.0097 x 0.0071 x 0.0063	0.0183 x 0.0167 x 0.0059
θ range for data collection	3.2 to 29.33°	3.18 to 29.18°	3.22 to 29.08°	3.21 to 29.03°
Index ranges	-8<=h<=8, -12<=k<=11, -12<=l<=12	-12<=h<=12, -12<=k<=12, -8<=l<=8	-8<=h<=8, -7<=k<=8, -8<=l<=8	-7<=h<=7, -8<=k<=8, -8<=l<=8
Reflections collected	2524	4394	2493	2326
Independent reflections	1402 [R$_{int}$ = 0.1234]	1105 [R$_{int}$ = 0.0884]	455 [R$_{int}$ = 0.0731]	923 [R$_{int}$ = 0.0608]
Completeness to θ = 29.33°	98%	99%	100%	100%
Refinement method	Full-matrix least-squares on F^2	Full-matrix least-squares on F^2	Full-matrix least-squares on F^2	Full-matrix least-squares on F^2
Data / restraints / parameters	1402 / 2 / 22	1105 / 2 / 20	455 / 1 / 16	923 / 1 / 17
Goodness-of-fit	3.02	3.32	1.75	1.11
Final R indices [I>2σ(I)]	R$_{obs}$ = 0.0801, wR$_{obs}$ = 0.2226	R$_{obs}$ = 0.0769, wR$_{obs}$ = 0.1475	R$_{obs}$ = 0.0461, wR$_{obs}$ = 0.1022	R$_{obs}$ = 0.0433, wR$_{obs}$ = 0.0650
R indices [all data]	R$_{all}$ = 0.1161, wR$_{all}$ = 0.2264	R$_{all}$ = 0.0877, wR$_{all}$ = 0.1483	R$_{all}$ = 0.0574, wR$_{all}$ = 0.1031	R$_{all}$ = 0.0684, wR$_{all}$ = 0.0691
Largest diff. peak and hole	1.49 and -2.21 e·Å^{-3}	2.12 and -2.24 e·Å^{-3}	0.78 and -0.76 e·Å^{-3}	0.93 and -0.41 e·Å^{-3}

$R = \Sigma||F_o|-|F_c|| / \Sigma|F_o|$, $wR = (\Sigma[w(|F_o|^2 - |F_c|^2)^2] / \Sigma[w(|F_o|^4)])^{1/2}$ and $w=1/(\sigma^2(I)+0.0004I^2)$

Table 3. Correlation between refinement occupancy parameters for Pb and I atoms when refined individually (A, B, C) for the single crystal structures of compounds $(MA)_{0.56}(en)_{0.44}(Pb)_{0.692}(I)_{2.824}$, $(MA)_{0.71}(en)_{0.29}(Pb)_{0.797}(I)_{2.884}$, $(FA)_{0.61}(en)_{0.39}(Pb)_{0.727}(I)_{2.844}$, $(FA)_{0.73}(en)_{0.27}(Pb)_{0.811}(I)_{2.892}$. Numbers in parentheses represent the ideal (unrefined) occupancy parameter of each atom. The observed R values drop when the occupancy of Pb atoms is refined (E), as compared to the full occupancy R values (D).

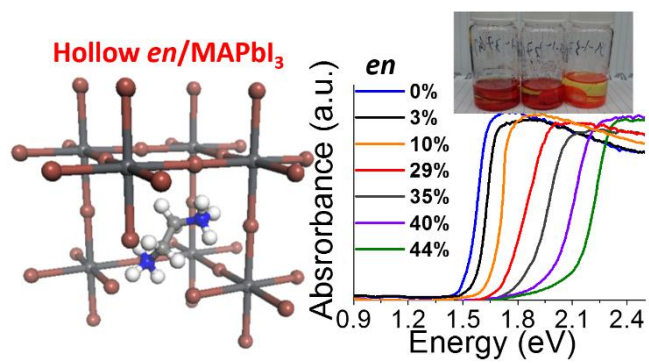| Material	A) Pb occupancy	B) I1 occupancy	C) I2 occupancy	D) Full occupancy	E) Refined Pb occupancy
$(MA)_{0.56}(en)_{0.44}(Pb)_{0.692}(I)_{2.824}$	0.101 (0.125)	0.158 (0.125)	0.317 (0.25)	$R_{obs} = 0.0685$, $wR_{obs} = 0.1086$	$R_{obs} = 0.0433$, $wR_{obs} = 0.0650$
$(MA)_{0.71}(en)_{0.29}(Pb)_{0.797}(I)_{2.884}$	0. 106 (0.125)	0.135 (0.125)	0. 274 (0.25)	$R_{obs} = 0.0654$, $wR_{obs} = 0.1316$	$R_{obs} = 0.0461$, $wR_{obs} = 0.1022$
$(FA)_{0.61}(en)_{0.39}(Pb)_{0.727}(I)_{2.844}$	0.186 (0.25)	0.283 (0.25)	0.59 (0.5)	$R_{obs} = 0.1059$, $wR_{obs} = 0.2104$	$R_{obs} = 0.0769$, $wR_{obs} = 0.1475$
$(FA)_{0.73}(en)_{0.27}(Pb)_{0.811}(I)_{2.892}$	0.240 (0.25)	0.243 (0.25)	0.519 (0.5)	$R_{obs} = 0.0796$, $wR_{obs} = 0.2231$	$R_{obs} = 0.0801$, $wR_{obs} = 0.2226$

Table 4. Comparison of the 10 different chemical formulas that were considered to best describe the hollow perovskites materials. In each formula a specific fragment or a combination of fragments are replaced by *en* impacting the material's crystal density. The column on the right shows how many materials lay above a certain threshold density value limit out of the 18 synthesized and examined materials described by each formula.

Formula	Displaced perovskite fragments by *en*	*en* charge	$\rho_{calc}- \rho_{exp}$ threshold > 0.1 g cm^{-3}
1) $Aen_{(x/2)}M_{(1-x)}I_{(3-x)}$	equal $M^{2+} + I^-$, no A^+	2+	13 out of the 18 materials
2) $A_{(1-x)}en_{(x/2)}M_{(1-x/2)}I_{(3-x)}$	equal $A^+ + I^-$, more A^+, less M^{2+}	2+	9 out of the 18 materials
3) $A_{(1-x)}en_{(x)}M_{(1-x/2)}I_3$	more A^+, less M^{2+}, no I^-	2+	8 out of the 18 materials
4) $A_{(1-x)}en_{(x)}M_{(1-x/2)}I_{(3-x)}$	equal $A^+ + I^-$, more A^+, less M^{2+}	1+	8 out of the 18 materials
5) $A_{(1-x)}en_{(x/2)}[M_{(1-d/2)}I_{(3-d)}]$ d = 0.05	more A^+, $M^{2+}$and I^- as MI_2	2+	8 out of the 18 materials
6) $A_{(1-x/2)}en_{(x)}M_{(1-x)}I_{(3-x/2)}$	equal $A^+ + I^-$, less A^+, more M^{2+}	2+	5 out of the 18 materials
7) $Aen_{(x)}M_{(1-x/2)}I_{(3-x/2)}$	equal $M^{2+} + I^-$ in lower amounts, no A^+	2+	2 out of the 18 materials
8) $Aen_{(x)}M_{(1-x)}I_3$	no $A^+ + I^-$, only M^{2+}	2+	2 out of the 18 materials
9) $A_{(1-x/2)}en_{(x/2)}M_{(1-x/2)}I_{(3-x/2)}$	equal $A^+ + I^- + M^{2+}$	2+	1 out of the 18 materials
10) $A_{(1-x)}en_{(x)}M_{(1-0.7x)}I_{(3-0.4x)}$	equal A^+, more M^{2+}, less I^-	2+	All materials below the threshold limit

Table 5. Measured band gap energy (eV) from the absorption spectra and the corresponding PL peak positions (eV) for all hollow and pristine examined materials (x=0). The maximum recorded energy difference values are 0.22 eV for the $(MA)_{1-x}(en)_x(Sn)_{1-0.7x}(I)_{3-0.4x}$ compounds, 0.12 eV for the $(FA)_{1-x}(en)_x(Pb)_{1-0.7x}(I)_{3-0.4x}$ compounds and 0.13 eV for the $(MA)_{1-x}(en)_x(Pb)_{1-0.7x}(I)_{3-0.4x}$ compounds.

normalized x% _en_ value	$(MA)_{1-x}(en)_x(Sn)_{1-0.7x}(I)_{3-0.4x}$		$(FA)_{1-x}(en)_x(Pb)_{1-0.7x}(I)_{3-0.4x}$		$(MA)_{1-x}(en)_x(Pb)_{1-0.7x}(I)_{3-0.4x}$	
	Band gap (eV)	PL peak (eV)	Band gap (eV)	PL peak (eV)	Band gap (eV)	PL peak (eV)
0	1.21	1.25	1.44	1.55	1.52	1.62
4	1.25	1.27	1.53	1.6	1.56	1.68
10	1.28	1.31	1.57	1.65	1.65	1.71
20	1.35	1.49	1.67	1.73	1.73	1.86
28	1.42	1.59	1.69	1.81	1.85	1.93
36	1.45	1.67	1.71	1.83	2	-
40	1.51	1.73	1.94	-	2.1	-

Table of Contents

Hollow *en*/MAPbI₃

Supporting information

Unraveling the Chemical Nature of the 3D "Hollow'' Hybrid Halide Perovskites

Ioannis Spanopoulos[†], Weijun Ke[†], Constantinos C. Stoumpos[†], Emily C. Schueller[||], Oleg Y. Kontsevoi[§], Ram Seshadri[||] and Mercouri G. Kanatzidis*[,†]

[†]*Department of Chemistry, Northwestern University, Evanston, IL 60208, United States*

[||]*Materials Research Laboratory, Materials Department, and Department of Chemistry and Biochemistry, University of California, Santa Barbara, CA 93106, United States*

[§]*Department of Physics and Astronomy, Northwestern University, Evanston, IL 60208, United States*

Table of contents

1. Materials and methods

Starting materials

All starting materials for synthesis were purchased commercially and were used without further purification. Lead(II) acetate trihydrate puriss. p.a., ACS, 99.5-102.0%, Tin(II) chloride dihydrate puriss. p.a., ACS, ≥98%, Methylamine hydrochloride ≥98%, Formamidine acetate 99%, Hypophosphorous acid solution 50 wt. % in H_2O, Hydriodic acid 57 wt. % in H_2O, distilled, stabilized, 99.95%, Ethylenediamine ReagentPlus®, ≥99% and Dimethyl sulfoxide-d_6 99.9 atom %D were purchased from Aldrich. 20 mL glass scintillation vials were used in all the syntheses of the materials. The same batch of the starting materials were used in all syntheses.

^{1}H-NMR measurements

^{1}H NMR spectra were recorded on 600 MHz Bruker, A600 spectrometer. All samples were prepared by dissolving a small portion of the dried solids (~ 10 mg) in a DMSO-d_6 solution (0.5 mL). The actual amount of *en* (x) that resides in the crystal structure was determined by ^{1}H-NMR spectroscopy. The (x) value was used for the calculations of all the examined crystal formulas.

From NMR spectroscopy it was possible to calculate only the ratio between *en* and MA, FA molecules. In order to find a way to quantify the amount of *en* relative to the MA we have introduced another equation that included the two molecules, namely:

$$MA + en = 1 \quad \text{(eq. 1)}$$

This is consistent with the 113 (Cation)MX_3 (Cation= MA + *en*) perovskite formula. Since we have only two organic molecules in the structure, the total organic content should be equal to 1 (or 100%). These constrains along with a requirement for charge balance were used in all formula calculations and is mentioned in Table 1 and Tables S29-31.

Using the density difference criteria and for reasons we extensively explain on page 11, subsection "Hollow perovskites have lower density" in the manuscript, we chose the charged balanced formula $A_{(1-x)}en_{(x)}M_{(1-0.7x)}I_{(3-0.4x)}$. In this case *en* molecules replace I^-, M^{2+} and A^+ in the crystal in a manner that can afford a charge balanced formula, and can cover a wide range of (x) values up to 0.9 (90%).

Under the current drying conditions (110 ^{0}C, for 12h under vacuum) based on ^{1}H-NMR data, it seems that there is a small amount of residual H_3PO_2 on some of the Pb based crystals. However based on the spectra presented in Figures S19-20 and S23-24, the amount of residual H_3PO_2 depends on the drying temperature. Therefore, it is possible that higher drying temperatures may lead to complete absence of H_2PO_3. Furthermore, based on EDX analysis, taking a closer look at Figure S37, there is no Phosphorous (P) peak in the spectra. The Kα energy for (P) is expected at 2.013 eV lower than the (Pb) M peak at 2.342 eV. This energy difference is sufficient for the separation of the two peaks in the EDX spectrum. Those findings indicate that the presence of residual H_3PO_2 is due to the drying process and is not part of the crystal structure.

XRD measurements

Single-crystal X-ray diffraction

Single crystal diffraction experiments were performed using either a STOE IPDS II or IPDS 2T diffractometer using Mo Kα radiation (λ = 0.71073 Å) and operating at 50 kV and 40 mA. Integration and numerical absorption corrections were performed using the X-AREA, X-RED, and X-SHAPE programs. The structure was solved by charge flipping and refined by full-matrix least squares on F^2 with the Jana2006 package.[1]

Powder X-ray diffraction

Powder X-ray diffraction patterns were collected on a Rigaku Miniflex system (CuKα radiation) operated at 40 kV and 15 mA. A typical scan rate was 10 sec/step with a step size of 0.02 deg. The data were manipulated with CMPR,[2] and Rietveld analysis was performed with the Jana2006 package.[1] All PXRD patterns are recorded on the same in house instrument, except for the patterns used in PDF analysis, where they were recorded at synchrotron.

Pair distribution function analysis

For the synchrotron total scattering measurements, samples of fine powder, obtained by the means described above, were transferred into Kapton capillaries (0.81 mm OD, 0.8 mm ID) and tightly compacted to ensure a maximum packing fraction. Both ends of the capillaries were sealed with epoxy and stored at RT. The synchrotron X-ray total scattering measurements were recorded on the 11-ID-B beam line at the Advanced Photon Source located at Argonne National Laboratory.

Comments on the selection of the crystal space groups

The solved single crystal structures of the 3D perovskites were solved in both centrosymmetric and non-centrosymmetric space groups and all .cif files are available as supporting information. However for reasons we refer to in the manuscript (subchapter structural properties) all 3D structures were refined using the non-centrosymmetric space groups.

Optical Spectroscopy.

Optical diffuse-reflectance measurements were performed at room temperature using a Shimadzu UV-3600 PC double-beam, double-monochromator spectrophotometer operating from 200 to 2500 nm. $BaSO_4$ was used as a non-absorbing reflectance reference. The generated reflectance-versus-wavelength data were used to estimate the band gap of the material by converting reflectance to absorbance data according to the Kubelka–Munk equation: $\alpha/S = (1 - R)2/2R$, where R is the reflectance and α and S are the absorption and scattering coefficients, respectively.[3]

PL Measurements.

All samples were measured using a Horiba LabRam Evolution high-resolution confocal Raman microscope spectrometer (600 g/mm diffraction grating) equipped with a diode continuous wave laser (473 nm, 25 mW) and a Synapse charge-coupled device camera. The maximum power output of the laser source was filtered to 1% of the maximum power output.

TGA measurements

The Thermogravimetric Analysis (TGA) measurements were performed on a Netzsch's Simultaneous Thermal Analysis (STA) system. An amount of ~15 mg of sample was placed inside an alumina cap and heated up to 700 °C under He flow with a heating rate of 8 °C/min. We must note here that if an aluminum cap is used instead (up to 600 °C), then the TGA curve is incomplete, as there is a significant amount of a residue left, possibly from the reaction of the perovskite with the metallic medium.[4-5]

SEM/EDX

Scanning Electron Microscopy (SEM) measurements were recorded on a high-resolution field emission Hitachi SU8030. A Hitachi S3400N-II instrument equipped with a PGT energy-dispersive X-ray analyser was used for the EDX measurements. Data were acquired with an accelerating voltage of 20 kV.

Density measurements

  A Micromeritics AccuPyc II 1340 pycnometer was utilized for the density determination of all samples. An amount of 400 mg of dry sample was loaded to an aluminum cap (1 mL) and the volume determination was performed based on He displacement. Each sample was measured 5 times and the sample volume was recorded along with standard deviation. The average volume of each sample was used for the density calculations.

DFT calculations

  First-principles electronic structure calculations were carried out within the density functional theory (DFT) formalism using the Projector Augmented Wave method[6] implemented in Vienna Ab-initio Simulation Package.[7] The internal atomic positions were optimized until the atomic forces on each atom were less than 0.01 eV/Å with the plane-wave cutoff energy of 350 eV and a 4x3x3 Γ-centered Monkhorst-Pack k-point grid, while the volume and shape of the unit cell were fixed. Multiple possible orientations of PbI_2 vacancies in the single-vacancy supercells and multiple configurations of PbI_2 vacancies in two-vacancy supercells were considered, and lowest-energy configurations were selected for further band structure analysis. For the exchange-correlation function, the generalized gradient approximation (GGA) was employed within Perdew-Burke-Ernzerhof (PBE) formalism[8] and the spin−orbit coupling (SOC) was included in the calculation. Despite a known tendency of semi-local PBE functional to underestimate the band gaps compared to the experimentally obtained values, it is well accepted that semi-local density functionals can well describe the main features of the band structure such as band dispersion and band composition and reproduce general trends in band gap change under uniform transformation in the same material.

2. Syntheses

a) Syntheses of $(MA)_{1-x}(en)_x(Sn)_{1-0.7x}(I)_{3-0.4x}$ (x: 0%, 5%, 9%, 21%, 24%, 36%, 40%)

α-MASnI₃: 679.95 mg (3 mmol) of $SnCl_2 \cdot 2H_2O$ were dissolved in a solution consisting of 8 mL of 57% w/w aqueous HI and 1.5 mL of 50% aqueous H_3PO_2, by heating to boiling under constant magnetic stirring. Then 202.56 mg (3 mmol) of methylamine hydrochloride were added to the hot yellow solution, leading to the formation of black crystals. They were collected by suction filtration and dried in a vacuum oven at 110°C for 12h. Yield: 637 mg, (40% based on Sn)

x = 5%: 679.95 mg (3 mmol) of $SnCl_2 \cdot 2H_2O$ were dissolved in a 57% w/w aqueous HI solution (8 mL) by heating to boiling under constant magnetic stirring for about 5 minutes. Then 20 μL of ethylenediamine (0.3 mmol) were added to 50% aqueous H_3PO_2 (1.5 mL) at RT. This solution was added to the hot reaction solution. Subsequent addition of 202.56 mg (3 mmol) of methylamine hydrochloride to the hot yellow solution lead to the formation of black crystals. Stirring was continued for 5 min. The crystals were collected by suction filtration and dried in a vacuum oven at 110°C for 12h. Yield: 630 mg, (39.5% based on Sn)

x = 9%: 679.95 mg (3 mmol) of $SnCl_2 \cdot 2H_2O$ were dissolved in a 57% w/w aqueous HI solution (8 mL) by heating to boiling under constant magnetic stirring for about 5 minutes. Then 40 μL of ethylenediamine (0.6 mmol) were added to 50% aqueous H_3PO_2 (1.5 mL) at RT. This solution was added to the hot reaction solution. Subsequent addition of 202.56 mg (3 mmol) of

methylamine hydrochloride to the hot yellow solution lead to the formation of black crystals. Stirring was continued for 5 min. The crystals were collected by suction filtration and dried in a vacuum oven at 110°C for 12h. Yield: 640 mg, (40.1% based on Sn)

x = 21%: 679.95 mg (3 mmol) of $SnCl_2 \cdot 2H_2O$ were dissolved in a 57% w/w aqueous HI solution (8 mL) by heating to boiling under constant magnetic stirring for about 5 minutes. Then 100 µL of ethylenediamine (1.5 mmol) were added to 50% aqueous H_3PO_2 (1.5 mL) at RT. This solution was added to the hot reaction solution. Subsequent addition of 202.56 mg (3 mmol) of methylamine hydrochloride to the hot yellow solution lead to the formation of black crystals. Stirring was continued for 5 min. The crystals were collected by suction filtration and dried in a vacuum oven at 110°C for 12h. Yield: 646 mg, (40.5% based on Sn)

x = 24%: 679.95 mg (3 mmol) of $SnCl_2 \cdot 2H_2O$ were dissolved in a 57% w/w aqueous HI solution (8 mL) by heating to boiling under constant magnetic stirring for about 5 minutes. Then 120 µL of ethylenediamine (1.8 mmol) were added to 50% aqueous H_3PO_2 (1.5 mL) at RT. This solution was added to the hot reaction solution. Subsequent addition of 202.56 mg (3 mmol) of methylamine hydrochloride to the hot yellow solution lead to the formation of black crystals. Stirring was continued for 5 min. The crystals were collected by suction filtration and dried in a vacuum oven at 110°C for 12h. Yield: 635 mg, (39.8% based on Sn)

x = 36%: 679.95 mg (3 mmol) of $SnCl_2 \cdot 2H_2O$ were dissolved in a 57% w/w aqueous HI solution (8 mL) by heating to boiling under constant magnetic stirring for about 5 minutes. Then 160 µL of ethylenediamine (2.4 mmol) were added to 50% aqueous H_3PO_2 (1.5 mL) at RT. This solution was added to the hot reaction solution. Subsequent addition of 202.56 mg (3 mmol) of methylamine hydrochloride to the hot yellow solution lead to the formation of black crystals. Stirring was continued for 5 min. The crystals were collected by suction filtration and dried in a vacuum oven at 110°C for 12h. Yield: 620 mg, (38.9% based on Sn)

x = 40%: 679.95 mg (3 mmol) of $SnCl_2 \cdot 2H_2O$ were dissolved in a 57% w/w aqueous HI solution (8 mL) by heating to boiling under constant magnetic stirring for about 5 minutes. Then 200 µL of ethylenediamine (3 mmol) were added to 50% aqueous H_3PO_2 (1.5 mL) at RT. This solution was added to the hot reaction solution. Subsequent addition of 202.56 mg (3 mmol) of methylamine hydrochloride to the hot yellow solution lead to the formation of black crystals. Stirring was continued for 5 min. The crystals were collected by suction filtration and dried in a vacuum oven at 110°C for 12h. Yield: Yield: 610 mg, (38.3% based on Sn)

b) Syntheses of $(FA)_{1-x}(en)_x(Pb)_{1-0.7x}(I)_{3-0.4x}$ (x: 0%, 7%, 11%, 21%, 27%, 29%, 39%)

α-FAPbI₃: 1137 mg (3 mmol) of $Pb(CH_3CO_2)_2 \cdot 3H_2O$ were dissolved in a solution consisting of 8 mL of 57% w/w aqueous HI and 1.2 mL of 50% aqueous H_3PO_2, by heating to boiling under constant magnetic stirring. Then 312 mg (3 mmol) of formamidine acetate were added to the hot yellow solution, leading to the formation of yellow crystals (δ phase). The reaction mixture was heated for additional 10 min where all the yellow crystals turned black (α phase). They were collected immediately by suction filtration and dried in a vacuum oven at 110°C for 12h. Yield: 1044 mg, (55% based on Pb)

x = 7%: 1137 mg (3 mmol) of $Pb(CH_3CO_2)_2 \cdot 3H_2O$ were dissolved in a 57% w/w aqueous HI solution (8 mL) by heating to boiling under constant magnetic stirring for about 5 minutes. Then 20 µL of ethylenediamine (0.3 mmol) were added to 50% aqueous H_3PO_2 (1.2 mL) at RT. This solution was added to the hot reaction solution. Subsequent addition of 312 mg (3 mmol) of formamidine acetate to the hot yellow solution lead to the formation of black crystals.

Stirring was continued for 5 min. The crystals were collected by suction filtration and dried in a vacuum oven at 110°C for 12h. Yield: 1065 mg, (56% based on Pb)

x = 11%: 1137 mg (3 mmol) of $Pb(CH_3CO_2)_2 \cdot 3H_2O$ were dissolved in a 57% w/w aqueous HI solution (8 mL) by heating to boiling under constant magnetic stirring for about 5 minutes. Then 40 µL of ethylenediamine (0.6 mmol) were added to 50% aqueous H_3PO_2 (1.2 mL) at RT. This solution was added to the hot reaction solution. Subsequent addition of 312 mg (3 mmol) of formamidine acetate to the hot yellow solution lead to the formation of black crystals. Stirring was continued for 5 min. The crystals were collected by suction filtration and dried in a vacuum oven at 110°C for 12h. Yield: 1101 mg, (58% based on Pb)

x = 21%: 1137 mg (3 mmol) of $Pb(CH_3CO_2)_2 \cdot 3H_2O$ were dissolved in a 57% w/w aqueous HI solution (8 mL) by heating to boiling under constant magnetic stirring for about 5 minutes. Then 100 µL of ethylenediamine (1.5 mmol) were added to 50% aqueous H_3PO_2 (1.2 mL) at RT. This solution was added to the hot reaction solution. Subsequent addition of 312 mg (3 mmol) of formamidine acetate to the hot yellow solution lead to the formation of black crystals. Stirring was continued for 5 min. The crystals were collected by suction filtration and dried in a vacuum oven at 110°C for 12h. Yield: 1006 mg, (53% based on Pb)

x = 27%: 1137 mg (3 mmol) of $Pb(CH_3CO_2)_2 \cdot 3H_2O$ were dissolved in a 57% w/w aqueous HI solution (8 mL) by heating to boiling under constant magnetic stirring for about 5 minutes. Then 140 µL of ethylenediamine (2.1 mmol) were added to 50% aqueous H_3PO_2 (1.2 mL) at RT. This solution was added to the hot reaction solution. Subsequent addition of 312 mg (3 mmol) of formamidine acetate to the hot yellow solution lead to the formation of black crystals. Stirring was continued for 5 min. The crystals were collected by suction filtration and dried in a vacuum oven at 110°C for 12h. Yield: 968 mg, (51% based on Pb)

x = 29%: 1137 mg (3 mmol) of $Pb(CH_3CO_2)_2 \cdot 3H_2O$ were dissolved in a 57% w/w aqueous HI solution (8 mL) by heating to boiling under constant magnetic stirring for about 5 minutes. Then 160 µL of ethylenediamine (2.4 mmol) were added to 50% aqueous H_3PO_2 (1.2 mL) at RT. This solution was added to the hot reaction solution. Subsequent addition of 312 mg (3 mmol) of formamidine acetate to the hot yellow solution lead to the formation of black crystals. Stirring was continued for 5 min. The crystals were collected by suction filtration and dried in a vacuum oven at 110°C for 12h. Yield: 930 mg, (49% based on Pb)

x = 39%: 1137 mg (3 mmol) of $Pb(CH_3CO_2)_2 \cdot 3H_2O$ were dissolved in a 57% w/w aqueous HI solution (10 mL) by heating to boiling under constant magnetic stirring for about 5 minutes. Then 200 µL of ethylenediamine (3 mmol) were added to 50% aqueous H_3PO_2 (1.2 mL) at RT. This solution was added to the hot reaction solution. Following this, 312 mg (3 mmol) of formamidine acetate were added to the hot yellow solution giving rise to the precipitation of a black powder, which was rapidly dissolved under stirring to afford a clear bright yellow solution. The stirring was then discontinued, and the solution was left to cool to room temperature. Upon cooling dark red crystals deposited. They were collected by suction filtration and dried in a vacuum oven at 110°C for 12h. Yield: 720 mg, (38% based on Pb)

c) Syntheses of $(MA)_{1-x}(en)_x(Pb)_{1-0.7x}(I)_{3-0.4x}$ (x: 0%, 3%, 10%, 29%, 35%, 40%, 44%)

β-MAPbI₃: 1137 mg (3 mmol) of $Pb(CH_3CO_2)_2 \cdot 3H_2O$ were dissolved in a solution consisting of 5 mL of 57% w/w aqueous HI and 1.2 mL of 50% aqueous H_3PO_2, by heating to boiling under constant magnetic stirring. Then 202.56 mg (3 mmol) of methylamine hydrochloride were added to the hot yellow solution, leading to the formation of black crystals. They were collected by suction filtration and dried in a vacuum oven at 110°C for 12h. Yield: 837 mg, (45% based on Pb)

x = 3%: 1137 mg (3 mmol) of $Pb(CH_3CO_2)_2 \cdot 3H_2O$ were dissolved in a 57% w/w aqueous HI solution (5 mL) by heating to boiling under constant magnetic stirring for about 5 minutes. Then 20 µL of ethylenediamine (0.3 mmol) were added to 50% aqueous H_3PO_2 (1.2 mL) at RT.

This solution was added to the hot reaction solution. Subsequent addition of 202.56 mg (3 mmol) of methylamine hydrochloride to the hot yellow solution lead to the formation of black crystals. They were collected by suction filtration and dried in a vacuum oven at 110°C for 12h. Yield: 818 mg, (44% based on Pb)

x = 10%: 1137 mg (3 mmol) of Pb(CH$_3$CO$_2$)$_2$ · 3H$_2$O were dissolved in a 57% w/w aqueous HI solution (5 mL) by heating to boiling under constant magnetic stirring for about 5 minutes. Then 40 µL of ethylenediamine (0.6 mmol) were added to 50% aqueous H$_3$PO$_2$ (1.2 mL) at RT. This solution was added to the hot reaction solution. Subsequent addition of 202.56 mg (3 mmol) of methylamine hydrochloride to the hot yellow solution lead to the formation of black crystals. They were collected by suction filtration and dried in a vacuum oven at 110°C for 12h. Yield: 874 mg, (47% based on Pb)

x = 29%: 1137 mg (3 mmol) of Pb(CH$_3$CO$_2$)$_2$ · 3H$_2$O were dissolved in a 57% w/w aqueous HI solution (5 mL) by heating to boiling under constant magnetic stirring for about 5 minutes. Then 100 µL of ethylenediamine (1.5 mmol) were added to 50% aqueous H$_3$PO$_2$ (1.2 mL) at RT. This solution was added to the hot reaction solution. Subsequent addition of 202.56 mg (3 mmol) of methylamine hydrochloride to the hot yellow solution lead to the formation of black crystals. They were collected by suction filtration and dried in a vacuum oven at 110°C for 12h. Yield: 781 mg, (42% based on Pb)

x = 35%: 1137 mg (3 mmol) of Pb(CH$_3$CO$_2$)$_2$ · 3H$_2$O were dissolved in a 57% w/w aqueous HI solution (5 mL) by heating to boiling under constant magnetic stirring for about 5 minutes. Then 120 µL of ethylenediamine (1.8 mmol) were added to 50% aqueous H$_3$PO$_2$ (1.2 mL) at RT. This solution was added to the hot reaction solution. Following this, 202.56 mg (3 mmol) of methylamine hydrochloride were added to the hot yellow solution. The stirring was then discontinued, and the solution was left to cool to room temperature. Upon cooling dark red crystals deposited. They were collected by suction filtration and dried in a vacuum oven at 110°C for 12h. Yield: 725 mg, (39% based on Pb)

x = 40%: 1137 mg (3 mmol) of Pb(CH$_3$CO$_2$)$_2$ · 3H$_2$O were dissolved in a 57% w/w aqueous HI solution (5 mL) by heating to boiling under constant magnetic stirring for about 5 minutes. Then 140 µL of ethylenediamine (2.1 mmol) were added to 50% aqueous H$_3$PO$_2$ (1.2 mL) at RT. This solution was added to the hot reaction solution. Following this, 202.56 mg (3 mmol) of methylamine hydrochloride were added to the hot yellow solution. The stirring was then discontinued, and the solution was left to cool to room temperature. Upon cooling red crystals deposited. They were collected by suction filtration and dried in a vacuum oven at 110°C for 12h. Yield: 632 mg, (34% based on Pb)

x = 44%: 1137 mg (3 mmol) of Pb(CH$_3$CO$_2$)$_2$ · 3H$_2$O were dissolved in a 57% w/w aqueous HI solution (5 mL) by heating to boiling under constant magnetic stirring for about 5 minutes. Then 200 µL of ethylenediamine (3 mmol) were added to 50% aqueous H$_3$PO$_2$ (1 mL) at RT. This solution was added to the hot reaction solution. Following this, 202.56 mg (3 mmol) of methylamine hydrochloride were added to the hot yellow solution. The stirring was then discontinued, and the solution was left to cool to room temperature. Upon cooling orange crystals deposited. They were collected by suction filtration and dried in a vacuum oven at 110°C for 12h. Yield: 465 mg, (25% based on Pb)

3. Characterization
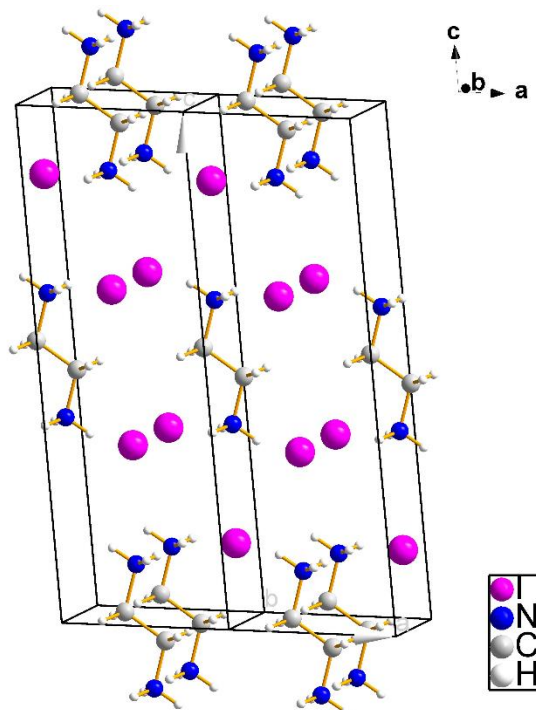
X-ray diffraction measurements

Figure S1. Part of the 0D molecular *en*I$_2$ structure looking down the b axis (010). The structure consists of single I atoms that are charged balanced by ethylenediammonium cations.
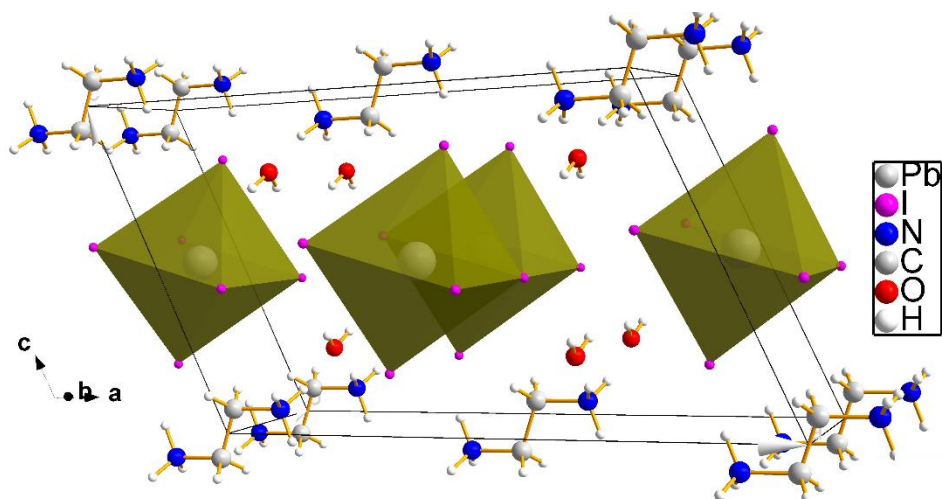

Figure S2. Part of the 1D *en*PbI$_4$ structure looking down the b axis (010). The structure consists of 1D [PbI$_4$]$^{2-}$ chains, presented here as edge sharing octahedra, that are separated and charged balanced by ethylenediammonium cations. Water molecules also reside in the structure.

Table S1. Crystallographic Data of *en*I$_2$ and *en*PbI$_4$ compounds.

	*en*I$_2$	*en*PbI$_4$
Empirical formula	C2 H10 I2 N2	C2 H12 I4 N2 O2 Pb1
Formula weight	315.9	810.9
Temperature	293 K	293 K
Wavelength	0.71073 Å	0.71073 Å
Crystal system	monoclinic	monoclinic
Space group	I2/m	C 1 2/m 1
Unit cell dimensions	a = 15.540(2) Å, α = 90° b = 5.0795(6) Å, β = 96.032(11)° c = 5.0964(7) Å, γ = 90°	a = 16.492(3) Å, α = 90° b = 4.7532(11) Å, β = 113.907(12)° c = 10.4165(18) Å, γ = 90°
Volume	400.06(9) Å^3	746.5(3) Å^3
Z	2	2
Density (calculated)	2.6226 g/cm^3	3.6077 g/cm^3
Absorption coefficient	7.763 mm^{-1}	19.546 mm^{-1}
F(000)	282	696
Crystal size	0.1172 x 0.0611 x 0.0520 mm^3	0.1275 x 0.0389 x 0.0304 mm^3
θ range for data collection	2.64 to 29.12°	2.14 to 29.25°
Index ranges	-20<=h<=20, -6<=k<=6, -6<=l<=6	-22<=h<=22, -6<=k<=6, -14<=l<=14
Reflections collected	1850	3610
Independent reflections	589 [R$_{int}$ = 0.0623]	1119 [R$_{int}$ = 0.0916]
Completeness to θ = 29.33°	99%	98%
Refinement method	Full-matrix least-squares on F^2	Full-matrix least-squares on F^2
Data / restraints / parameters	589 / 0 / 20	1119 / 0 / 42
Goodness-of-fit	3.24	3.36
Final R indices [I>2σ(I)]	R$_{obs}$ = 0.0450, wR$_{obs}$ = 0.1061	R$_{obs}$ = 0.0605, wR$_{obs}$ = 0.1326
R indices [all data]	R$_{all}$ = 0.0518, wR$_{all}$ = 0.1071	R$_{all}$ = 0.0692, wR$_{all}$ = 0.1332
Extinction coefficient	-	-
Largest diff. peak and hole	1.94 and -1.77 e·Å^{-3}	4.41 and -4.77 e·Å^{-3}

$R = \Sigma||F_o|-|F_c|| / \Sigma|F_o|$, $wR = (\Sigma[w(|F_o|^2 - |F_c|^2)^2] / \Sigma[w(|F_o|^4)])^{1/2}$ and $w=1/(\sigma^2(I)+0.0004I^2)$
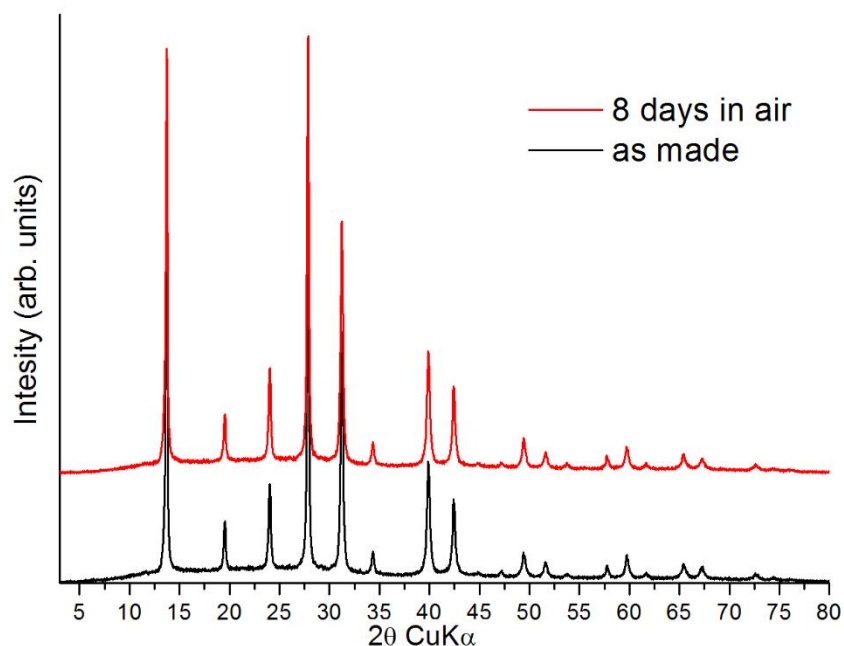
Figure S3. Experimental powder X-ray diffraction (PXRD) patterns of the freshly prepared pristine compound α-FAPbI$_3$ and after 8 days exposure to air.

Figure S4. A) Comparison of PXRD patterns of the (FA)$_{1-x}$(*en*)$_x$(Pb)$_{1-0.7x}$(I)$_{3-0.4x}$ compounds with increasing amount of *en*. The resulting materials for x-values up to 27% are isostructural to the pristine α phase FAPbI$_3$, while (FA)$_{0.61}$(*en*)$_{0.39}$(Pb)$_{0.727}$(I)$_{2.844}$ (x = 39%) is isostructural to the pristine β phase FAPbI$_3$. B) The red circle and arrows indicate the position of the appearance of additional diffraction peaks at 2θ = 22.3^0 and 26.4^0 (x = 39%), which are characteristic of the pure β-FAPbI$_3$.

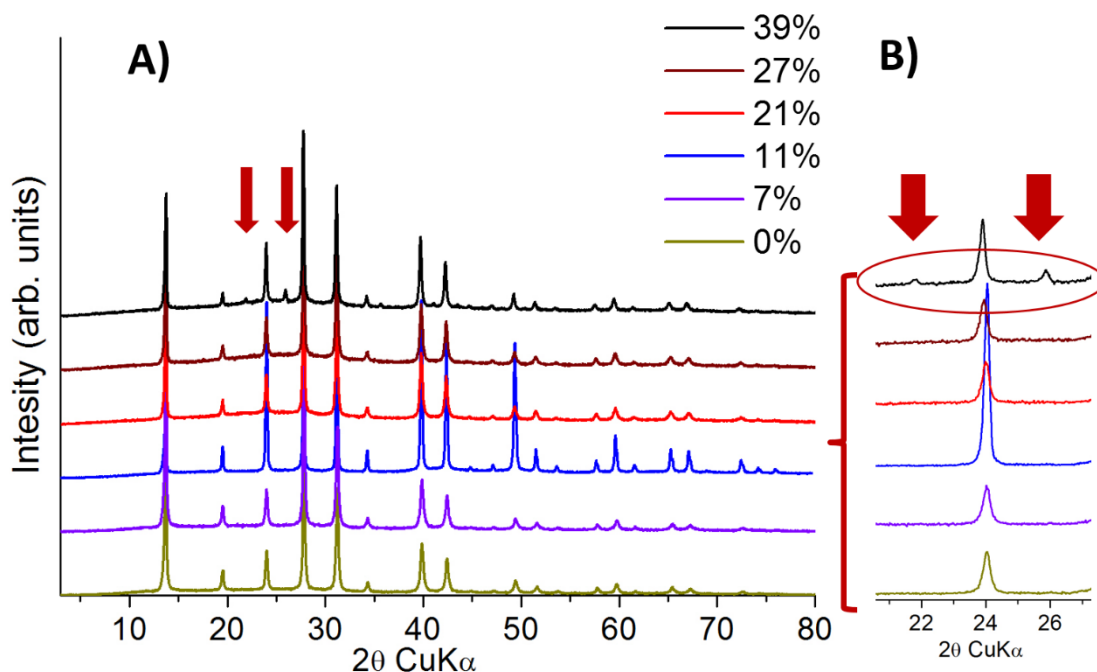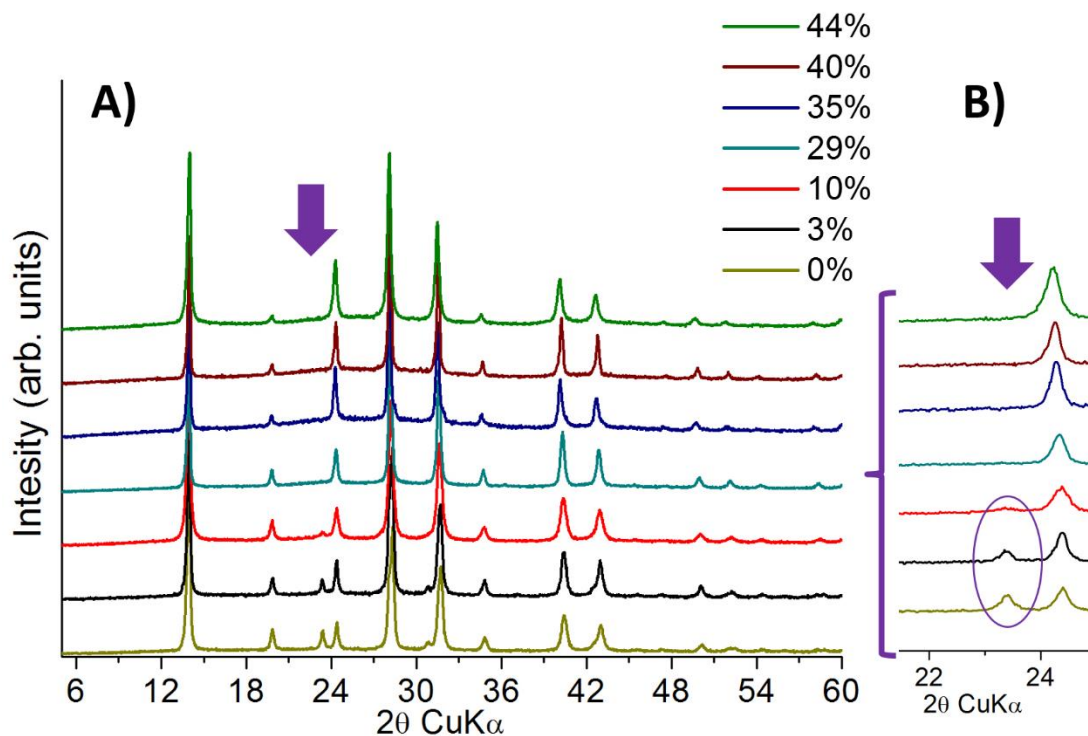**Figure S5.** A) Comparison of PXRD patterns of the $(MA)_{1-x}(en)_x(Pb)_{1-0.7x}(I)_{3-0.4x}$ compounds with increasing amount of *en*. The $(MA)_{0.97}(en)_{0.03}(Pb)_{0.979}(I)_{2.988}$ hollow perovskite (x = 3%) is isostructural to the pristine β phase MAPbI₃, while the rest of the hollow materials for x values up to 44% are isostructural to the pristine α phase MAPbI₃. B) The purple circle and arrow indicates the position of the progressive disappearance of the diffraction peak at $2\theta = 23.7^0$ with increasing amount of *en*, which is characteristic of the β phase MAPbI₃, giving rise to uniform α-MAPbI₃ crystals.
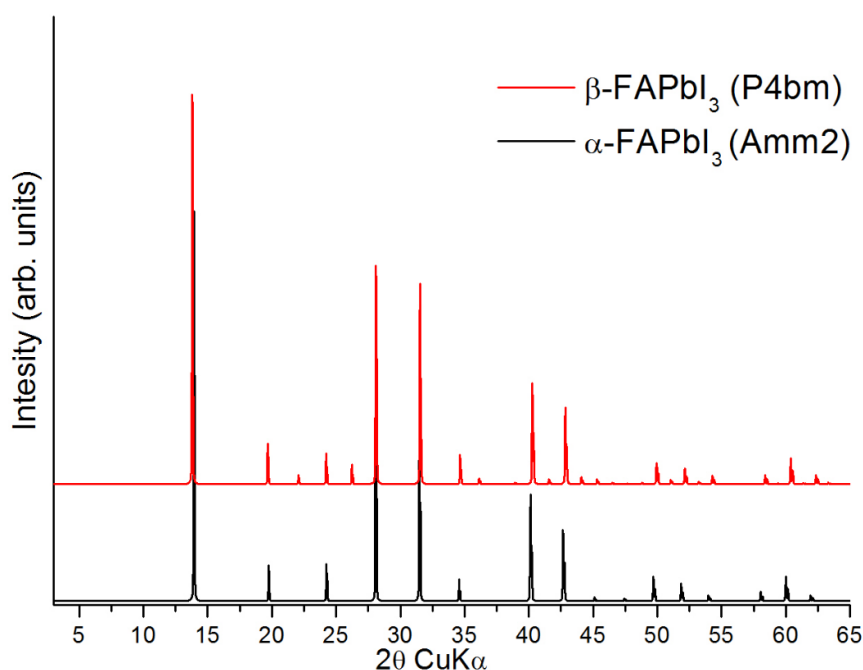
Figure S6. Comparison of the calculated PXRD patterns from the single crystal structures of the pristine α phase FAPbI₃ and β phase FAPbI₃.
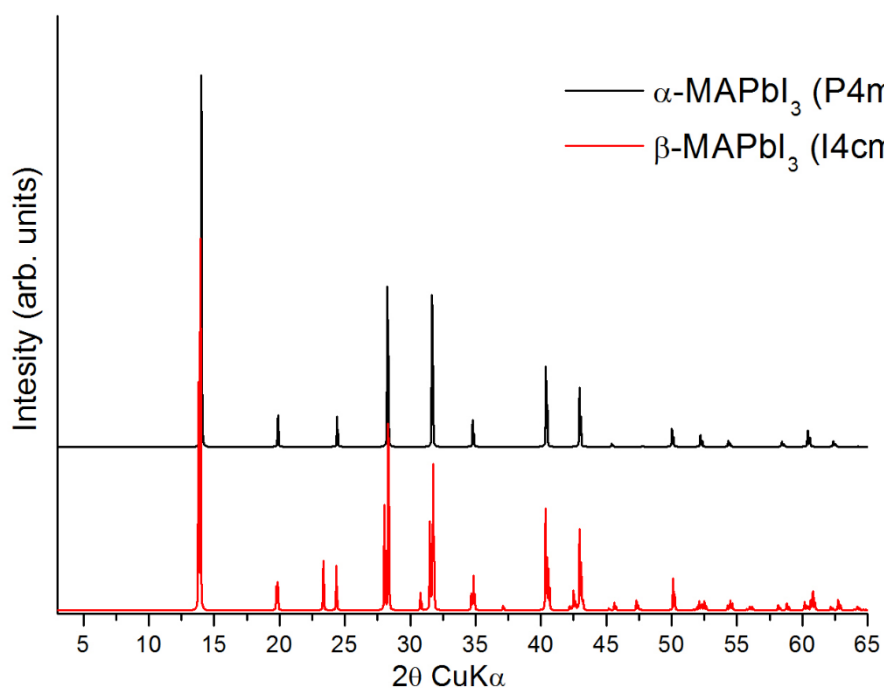
Figure S7. Comparison of the calculated PXRD patterns from the single crystal structures of the pristine α phase MAPbI₃ and β phase MAPbI₃.
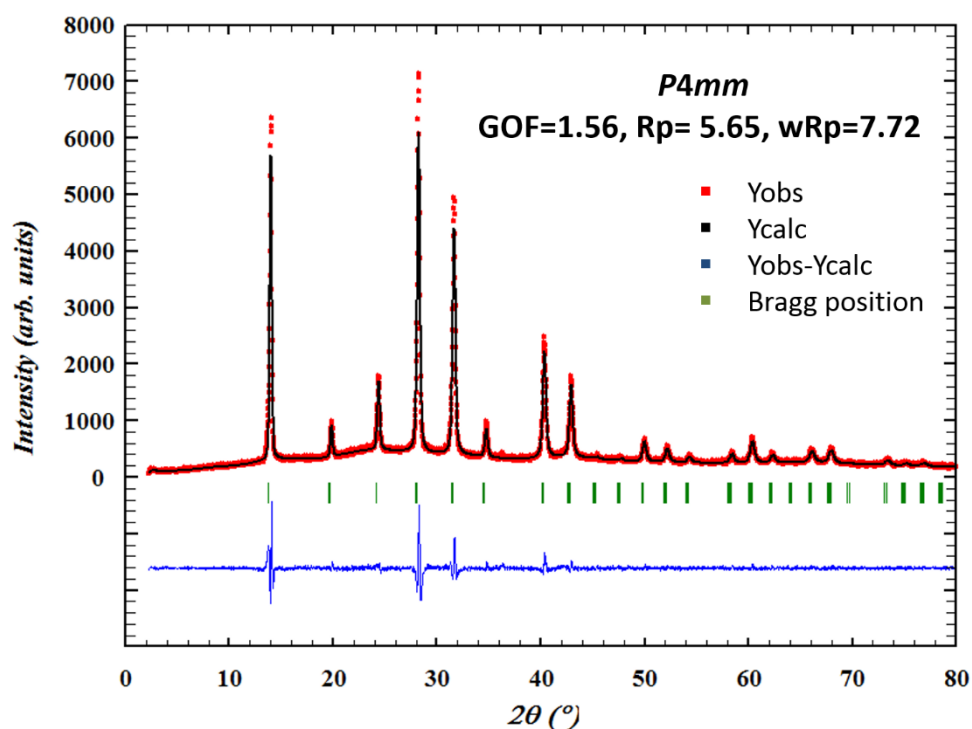
Figure S8. Observed and calculated diffraction profiles from the Rietveld refinement of compound $(MA)_{0.71}(en)_{0.29}(Pb)_{0.797}(I)_{2.884,}$ (Cu Kα).
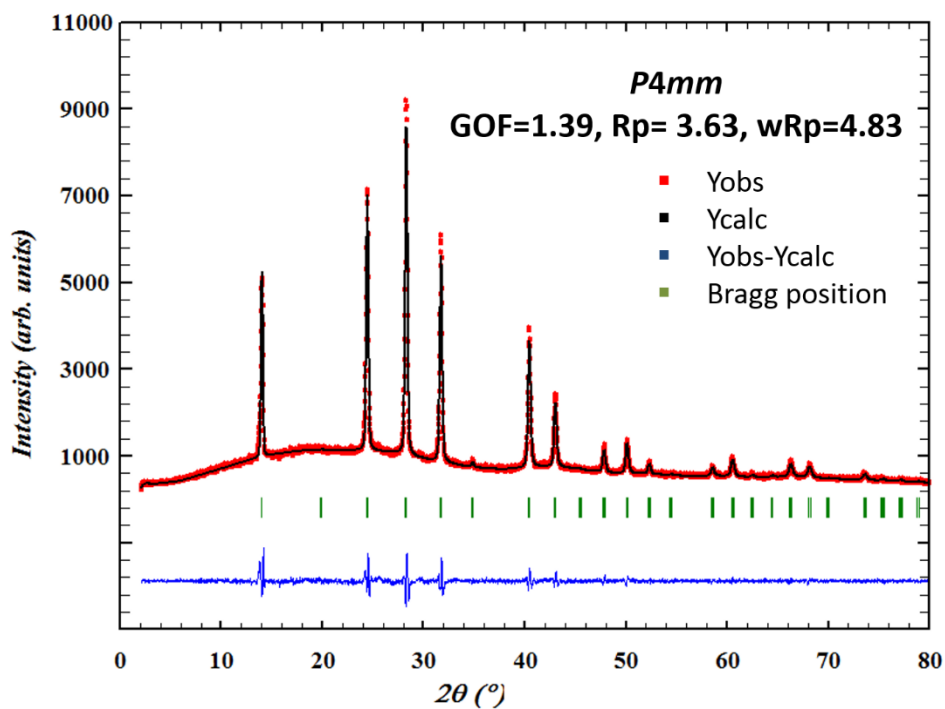
Figure S9. Observed and calculated diffraction profiles from the Rietveld refinement of compound $(MA)_{0.6}(en)_{0.4}(Sn)_{0.72}(I)_{2.84,}$ (Cu Kα).
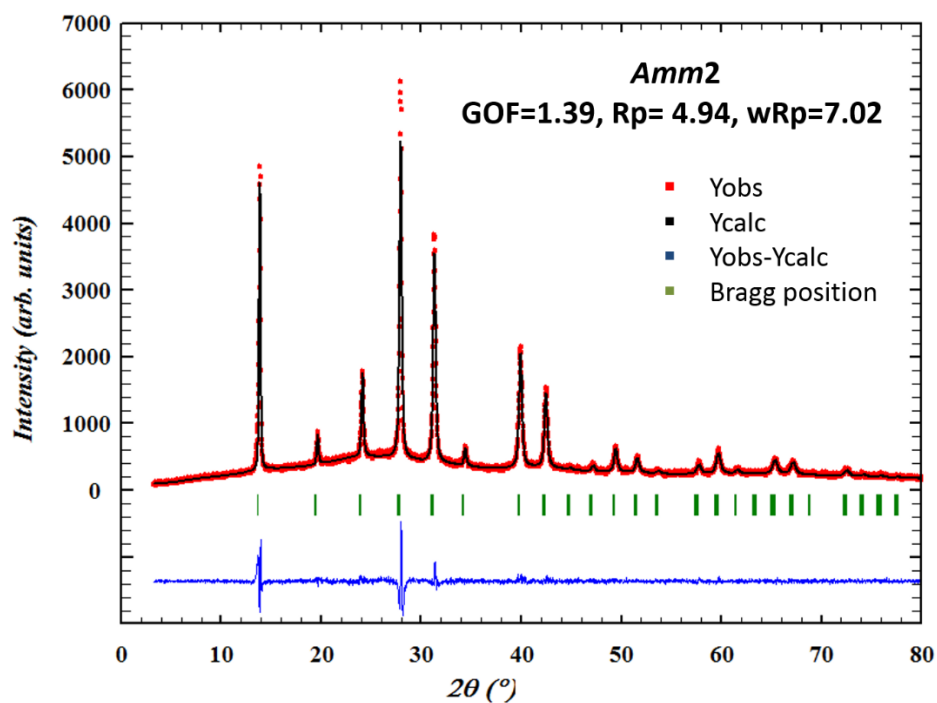
Figure S10. Observed and calculated diffraction profiles from the Rietveld refinement of compound $(FA)_{0.71}(en)_{0.29}(Pb)_{0.797}(I)_{2.884,}$ (Cu Kα).

Table S2. Comparison of the refined unit cell dimension of $(MA)_{1-x}(en)_x(Sn)_{1-0.7x}(I)_{3-0.4x}$ materials along with their calculated band gaps. The increase of the *en* concentration leads to an increase to the unit cell dimension and the observed band gap for all materials.

| MASnI$_3$ + *en*%	Unit cell parameters a, b, c (Å)	Unit cell Volume (Å³)	Band gap (eV)
0	6.2360(3), 6.2360(3), 6.2430(7)	242.77(8)	1.21 (black cr.)
5	6.244(1), 6.244(1), 6.244(2)	243.5(3)	1.25 >>
9	6.2509(3), 6.2509(3), 6.2493(6)	244.18(8)	1.28 >>
21	6.2605(2), 6.2605(2), 6.2738(5)	245.89(6)	1.35 >>
24	6.267(1), 6.267(1), 6.282(2)	246.7(3)	1.42 >>
36	6.2995(3), 6.2995(3), 6.2972(3)	249.90(6)	1.45 >>
40	6.2994(8), 6.2994(8), 6.305(2)	250.2(2)	1.51 >>

Table S3. Comparison of the refined unit cell dimension of $(FA)_{1-x}(en)_x(Pb)_{1-0.7x}(I)_{3-0.4x}$ materials along with their calculated band gaps. The increase of the *en* concentration leads to an increase to the unit cell dimension and the observed band gap for all materials.

FAPbI$_3$ + *en*%	Unit cell parameters axbxc (Å)	Unit cell Volume Normalized (Å³)	Band gap (eV)
0	6.352(1), 6.358(1), 6.348(1)	256.4(2)	1.44 (black cr.)
7	6.358(1), 6.355(2), 6.362(2)	257.1(3)	1.53 >>
11	6.3637(5), 6.3782(7), 6.3505(7)	257.8(1)	1.57 >>
21	6.3766(7), 6.371(3), 6.385(3)	259.4(5)	1.67 >>
27	6.3808(8), 6.386(3), 6.377(3)	259.9(4)	1.69 >>
29	6.3817(7), 6.3924(7), 6.3740(7)	260.0(1)	1.71 >>
39	9.038(2), 9.038(2), 12.807(5)	262(2)	1.94 (dark red)

Table S4. Comparison of the refined unit cell dimension of $(MA)_{1-x}(en)_x(Pb)_{1-0.7x}(I)_{3-0.4x}$ materials along with their calculated band gaps. The increase of the *en* concentration leads to an increase to the unit cell dimension and the observed band gap for all materials.

$MAPbI_3$ + *en*%	Unit cell parameters axbxc (Å)	Unit cell Volume Normalized (Å³)	Band gap (ev)
0	8.8617(3), 8.8617(3), 12.6492(5)	248.3(2)	1.52 (black cr.)
3	8.8814(4), 8.8814(4), 12.6558(8)	249.5(3)	1.56 >>
10	6.306(1), 6.306(1), 6.296(2)	250.3(3)	1.65 >>
29	6.314(3), 6.314(3), 6.324(7)	252.1(9)	1.73 >>
35	6.3472(8), 6.3472(8), 6.333(2)	255.2(2)	1.85 (dark red)
40	6.352(1), 6.352(1), 6.364(2)	256.8(3)	2 (red)
44	6.3814(2), 6.3814(2), 6.3940(5)	260.38(6)	2.1 (orange)

^{1}H-NMR Spectroscopy
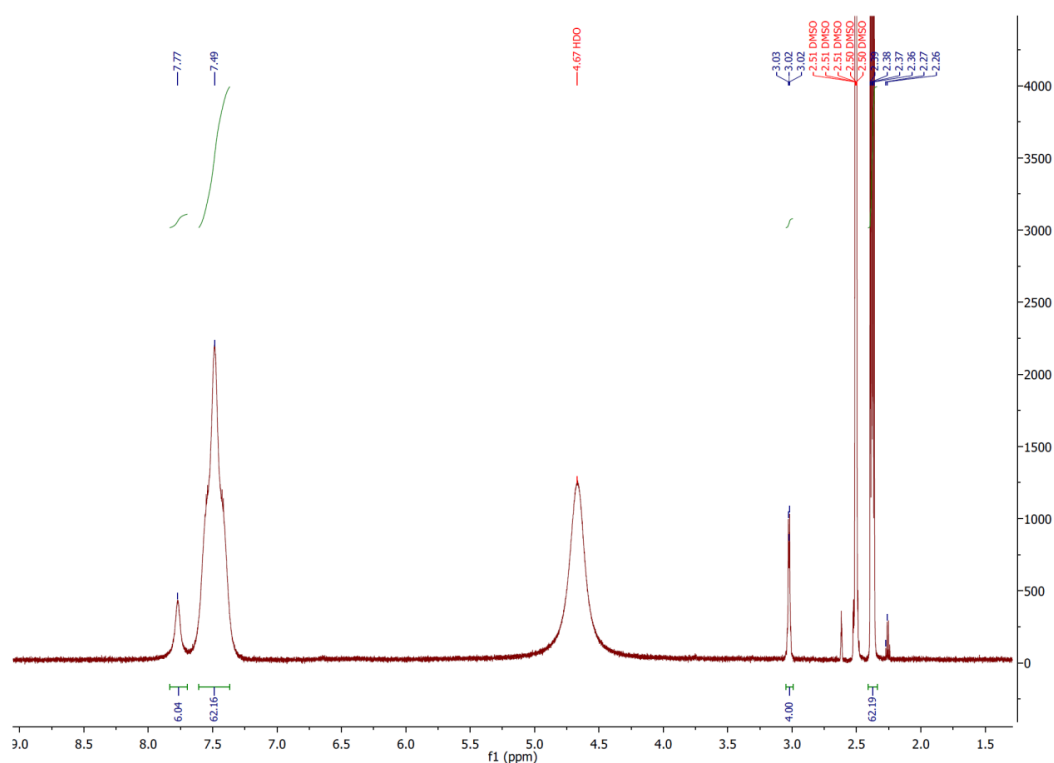
Figure S11. ^{1}H NMR spectrum of the $(MA)_{0.95}(en)_{0.05}(Sn)_{0.965}(I)_{2.98}$ compound in DMSO-d_6 (600 MHz).
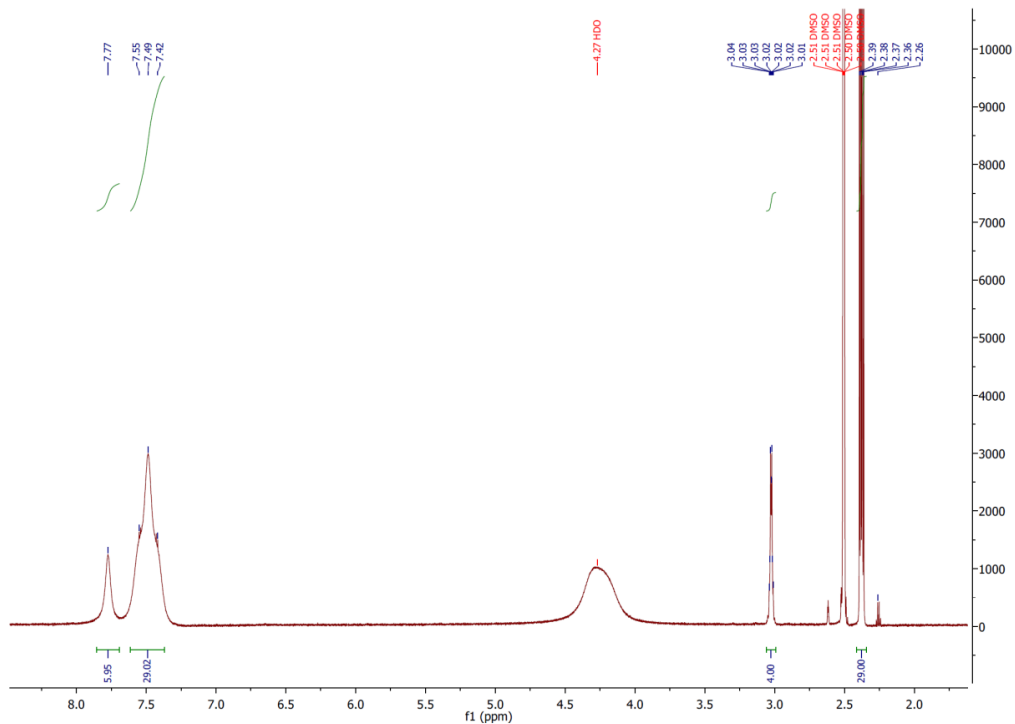
Figure S12. ^{1}H NMR spectrum of the compound $(MA)_{0.91}(en)_{0.09}(Sn)_{0.937}(I)_{2.964}$ in DMSO-d_6 (600 MHz).
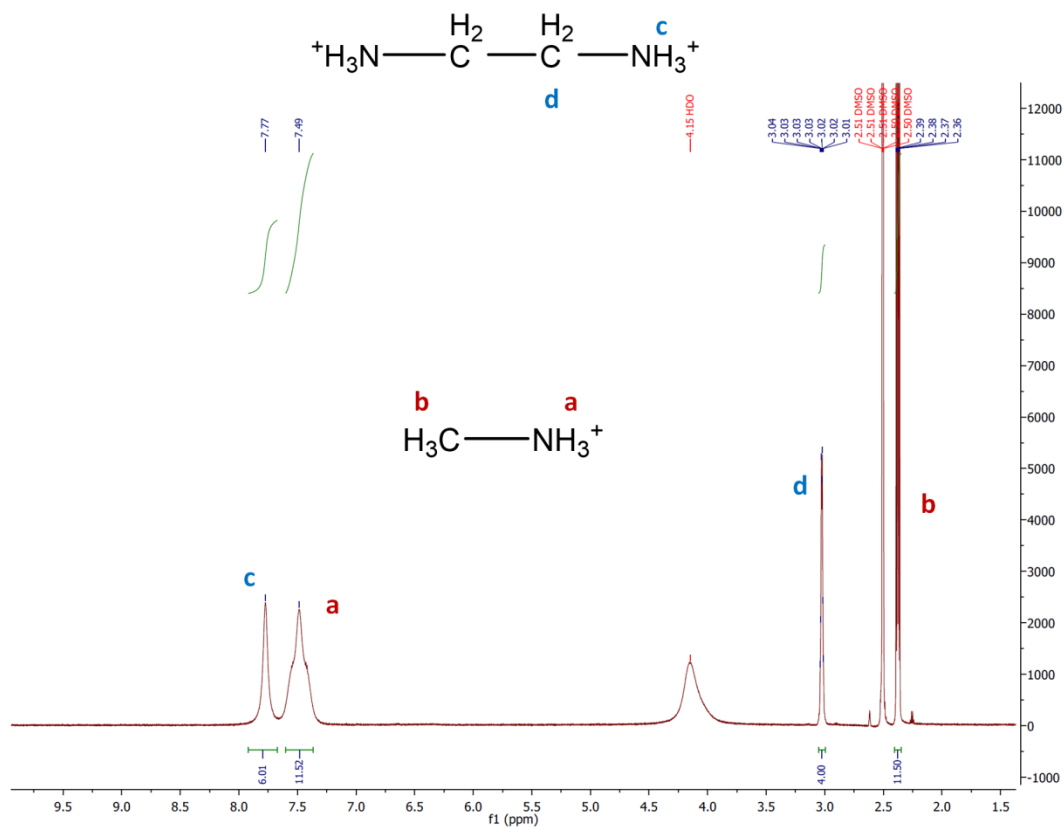
Figure S13. ^{1}H NMR spectrum of the compound $(MA)_{0.79}(en)_{0.21}(Sn)_{0.853}(I)_{2.916}$ in DMSO-d_6 (600 MHz).
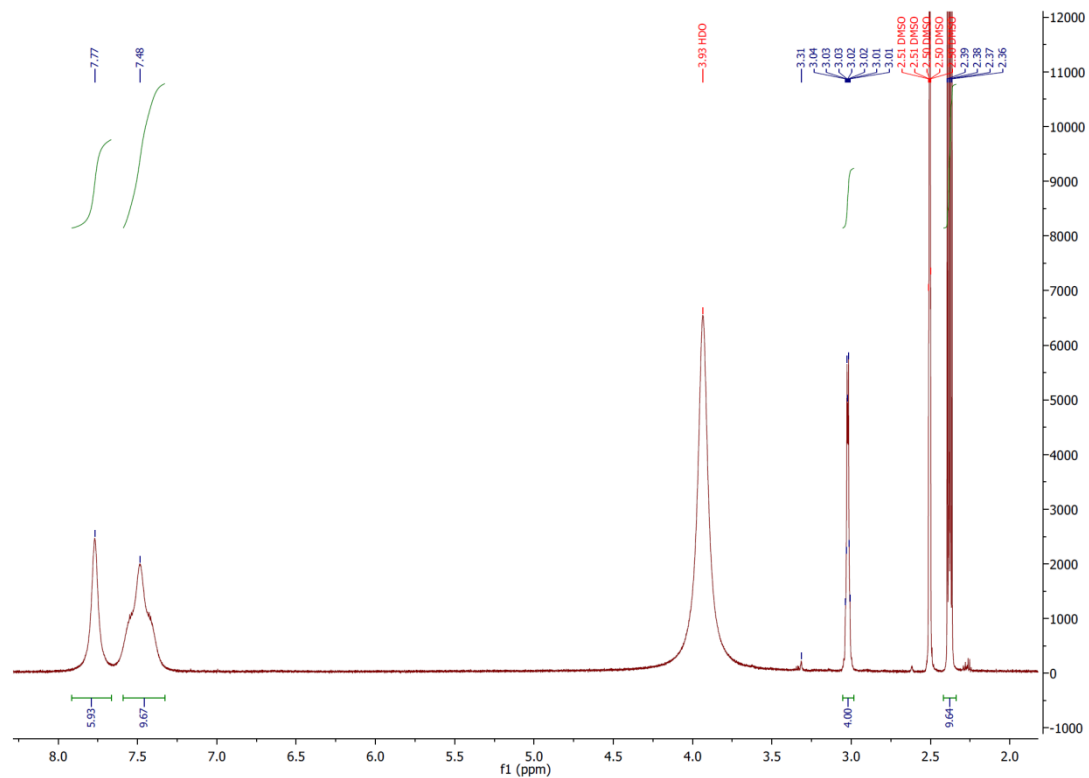
Figure S14. ^{1}H NMR spectrum of the compound $(MA)_{0.76}(en)_{0.24}(Sn)_{0.832}(I)_{2.904}$ in DMSO-d_6 (600 MHz).
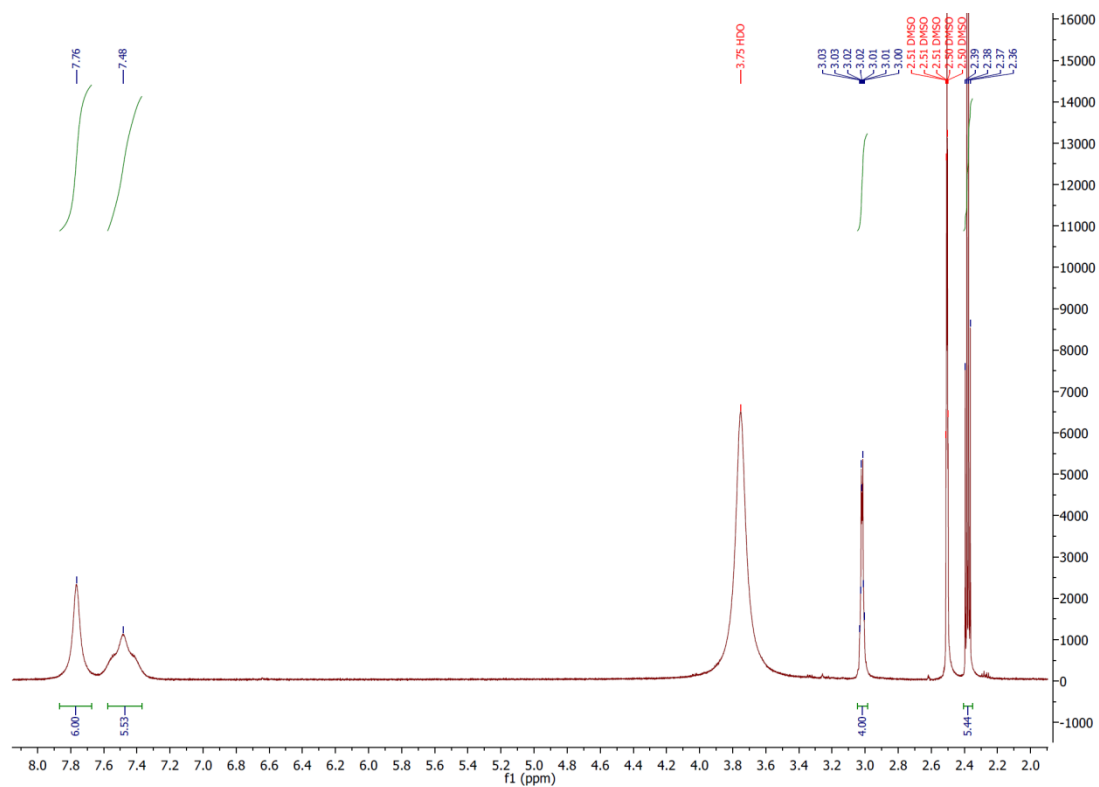
Figure S15. ^{1}H NMR spectrum of the compound $(MA)_{0.64}(en)_{0.36}(Sn)_{0.748}(I)_{2.856}$ in DMSO-d_6 (600 MHz).
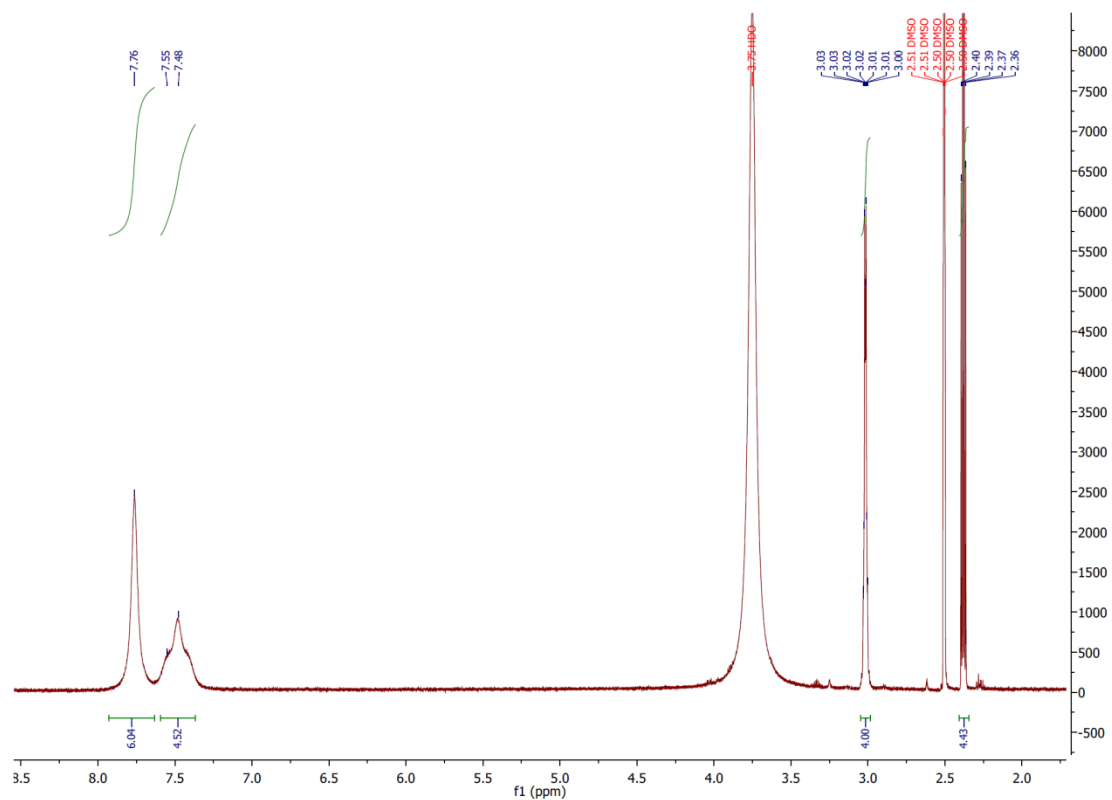
Figure S16. ^{1}H NMR spectrum of the compound $(MA)_{0.6}(en)_{0.4}(Sn)_{0.72}(I)_{2.84}$ in DMSO-d_6 (600 MHz).
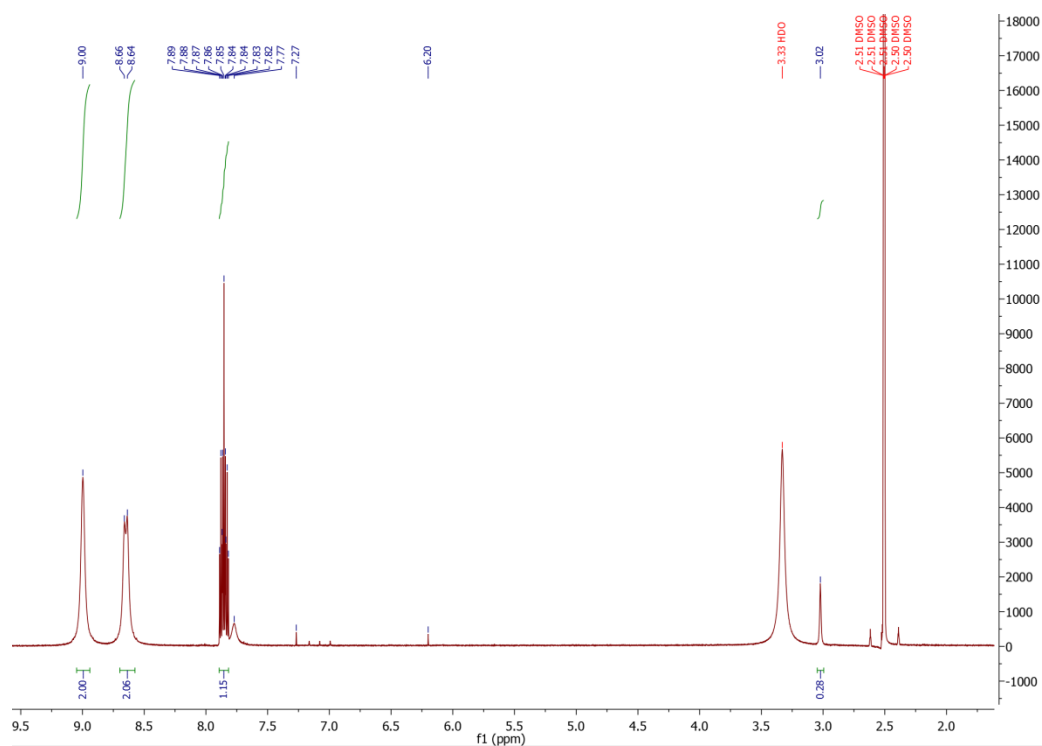
Figure S17. ^{1}H NMR spectrum of the compound $(FA)_{0.93}(en)_{0.07}(Pb)_{0.951}(I)_{2.972}$ in DMSO-d_6 (600 MHz).
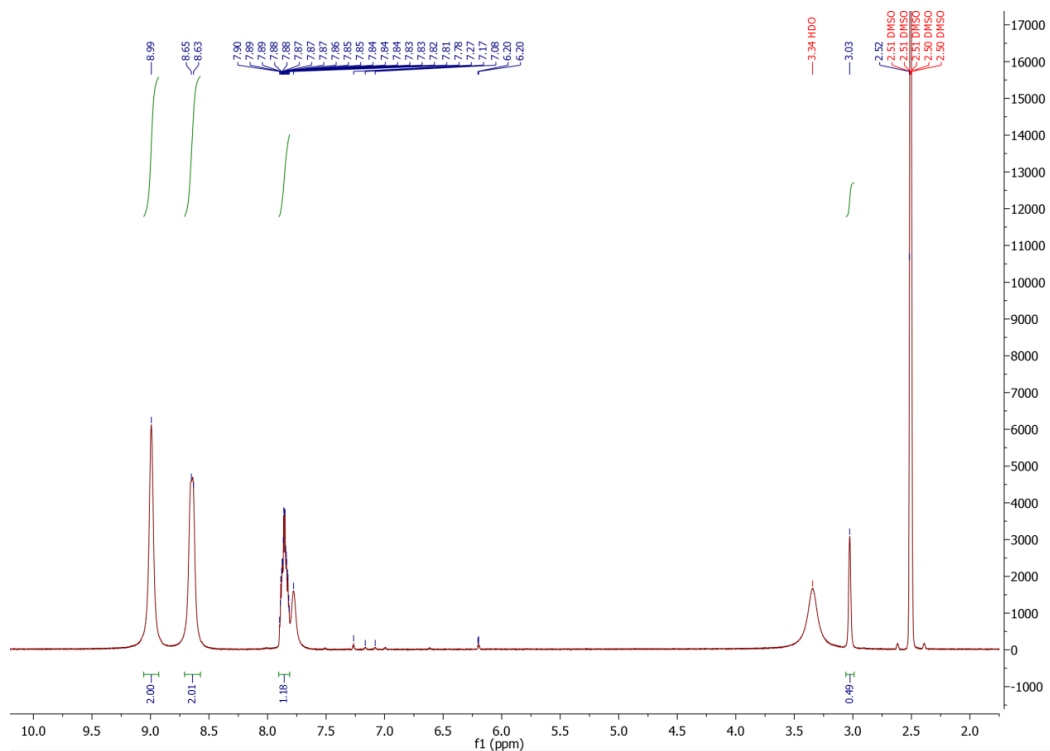
Figure S18. ^{1}H NMR spectrum of the compound with $(FA)_{0.89}(en)_{0.11}(Pb)_{0.923}(I)_{2.956}$ in DMSO-d_6 (600 MHz).
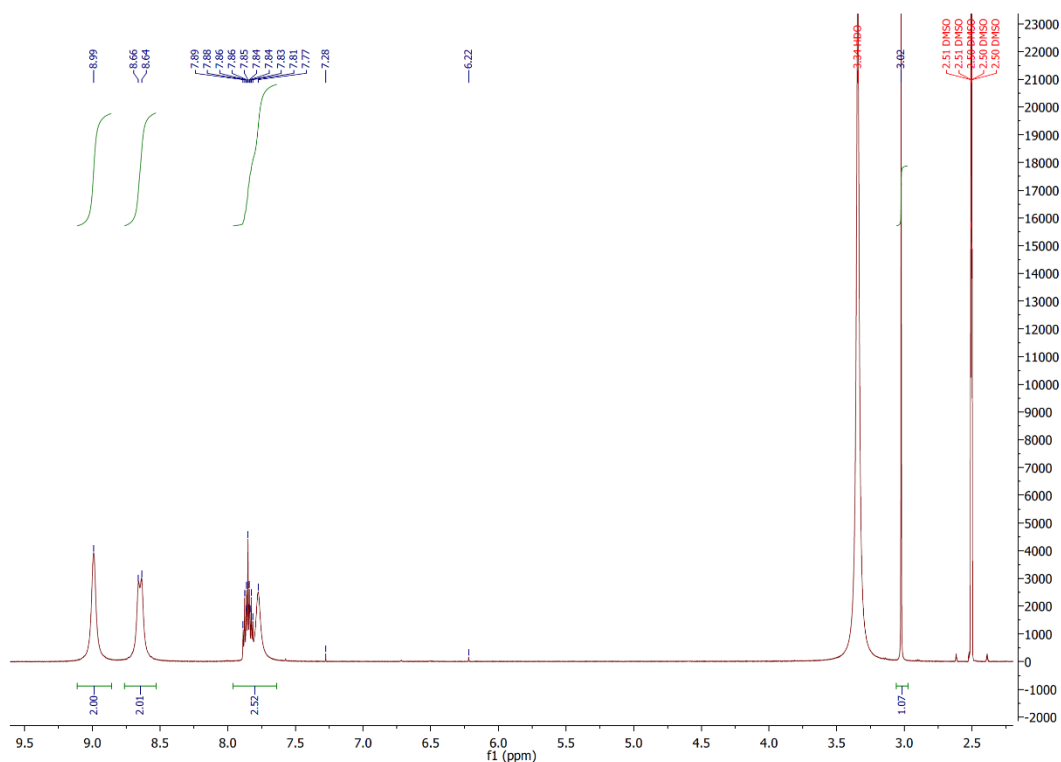
Figure S19. ^{1}H NMR spectrum of the compound $(FA)_{0.79}(en)_{0.21}(Pb)_{0.853}(I)_{2.916}$ in DMSO-d_6 (600 MHz), dried at 100 ^{0}C.
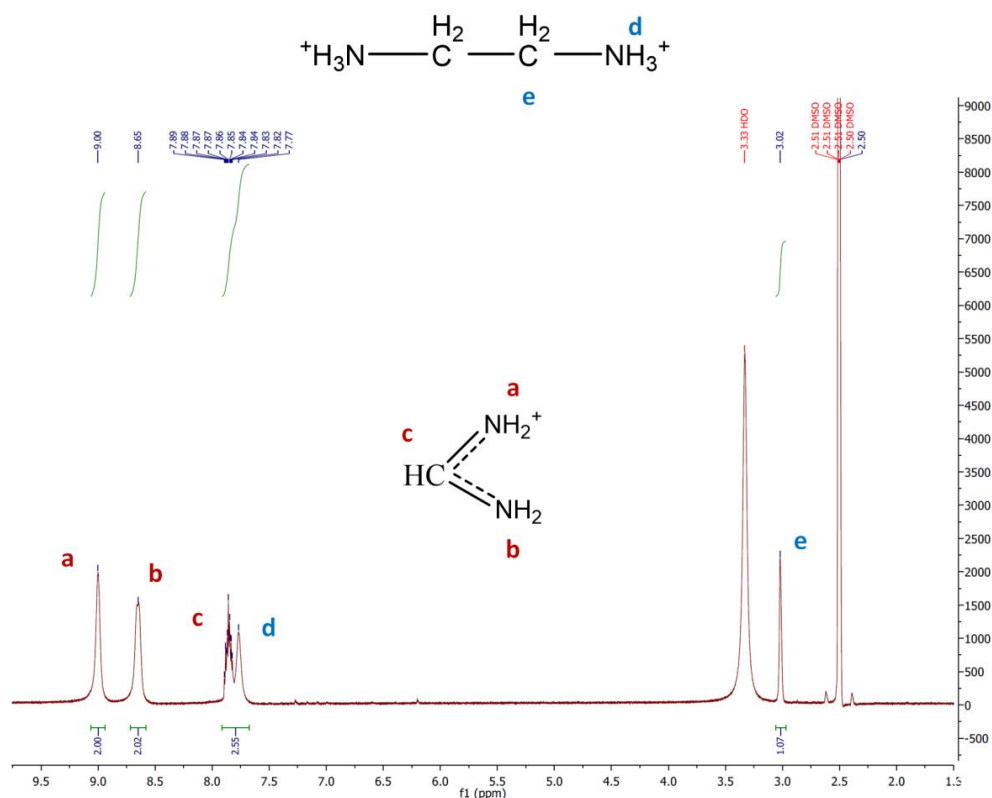
Figure S20. ^{1}H NMR spectrum of the compound $(FA)_{0.79}(en)_{0.21}(Pb)_{0.853}(I)_{2.916}$ in DMSO-d_6 (600 MHz), dried at 110 ^{0}C. Apparently comparing the NMR spectra of the materials dried at 100 ^{0}C and 110 ^{0}C, the H_3PO_2 peaks are gradually diminishing and disappeared, while the *en* and FA peaks are still the same, (integration of *en* and FA was the same). This result indicates that the residual solvent peaks are due to traces of H_3PO_2 left after the drying process.
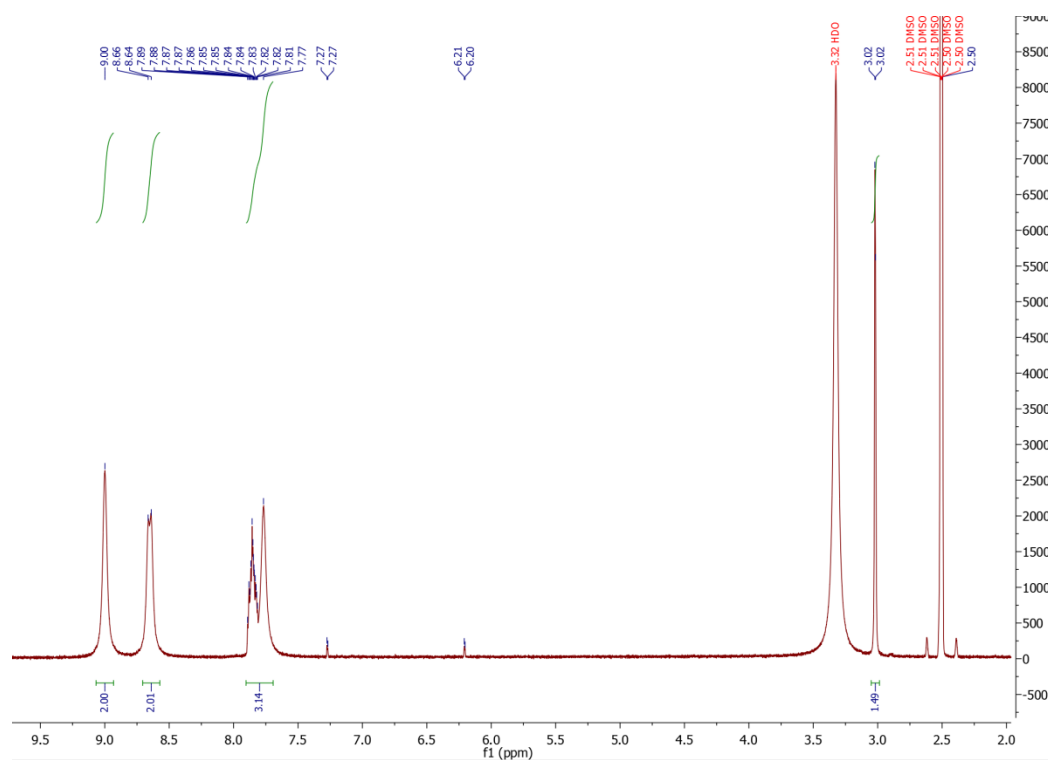
Figure S21. ^{1}H NMR spectrum of the compound $(FA)_{0.73}(en)_{0.27}(Pb)_{0.811}(I)_{2.892}$ in DMSO-d_6 (600 MHz).
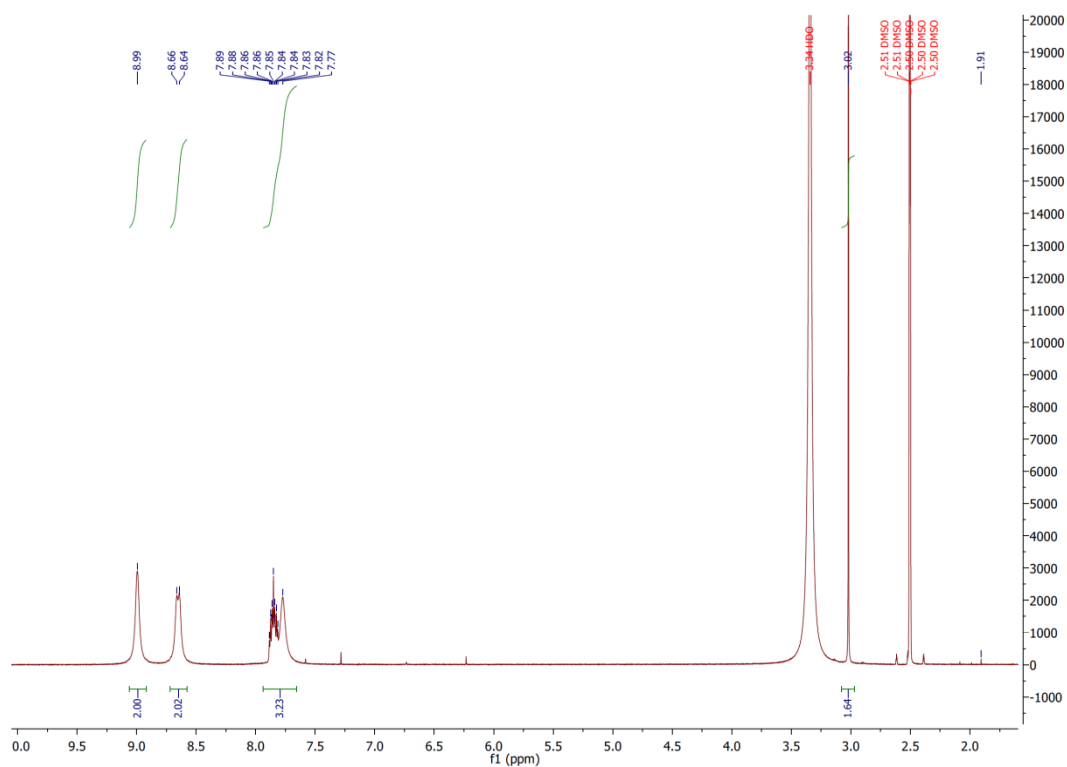
Figure S22. ^{1}H NMR spectrum of the compound $(FA)_{0.71}(en)_{0.29}(Pb)_{0.797}(I)_{2.884}$ in DMSO-d_6 (600 MHz).
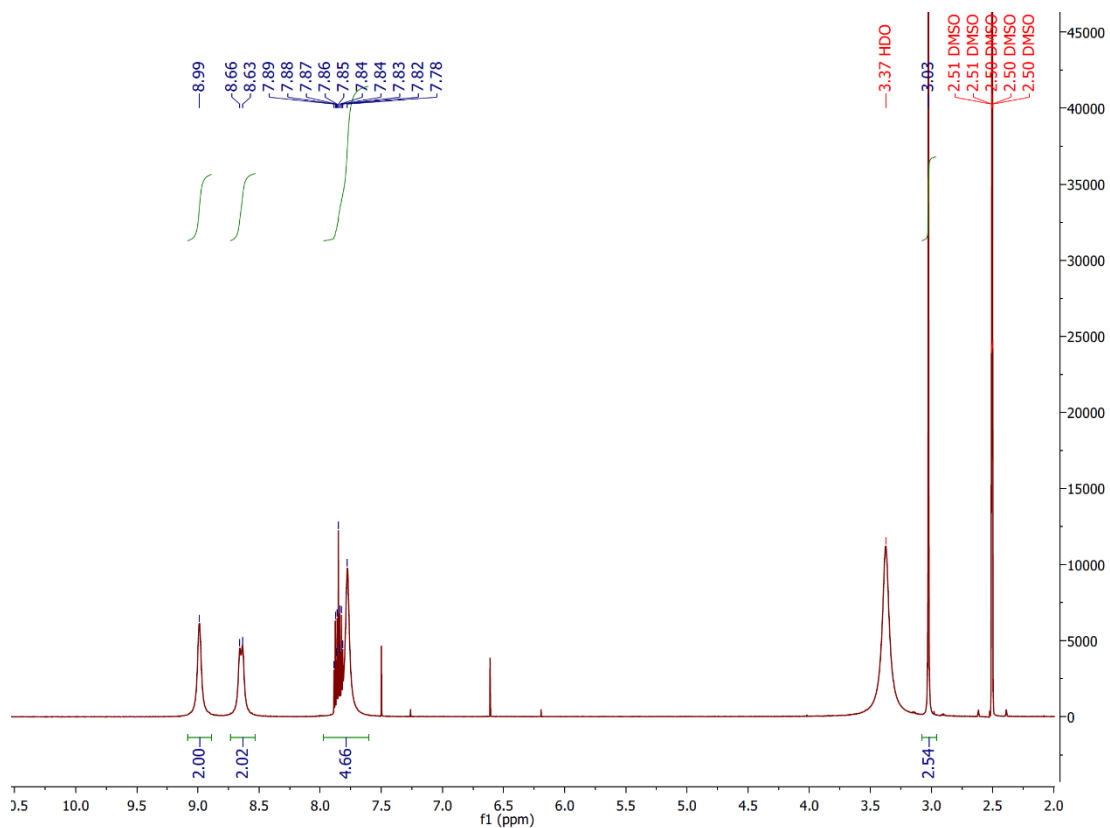
Figure S23. ^{1}H NMR spectrum of the compound $(FA)_{0.61}(en)_{0.39}(Pb)_{0.727}(I)_{2.844}$ in DMSO-d_6 (600 MHz), dried at 100 ^{0}C.
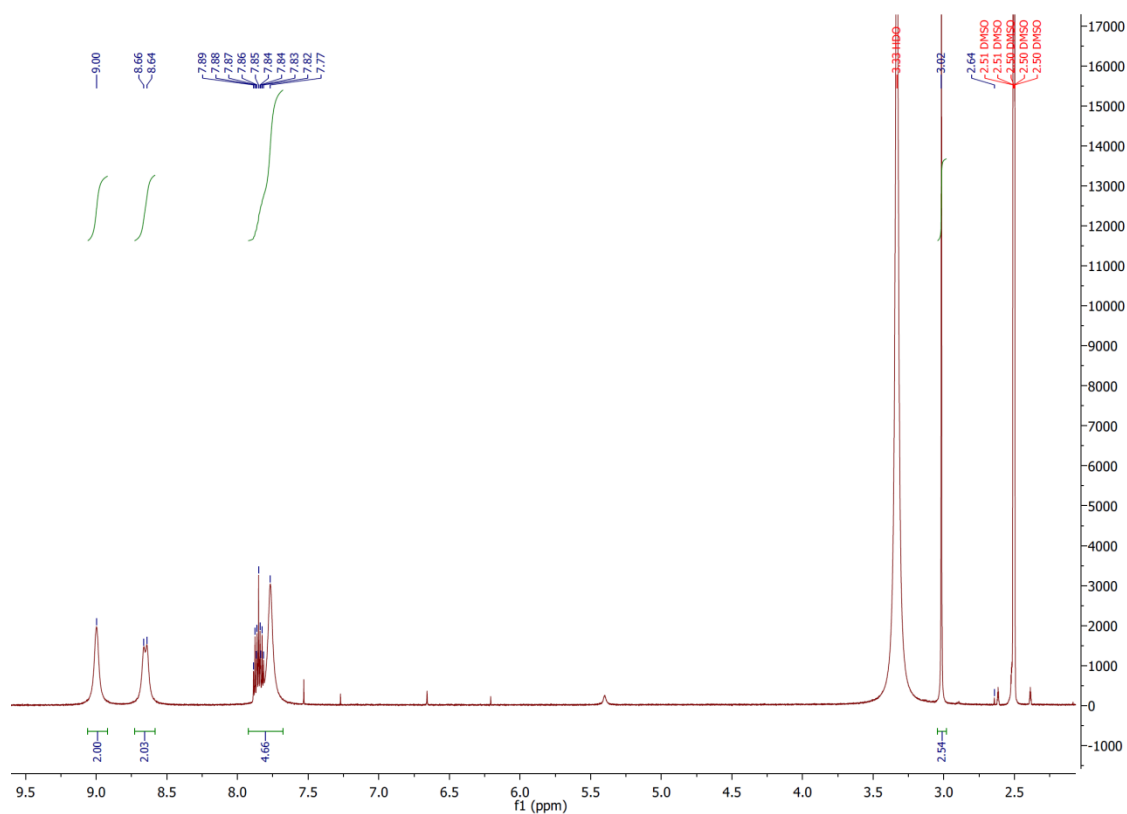
Figure S24. ^{1}H NMR spectrum of the compound $(FA)_{0.61}(en)_{0.39}(Pb)_{0.727}(I)_{2.844}$ in DMSO-d_6 (600 MHz), dried at 110 ^{0}C.
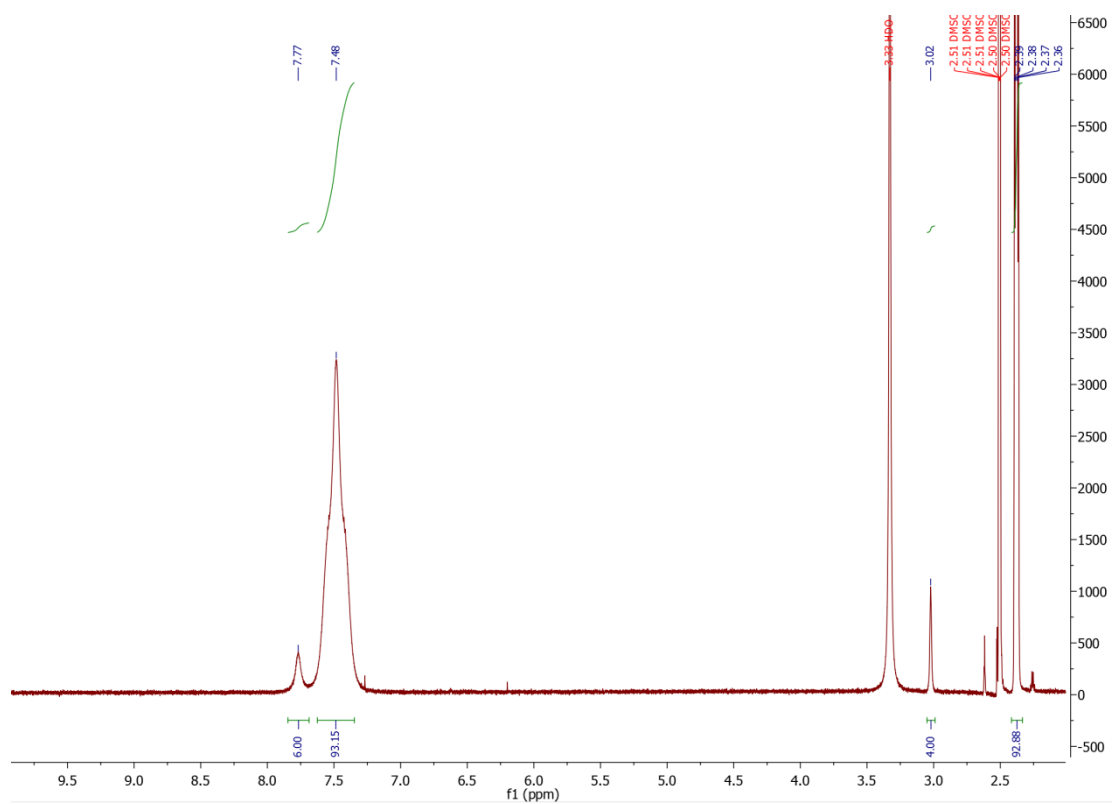
Figure S25. ^{1}H NMR spectrum of the compound $(MA)_{0.97}(en)_{0.03}(Pb)_{0.979}(I)_{2.988}$ in DMSO-d_6 (600 MHz).
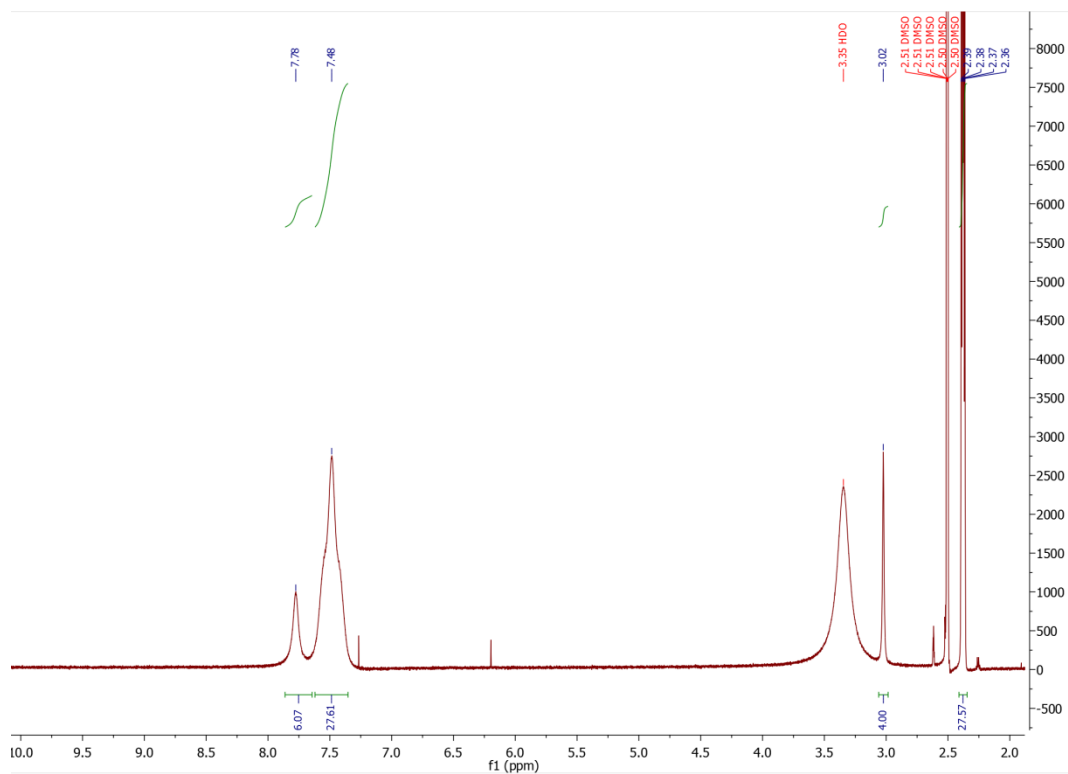
Figure S26. ^{1}H NMR spectrum of the compound $(MA)_{0.9}(en)_{0.1}(Pb)_{0.93}(I)_{2.96}$ in DMSO-d_6 (600 MHz). The peaks at 7.79 and 7.49 ppm have been integrated together due to overlap. The peaks at 6.23 and 7.28 ppm correspond to residual solvent peaks from the stabilizer of HI (H_3PO_2).
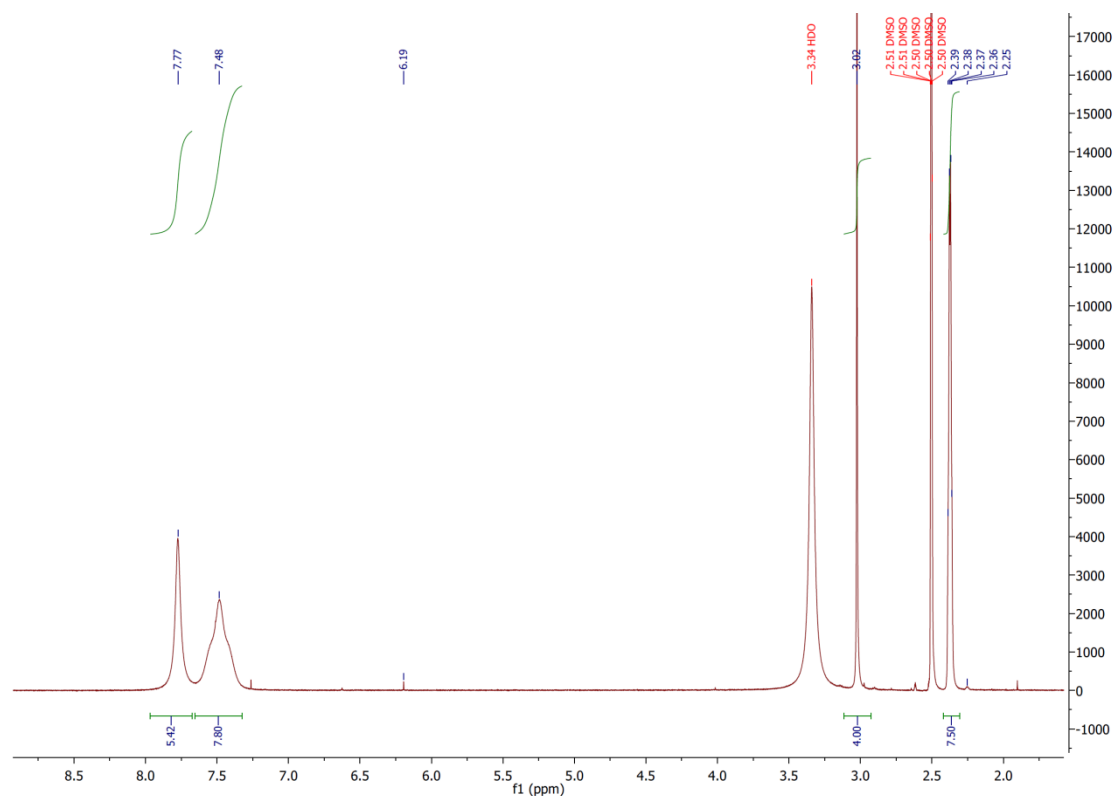
Figure S27. ^{1}H NMR spectrum of the compound $(MA)_{0.71}(en)_{0.29}(Pb)_{0.797}(I)_{2.884}$ in DMSO-d_6 (600 MHz).
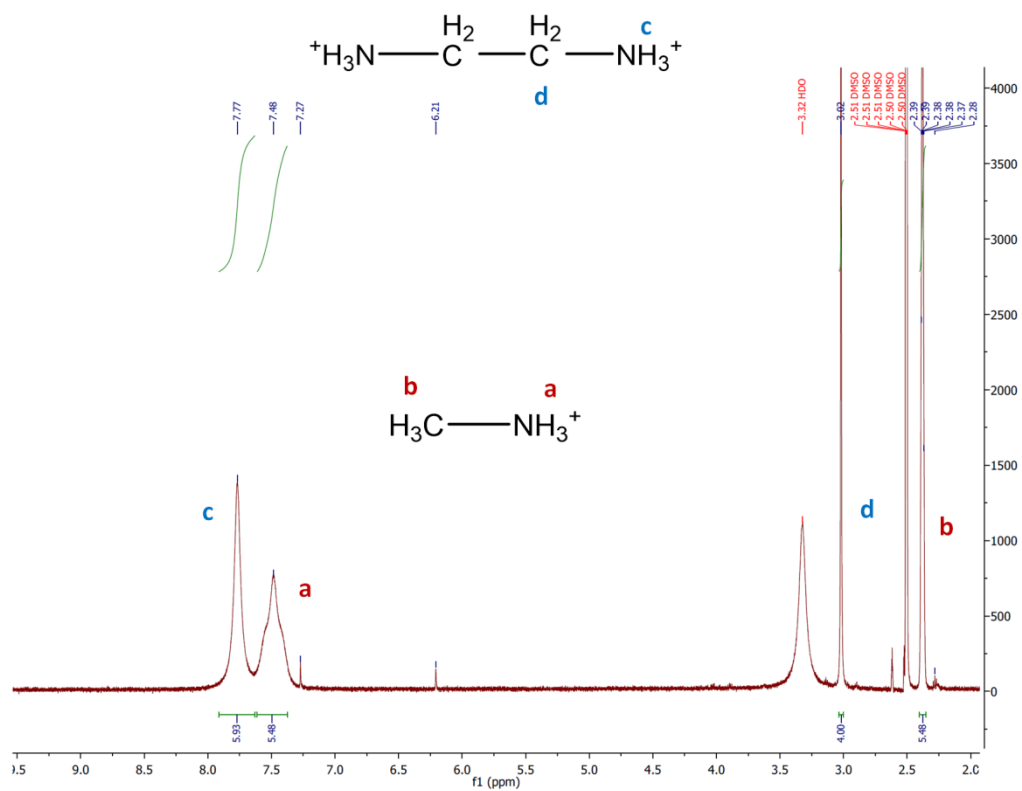
Figure S28. ^{1}H NMR spectrum of the compound $(MA)_{0.65}(en)_{0.35}(Pb)_{0.755}(I)_{2.86}$ in DMSO-d_6 (600 MHz).
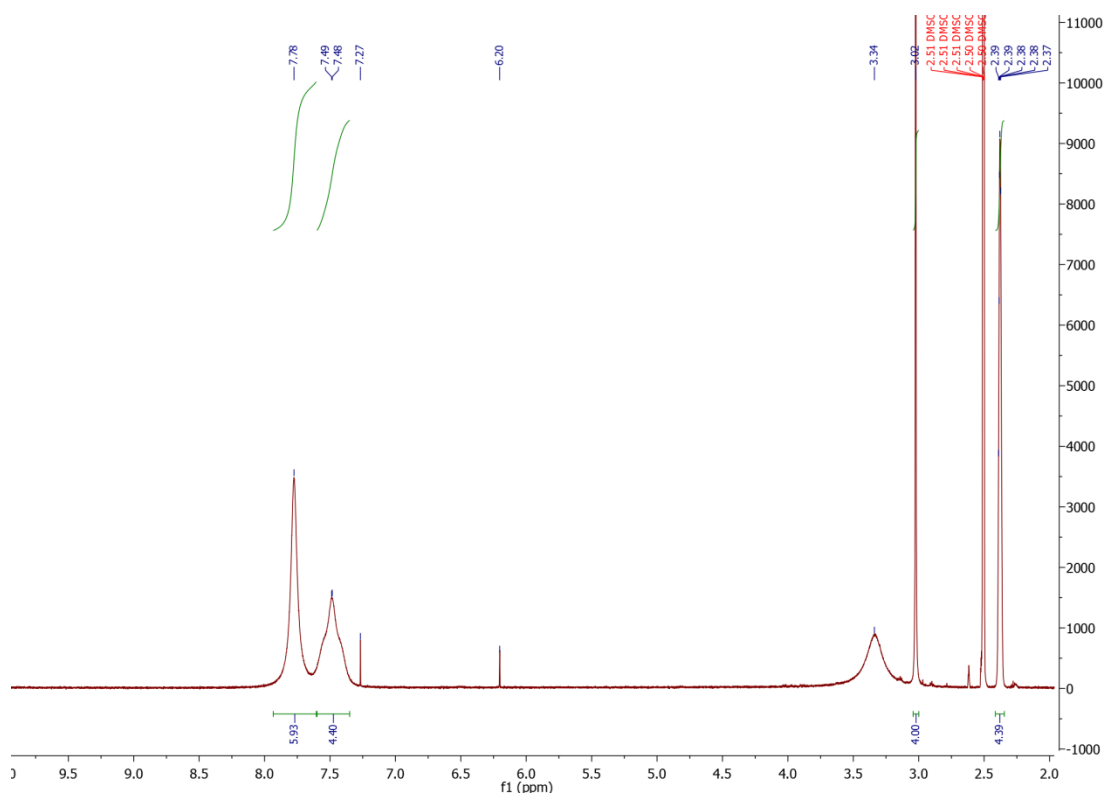
Figure S29. ^{1}H NMR spectrum of the compound $(MA)_{0.6}(en)_{0.4}(Pb)_{0.72}(I)_{2.84}$ in DMSO-d_6 (600 MHz).
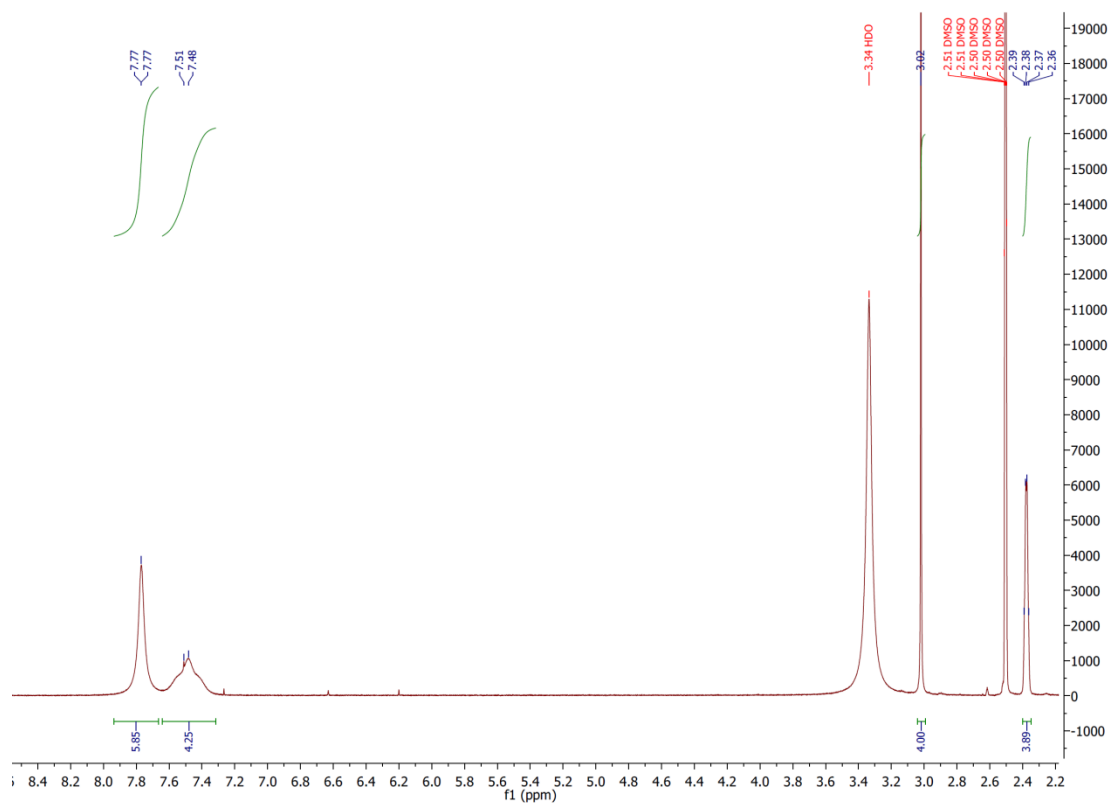
Figure S30. ^{1}H NMR spectrum of the compound $(MA)_{0.56}(en)_{0.44}(Pb)_{0.692}(I)_{2.824}$ in DMSO-d_6 (600 MHz).

SEM measurements
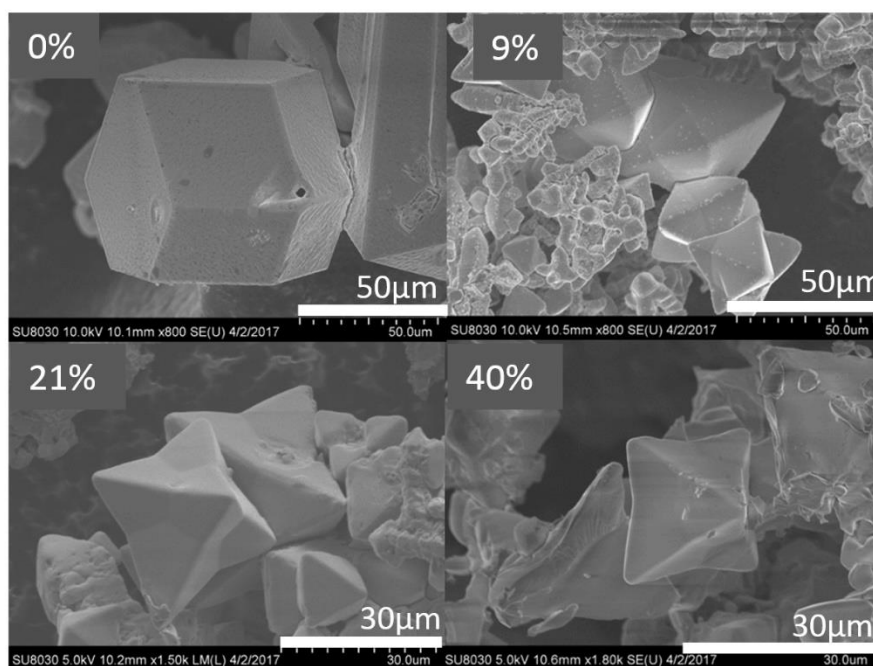
Figure S31. Representative SEM images of pristine perovskite α MASnI$_3$, hollow $(MA)_{0.91}(en)_{0.09}(Sn)_{0.937}(I)_{2.964}$, $(MA)_{0.79}(en)_{0.21}(Sn)_{0.853}(I)_{2.916}$ and $(MA)_{0.6}(en)_{0.4}(Sn)_{0.72}(I)_{2.84}$.
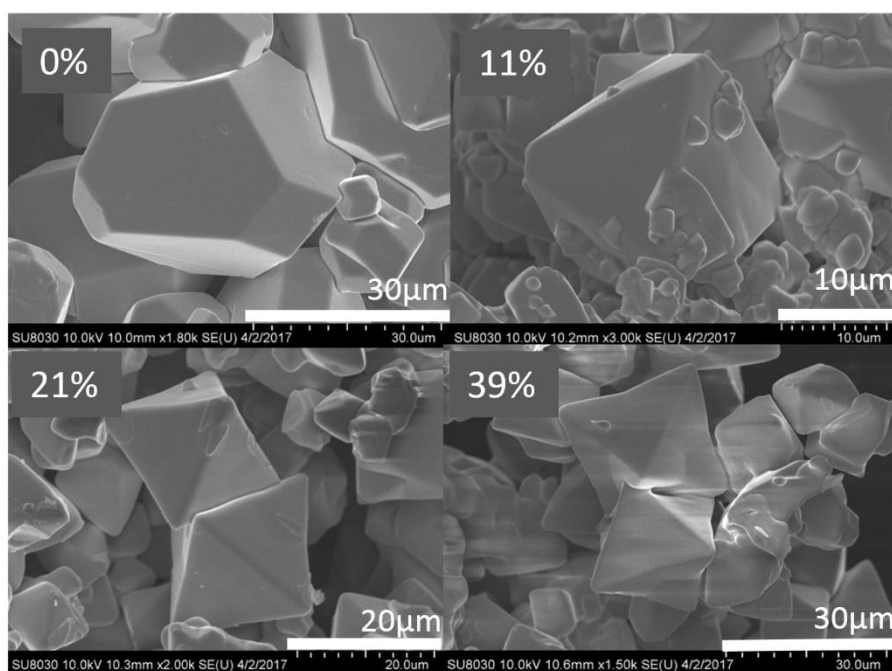
Figure S32. Representative SEM images of pristine perovskite α FAPbI$_3$, hollow (FA)$_{0.89}$(*en*)$_{0.11}$(Pb)$_{0.923}$(I)$_{2.956}$, (FA)$_{0.79}$(*en*)$_{0.21}$(Pb)$_{0.853}$(I)$_{2.916}$ and (FA)$_{0.61}$(*en*)$_{0.39}$(Pb)$_{0.727}$(I)$_{2.844}$.
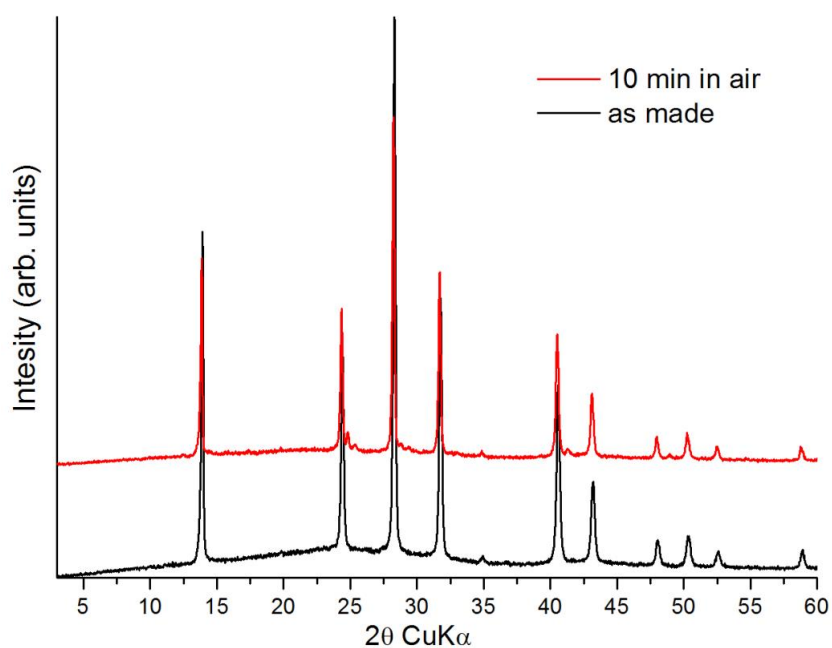
Figure S33. Experimental powder X-ray diffraction (PXRD) patterns of the freshly prepared pristine compound α-MASnI$_3$ and after 10 min exposure to air.
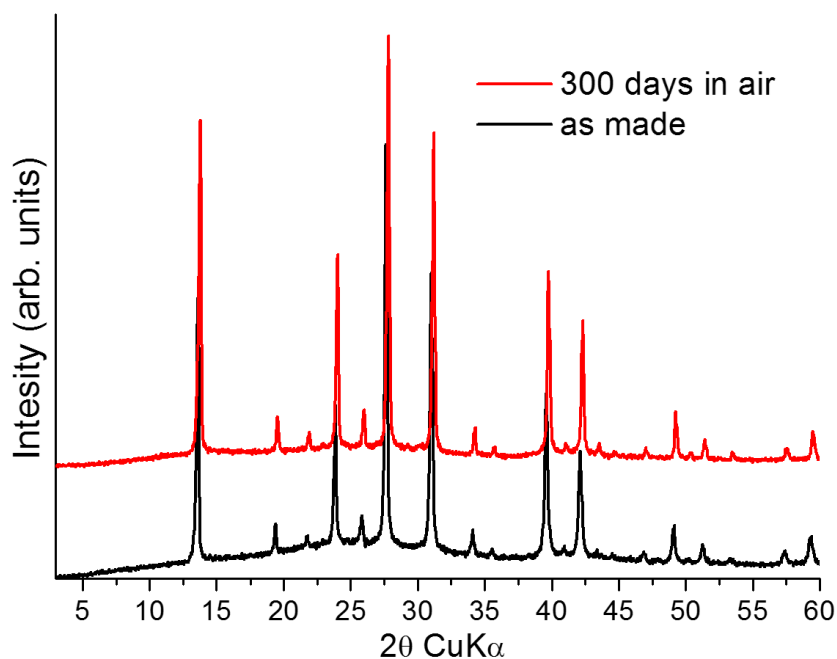
Figure S34. Experimental powder X-ray diffraction (PXRD) patterns of the freshly prepared compound $(FA)_{0.61}(en)_{0.39}(Pb)_{0.727}(I)_{2.844}$ and after 300 days exposure to air. The humidity in the laboratory ranged during this period from 10% in the winter to 80% in the summer time.
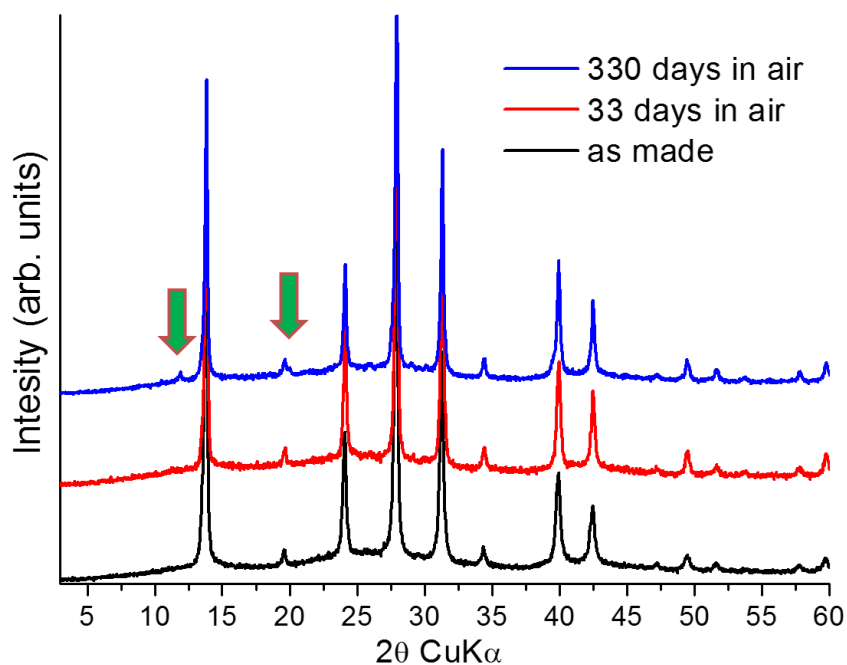
Figure S35. Experimental powder X-ray diffraction (PXRD) patterns of the freshly prepared compound $(MA)_{0.56}(en)_{0.44}(Pb)_{0.692}(I)_{2.824}$ and after 33 and 330 days exposure to air. The humidity in the laboratory ranged during this period from 10% in the winter to 80% in the summer time. The green arrows show the appearance of an additional diffraction peak at $2\theta = 11.9^0$ and a smaller one, appearing as a "shoulder" at $2\theta = 20^0$ coming from crystalline decomposition byproduct/s.

Crystallographic tables

1. Structure: $(FA)_{0.61}(en)_{0.39}(Pb)_{0.727}(I)_{2.844}$

Table S5. Atomic coordinates (x10^4) and equivalent isotropic displacement parameters (Å^2x10^3) for $(FA)_{0.61}(en)_{0.39}(Pb)_{0.727}(I)_{2.844}$ at 293 K with estimated standard deviations in parentheses.

Label	x	y	z	Occupancy	U_{eq}*
I(1)	0	0	12(16)	1	85(1)
Pb(1)	0	0	5063(9)	0.743(6)	57(1)
I(2)	2154(3)	7154(3)	5178(13)	1	121(1)
C	0	5000	160(80)	1	200(20)
N	913(1)	4087(1)	1050(80)	1	200(20)
H(1c)	0	5000	-1343.69	1	244.8
H(1n)	960.86	4039.14	2400.71	1	244.8
H(2n)	1477.27	3522.73	285.68	1	244.8

*U_{eq} is defined as one third of the trace of the orthogonalized U_{ij} tensor.

Table S6. Anisotropic displacement parameters (Å^2x10^3) for $(FA)_{0.61}(en)_{0.39}(Pb)_{0.727}(I)_{2.844}$ at 293 K with estimated standard deviations in parentheses.

Label	U_{11}	U_{22}	U_{33}	U_{12}	U_{13}	U_{23}
I(1)	108(2)	108(2)	40(2)	0	0	0
Pb(1)	58(1)	58(1)	56(2)	0	0	0
I(2)	133(2)	133(2)	96(2)	78(2)	5(5)	5(5)

The anisotropic displacement factor exponent takes the form: $-2\pi^2[h^2a^{*2}U_{11} + \ldots + 2hka^*b^*U_{12}]$.

Table S7. Bond lengths [Å] for $(FA)_{0.61}(en)_{0.39}(Pb)_{0.727}(I)_{2.844}$ at 293 K with estimated standard deviations in parentheses.

Label	Distances
I(1)-Pb(1)#1	3.169(12)
I(1)-Pb(1)	3.235(12)
I(1)-N	3.845(9)
I(1)-N#2	3.845(9)
I(1)-N#3	3.845(9)
I(1)-N#4	3.845(9)
Pb(1)-I(2)#5	3.229(3)
Pb(1)-I(2)#6	3.229(3)
Pb(1)-I(2)#7	3.229(3)
Pb(1)-I(2)#8	3.229(3)

Symmetry transformations used to generate equivalent atoms:

(1) x,y,z-1 (2) -x,-y,z (3) -y,x,z (4) y,-x,z (5) x,y-1,z (6) -x,-y+1,z (7) -y+1,x,z (8) y-1,-x,z (9) y,-x+1,z (10) x,y,z+1 (11) x,y+1,z (12) x+1/2,-y+1/2,z

Table S8. Bond angles [°] for $(FA)_{0.61}(en)_{0.39}(Pb)_{0.727}(I)_{2.844}$ at 293 K with estimated standard deviations in parentheses.

Label	Angles
Pb(1)#1-I(1)-Pb(1)	180.0(5)
Pb(1)#1-I(1)-N	99.9(8)
Pb(1)#1-I(1)-N#2	99.9(8)
Pb(1)#1-I(1)-N#3	99.9(8)
Pb(1)#1-I(1)-N#4	99.9(8)
Pb(1)-I(1)-N	80.1(8)
Pb(1)-I(1)-N#2	80.1(8)
Pb(1)-I(1)-N#3	80.1(8)
Pb(1)-I(1)-N#4	80.1(8)

Symmetry transformations used to generate equivalent atoms:

(1) x,y,z-1 (2) -x,-y,z (3) -y,x,z (4) y,-x,z (5) x,y-1,z (6) -x,-y+1,z (7) -y+1,x,z (8) y-1,-x,z (9) y,-x+1,z (10) x,y,z+1 (11) x,y+1,z (12) x+1/2,-y+1/2,z

2. Structure: $(FA)_{0.73}(en)_{0.27}(Pb)_{0.811}(I)_{2.892}$

Table S9. Atomic coordinates (x10⁴) and equivalent isotropic displacement parameters ($Å^2$x10³) for $(FA)_{0.73}(en)_{0.27}(Pb)_{0.811}(I)_{2.892}$ at 293 K with estimated standard deviations in parentheses.

Label	x	y	z	Occupancy	U_{eq}*
Pb(1)	0	0	-45(5)	0.960(17)	33(4)
I(1)	5000	0	-330(12)	1	49(7)
I(2)	0	7465(18)	2450(13)	1	83(4)
C(1)	5000	5000	850(120)	1	160(40)
N(1)	5000	6309(1)	240(120)	1	160(40)
H(1c1)	5000	5000	1913.24	1	197
H(1n1)	5000	6393.19	-724.99	1	197
H(2n1)	5000	7100.66	791.37	1	197

*U_{eq} is defined as one third of the trace of the orthogonalized U_{ij} tensor.

Table S10. Anisotropic displacement parameters ($Å^2$x10³) for $(FA)_{0.73}(en)_{0.27}(Pb)_{0.811}(I)_{2.892}$ at 293 K with estimated standard deviations in parentheses.

Label	U_{11}	U_{22}	U_{33}	U_{12}	U_{13}	U_{23}
Pb(1)	30(2)	41(8)	29(7)	0	0	0
I(1)	22(3)	79(15)	47(13)	0	0	0
I(2)	118(4)	76(9)	55(8)	0	0	53(2)

The anisotropic displacement factor exponent takes the form: $-2\pi^2[h^2a^{*2}U_{11} + ... + 2hka^*b^*U_{12}]$.

Table S11. Bond lengths [Å] for (FA)$_{0.73}$(*en*)$_{0.27}$(Pb)$_{0.811}$(I)$_{2.892}$ at 293 K with estimated standard deviations in parentheses.

Label	Distances
Pb(1)-I(1)#1	3.193(2)
Pb(1)-I(1)	3.193(2)
Pb(1)-I(2)#2	3.203(14)
Pb(1)-I(2)#3	3.164(14)
Pb(1)-I(2)#4	3.203(14)
Pb(1)-I(2)#5	3.164(14)
I(1)-N(1)#2	3.362(16)
I(1)-N(1)#3	4.16(10)
I(1)-N(1)#6	3.362(16)
I(1)-N(1)#7	4.16(10)

Symmetry transformations used to generate equivalent atoms:

(1) x-1,y,z (2) x,y-1,z (3) x,y-1/2,z-1/2 (4) -x,-y+1,z (5) -x,-y+1/2,z-1/2 (6) -x+1,-y+1,z (7) -x+1,-y+1/2,z-1/2 (8) -x,-y+3/2,z+1/2 (9) -x+1,-y+3/2,z+1/2 (10) x+1,y,z (11) x,y+1,z (12) x,y+1/2,z+1/2 (13) -x,-y+3/2,z-1/2 (14) -x+1,-y+3/2,z-1/2

Table S12. Bond angles [°] for $(FA)_{0.73}(en)_{0.27}(Pb)_{0.811}(I)_{2.892}$ at 293 K with estimated standard deviations in parentheses.

Label	Angles
I(1)#1-Pb(1)-I(1)	170.8(3)
I(1)#1-Pb(1)-I(2)#2	93.24(14)
I(1)#1-Pb(1)-I(2)#3	86.71(15)
I(1)#1-Pb(1)-I(2)#4	93.24(14)
I(1)#1-Pb(1)-I(2)#5	86.71(15)
I(1)-Pb(1)-I(2)#2	93.24(14)
I(1)-Pb(1)-I(2)#3	86.71(15)
I(1)-Pb(1)-I(2)#4	93.24(14)
I(1)-Pb(1)-I(2)#5	86.71(15)
I(2)#2-Pb(1)-I(2)#3	179.1(4)

Symmetry transformations used to generate equivalent atoms:

(1) x-1,y,z (2) x,y-1,z (3) x,y-1/2,z-1/2 (4) -x,-y+1,z (5) -x,-y+1/2,z-1/2 (6) -x+1,-y+1,z (7) -x+1,-y+1/2,z-1/2 (8) -x,-y+3/2,z+1/2 (9) -x+1,-y+3/2,z+1/2 (10) x+1,y,z (11) x,y+1,z (12) x,y+1/2,z+1/2 (13) -x,-y+3/2,z-1/2 (14) -x+1,-y+3/2,z-1/2

3. Structure: $(MA)_{0.71}(en)_{0.29}(Pb)_{0.797}(I)_{2.884}$

Table S13. Atomic coordinates ($\times 10^4$) and equivalent isotropic displacement parameters ($\text{Å}^2 \times 10^3$) for $(MA)_{0.71}(en)_{0.29}(Pb)_{0.797}(I)_{2.884}$ at 293 K with estimated standard deviations in parentheses.

Label	x	y	z	Occupancy	U_{eq}^*
Pb(1)	0	0	282(7)	0.847(8)	49(1)
I(1)	0	5000	456(17)	1	139(2)
I(2)	0	0	5320(20)	1	145(2)
N(1)	5000	5000	7240(100)	1	180(20)
C(1)	5000	5000	4870(100)	1	180(20)
H(1c1)	4227.42	6201.53	4368.98	0.125	219.1
H(2c1)	6426.84	5068.31	4368.98	0.125	219.1
H(3c1)	4345.74	3730.16	4368.98	0.125	219.1
H(1n1)	3783.18	5441.85	7702.67	0.125	219.1
H(2n1)	5225.76	3725.28	7702.67	0.125	219.1
H(3n1)	5991.06	5832.87	7702.67	0.125	219.1

$^*U_{eq}$ is defined as one third of the trace of the orthogonalized U_{ij} tensor.

Table S14. Anisotropic displacement parameters ($\text{Å}^2 \times 10^3$) for $(MA)_{0.71}(en)_{0.29}(Pb)_{0.797}(I)_{2.884}$ at 293 K with estimated standard deviations in parentheses.

Label	U_{11}	U_{22}	U_{33}	U_{12}	U_{13}	U_{23}
Pb(1)	50(1)	50(1)	47(1)	0	0	0
I(1)	193(3)	38(2)	186(4)	0	0	0
I(2)	200(3)	200(3)	36(2)	0	0	0

The anisotropic displacement factor exponent takes the form: $-2\pi^2[h^2a^{*2}U_{11} + ... + 2hka^*b^*U_{12}]$.

Table S15. Bond lengths [Å] for $(MA)_{0.71}(en)_{0.29}(Pb)_{0.797}(I)_{2.884}$ at 293 K with estimated standard deviations in parentheses.

Label	Distances
Pb(1)-I(1)#1	3.1700(17)
Pb(1)-I(1)	3.1700(17)
Pb(1)-I(1)#2	3.1700(17)
Pb(1)-I(1)#3	3.1700(17)
Pb(1)-I(2)#4	3.143(14)
Pb(1)-I(2)	3.187(14)
I(1)-N(1)#5	3.76(3)
I(1)-N(1)#4	3.76(3)
N(1)-C(1)	1.50(9)

Symmetry transformations used to generate equivalent atoms:

(1) x,y-1,z (2) -y,x,z (3) -y+1,x,z (4) x,y,z-1 (5) x-1,y,z-1 (6) -x+1,-y+1,z (7) y,-x+1,z (8) x,-y+1,z (9) -x+1,y,z (10) -y+1,-x+1,z (11) y,x,z (12) x,y+1,z (13) x,y,z+1 (14) x+1,y,z+1 (15) -y+1,x,z+1 (16) -y+1,x+1,z+1

Table S16. Bond angles [°] for $(MA)_{0.71}(en)_{0.29}(Pb)_{0.797}(I)_{2.884}$ at 293 K with estimated standard deviations in parentheses.

Label	Angles
I(1)#1-Pb(1)-I(1)	176.0(3)
I(1)#1-Pb(1)-I(1)#2	89.930(11)
I(1)#1-Pb(1)-I(1)#3	89.930(11)
I(1)#1-Pb(1)-I(2)#4	92.0(2)
I(1)#1-Pb(1)-I(2)	88.0(2)
I(1)-Pb(1)-I(1)#2	89.930(11)

Symmetry transformations used to generate equivalent atoms:

(1) x,y-1,z (2) -y,x,z (3) -y+1,x,z (4) x,y,z-1 (5) x-1,y,z-1 (6) -x+1,-y+1,z (7) y,-x+1,z (8) x,-y+1,z (9) -x+1,y,z (10) -y+1,-x+1,z (11) y,x,z (12) x,y+1,z (13) x,y,z+1 (14) x+1,y,z+1 (15) -y+1,x,z+1 (16) -y+1,x+1,z+1

4. Structure: $(MA)_{0.56}(en)_{0.44}(Pb)_{0.692}(I)_{2.824}$

Table S17. Atomic coordinates (x10^4) and equivalent isotropic displacement parameters (Å^{2}x10^3) for $(MA)_{0.56}(en)_{0.44}(Pb)_{0.692}(I)_{2.824}$ at 293 K with estimated standard deviations in parentheses.

Label	x	y	z	Occupancy	U_{eq}*
Pb(1)	0	0	19(5)	0.815(4)	59(1)
I(1)	0	0	5125(18)	1	150(2)
I(2)	5000	0	90(20)	1	156(2)
C(1)	5000	5000	3954(2)	1	304(19)
N(1)	5000	5000	6162(1)	1	304(19)
H(1c1)	4742.66	3596.43	3448.7	0.125	364.9
H(2c1)	3913.14	5924.65	3448.7	0.125	364.9
H(3c1)	6344.2	5478.92	3448.7	0.125	364.9
H(1n1)	4844.22	6283.77	6618.89	0.125	364.9
H(2n1)	3966.11	4223.2	6618.89	0.125	364.9
H(3n1)	6189.67	4493.02	6618.89	0.125	364.9

*U_{eq} is defined as one third of the trace of the orthogonalized U_{ij} tensor.

Table S18. Anisotropic displacement parameters (Å^{2}x10^3) for $(MA)_{0.56}(en)_{0.44}(Pb)_{0.692}(I)_{2.824}$ at 293 K with estimated standard deviations in parentheses.

Label	U_{11}	U_{22}	U_{33}	U_{12}	U_{13}	U_{23}
Pb(1)	60(1)	60(1)	56(2)	0	0	0
I(1)	203(2)	203(2)	45(3)	0	0	0
I(2)	48(2)	216(3)	204(3)	0	0	0

The anisotropic displacement factor exponent takes the form: $-2\pi^2[h^2a^{*2}U_{11} + \ldots + 2hka^*b^*U_{12}]$.

Table S19. Bond lengths [Å] for $(MA)_{0.56}(en)_{0.44}(Pb)_{0.692}(I)_{2.824}$ at 293 K with estimated standard deviations in parentheses.

Label	Distances
Pb(1)-I(1)#1	3.103(12)
Pb(1)-I(1)	3.237(12)
Pb(1)-I(2)#2	3.172(3)
Pb(1)-I(2)	3.172(3)
Pb(1)-I(2)#3	3.172(3)
Pb(1)-I(2)#4	3.172(3)
I(2)-N(1)#5	4.034(9)
I(2)-N(1)#1	4.034(9)
C(1)-N(1)	1.3999(18)

Symmetry transformations used to generate equivalent atoms:

(1) x,y,z-1 (2) x-1,y,z (3) -y,x-1,z (4) -y,x,z (5) x,y-1,z-1 (6) -x+1,-y+1,z (7) -y+1,x,z (8) y,-x+1,z (9) x,-y+1,z (10) -x+1,y,z (11) -y+1,-x+1,z (12) y,x,z (13) x+1,y,z (14) x,y,z+1 (15) x,y+1,z+1 (16) -y,x,z+1 (17) -y+1,x,z+1

Table S20. Bond angles [°] for $(MA)_{0.56}(en)_{0.44}(Pb)_{0.692}(I)_{2.824}$ at 293 K with estimated standard deviations in parentheses.

Label	Angles
I(1)#1-Pb(1)-I(1)	180.0(5)
I(1)#1-Pb(1)-I(2)#2	90.8(2)
I(1)#1-Pb(1)-I(2)	90.8(2)
I(1)#1-Pb(1)-I(2)#3	90.8(2)
I(1)#1-Pb(1)-I(2)#4	90.8(2)
I(1)-Pb(1)-I(2)#2	89.2(2)
I(1)-Pb(1)-I(2)	89.2(2)
I(1)-Pb(1)-I(2)#3	89.2(2)
I(1)-Pb(1)-I(2)#4	89.2(2)
I(2)#2-Pb(1)-I(2)	178.3(4)
I(2)#2-Pb(1)-I(2)#3	89.987(5)
I(2)#2-Pb(1)-I(2)#4	89.987(5)
I(2)-Pb(1)-I(2)#3	89.987(5)
I(2)-Pb(1)-I(2)#4	89.987(5)
I(2)#3-Pb(1)-I(2)#4	178.3(4)
Pb(1)-I(1)-Pb(1)#14	180.0(5)
Pb(1)-I(2)-Pb(1)#13	178.3(5)

Symmetry transformations used to generate equivalent atoms:

(1) x,y,z-1 (2) x-1,y,z (3) -y,x-1,z (4) -y,x,z (5) x,y-1,z-1 (6) -x+1,-y+1,z (7) -y+1,x,z (8) y,-x+1,z (9) x,-y+1,z (10) -x+1,y,z (11) -y+1,-x+1,z (12) y,x,z (13) x+1,y,z (14) x,y,z+1 (15) x,y+1,z+1 (16) -y,x,z+1 (17) -y+1,x,z+1

5. Structure: *en*I$_2$

Table S21. Atomic coordinates (x10^4) and equivalent isotropic displacement parameters (Å^{2}x10^3) for *en*I$_2$ at 293 K with estimated standard deviations in parentheses.

Label	x	y	z	Occupancy	U$_{eq}$*
I(1)	8501(1)	0	219(2)	1	39(1)
N(1)	3784(7)	0	220(20)	1	40(3)
C(2)	4719(8)	0	1090(20)	1	47(4)
H(1n1)	3672.83	-1156.2	-1024.56	0.25	47.8
H(2n1)	3498.65	-398.18	1550.47	0.5	47.8
H(3n1)	3628.21	1554.38	-364.93	0.5	47.8
H(1c2)	4858.75	-1489.74	2217.15	0.5	57
H(2c2)	4858.75	1489.74	2217.15	0.5	57

*U$_{eq}$ is defined as one third of the trace of the orthogonalized U$_{ij}$ tensor.

Table S22. Anisotropic displacement parameters (Å^{2}x10^3) for *en*I$_2$ at 293 K with estimated standard deviations in parentheses.

Label	U$_{11}$	U$_{22}$	U$_{33}$	U$_{12}$	U$_{13}$	U$_{23}$
I(1)	36(1)	38(1)	41(1)	0	3(1)	0
N(1)	36(5)	38(5)	45(5)	0	2(4)	0
C(2)	26(6)	81(10)	36(6)	0	8(5)	0

The anisotropic displacement factor exponent takes the form: $-2\pi^2[h^2a^{*2}U_{11} + ... + 2hka^*b^*U_{12}]$.

Table S23. Bond lengths [Å] for *en*I$_2$ at 293 K with estimated standard deviations in parentheses.

Label	Distances
I(1)-N(1)#1	3.655(8)
I(1)-N(1)#2	3.594(8)
I(1)-N(1)#3	3.655(8)
I(1)-N(1)#4	3.594(8)
I(1)-N(1)#5	3.534(11)
N(1)-C(2)	1.474(16)
N(1)-H(1n1)	0.87
N(1)-H(1n1)#6	0.87
N(1)-H(2n1)	0.87
N(1)-H(2n1)#6	0.87
N(1)-H(3n1)	0.87
N(1)-H(3n1)#6	0.87
C(2)-C(2)#5	1.487(18)
C(2)-H(1c2)	0.96
C(2)-H(1c2)#6	0.96
H(1n1)-H(3n1)#6	0.4045
H(2n1)-H(2n1)#6	0.4045

Symmetry transformations used to generate equivalent atoms:

(1) x+1/2,y-1/2,z-1/2 (2) x+1/2,y-1/2,z+1/2 (3) x+1/2,y+1/2,z-1/2 (4) x+1/2,y+1/2,z+1/2 (5) -x+1,y,-z (6) x,-y,z (7) x-1/2,y-1/2,z-1/2 (8) x-1/2,y-1/2,z+1/2 (9) x-1/2,y+1/2,z-1/2 (10) x-1/2,y+1/2,z+1/2

Table S24. Bond angles [°] for *en*I$_2$ at 293 K with estimated standard deviations in parentheses.

Label	Angles
N(1)#1-I(1)-N(1)#2	89.35(17)
N(1)#1-I(1)-N(1)#3	88.04(17)
N(1)#1-I(1)-N(1)#4	166.1(2)
N(1)#1-I(1)-N(1)#5	98.6(2)
N(1)#2-I(1)-N(1)#3	166.1(2)
N(1)#2-I(1)-N(1)#4	89.93(17)
N(1)#2-I(1)-N(1)#5	95.3(2)
N(1)#3-I(1)-N(1)#4	89.35(17)
N(1)#3-I(1)-N(1)#5	98.6(2)
N(1)#4-I(1)-N(1)#5	95.3(2)
I(1)#7-N(1)-I(1)#8	89.35(4)
I(1)#7-N(1)-I(1)#9	89.9(2)
I(1)#7-N(1)-I(1)#10	166.1(3)
I(1)#7-N(1)-I(1)#5	84.69(19)
I(1)#7-N(1)-C(2)	104.9(5)

Symmetry transformations used to generate equivalent atoms:

(1) x+1/2,y-1/2,z-1/2 (2) x+1/2,y-1/2,z+1/2 (3) x+1/2,y+1/2,z-1/2 (4) x+1/2,y+1/2,z+1/2 (5) -x+1,y,-z (6) x,-y,z (7) x-1/2,y-1/2,z-1/2 (8) x-1/2,y-1/2,z+1/2 (9) x-1/2,y+1/2,z-1/2 (10) x-1/2,y+1/2,z+1/2

6. Structure: *en*PbI$_4$

Table S25. Atomic coordinates (x10^4) and equivalent isotropic displacement parameters (Å^{2}x10^3) for *en*PbI$_4$ at 293 K with estimated standard deviations in parentheses.

Label	x	y	z	Occupancy	U$_{eq}$*
Pb	5000	0	5000	1	34(1)
I(1)	3604(2)	0	1799(2)	1	41(1)
I(2)	1120(2)	0	4324(2)	1	41(1)
N	1251(2)	0	750(40)	1	121(10)
C	341(8)	0	743(6)	1	121(10)
O	1977(13)	5000	2300(20)	1	58(5)
H(1n)	1567.66	-1644.18	1225.06	0.5	145.4
H(2n)	1202.86	0	-204.8	1	145.4
H(3n)	1565.51	1653.92	1216.64	0.5	145.4
H(1c)	268.19	-1649.08	1217.63	0.5	145.4
H(2c)	268.19	1649.08	1217.63	0.5	145.4
H(1o)	2185.69	6438.38	2743.02	0.5	69.2

*U$_{eq}$ is defined as one third of the trace of the orthogonalized U$_{ij}$ tensor.

Table S26. Anisotropic displacement parameters (Å^{2}x10^3) for *en*PbI$_4$ at 293 K with estimated standard deviations in parentheses.

Label	U$_{11}$	U$_{22}$	U$_{33}$	U$_{12}$	U$_{13}$	U$_{23}$
Pb	36(1)	37(1)	26(1)	0	10(1)	0
I(1)	36(1)	55(1)	29(1)	0	9(1)	0
I(2)	45(1)	41(1)	40(1)	0	22(1)	0

The anisotropic displacement factor exponent takes the form: $-2\pi^2[h^2a^{*2}U_{11} + ... + 2hka^*b^*U_{12}]$.

Table S27. Bond lengths [Å] for *en*PbI$_4$ at 293 K with estimated standard deviations in parentheses.

Label	Distances
Pb-I(1)	3.193(2)
Pb-I(1)#1	3.193(2)
Pb-I(2)#2	3.2581(17)
Pb-I(2)#3	3.2581(17)
Pb-I(2)#4	3.2581(17)
Pb-I(2)#5	3.2581(17)
I(1)-N	3.580(6)
I(1)-N#6	3.64(3)
I(1)-N#7	3.64(3)
I(2)-N	3.81(4)
N-C	1.50(2)
N-H(1n)	0.958(12)
N-H(1n)#8	0.958(12)
N-H(2n)	0.97(4)
N-H(3n)	0.959(12)
N-H(3n)#8	0.959(12)
C-C#9	1.500(9)
C-H(1c)	0.960(6)
C-H(1c)#8	0.960(6)
O-H(1o)	0.819(9)
O-H(1o)#10	0.819(9)
H(1n)-H(3n)#8	0.0093

Symmetry transformations used to generate equivalent atoms:

(1) -x+1,y,-z+1 (2) x+1/2,y-1/2,z (3) x+1/2,y+1/2,z (4) -x+1/2,y-1/2,-z+1 (5) -x+1/2,y+1/2,-z+1 (6) -x+1/2,y-1/2,-z (7) -x+1/2,y+1/2,-z (8) x,-y,z (9) -x,y,-z (10) x,-y+1,z (11) x-1/2,y-1/2,z (12) x-1/2,y+1/2,z

Table S28. Bond angles [°] for *en*PbI$_4$ at 293 K with estimated standard deviations in parentheses.

Label	Angles
I(1)-Pb-I(1)#1	180.0(5)
I(1)-Pb-I(2)#2	90.35(4)
I(1)-Pb-I(2)#3	90.35(4)
I(1)-Pb-I(2)#4	89.65(4)
I(1)-Pb-I(2)#5	89.65(4)
I(1)#1-Pb-I(2)#2	89.65(4)
I(1)#1-Pb-I(2)#3	89.65(4)
I(1)#1-Pb-I(2)#4	90.35(4)
I(1)#1-Pb-I(2)#5	90.35(4)
I(2)#2-Pb-I(2)#3	93.68(4)
I(2)#2-Pb-I(2)#4	86.32(4)
I(2)#2-Pb-I(2)#5	180.0(5)
I(2)#3-Pb-I(2)#4	180.0(5)

Symmetry transformations used to generate equivalent atoms:

(1) -x+1,y,-z+1 (2) x+1/2,y-1/2,z (3) x+1/2,y+1/2,z (4) -x+1/2,y-1/2,-z+1 (5) -x+1/2,y+1/2,-z+1 (6) -x+1/2,y-1/2,-z (7) -x+1/2,y+1/2,-z (8) x,-y,z (9) -x,y,-z (10) x,-y+1,z (11) x-1/2,y-1/2,z (12) x-1/2,y+1/2,z

Crystal density measurements

Table S29. Comparison of the initial, nominal ratio of *en* (the amount that was used in the synthesis) and the experimental determined one from ^{1}H-NMR spectroscopy (x), along with the determined crystal density for all $(MA)_{1-x}(en)_x(Sn)_{1-0.7x}(I)_{3-0.4x}$ materials and the theoritical crystal density if all the nomimal amount of *en* entered the structure. The experimental crystal density was determined using a commercial available pycnometer.

MASnI$_3$ + *en%*	Nominal *en* amount	NMR *en* (x)	Exp. crystal density (g cm^{-3}) Based on (x)	Theor. crystal density (g cm^{-3}) Based on nomimal amount
0			3.640(1)	3.636
10	0.1	0.05	3.591(1)	3.552
20	0.2	0.09	3.536(1)	3.469
50	0.5	0.21	3.505(2)	3.228
60	0.60	0.24	3.469(1)	3.146
80	0.80	0.36	3.301(1)	2.962
100	1	0.40	3.255(1)	2.816

Table S30. Comparison of the initial, nominal ratio of *en* (the amount that was used in the synthesis) and the experimental determined one from ^{1}H-NMR spectroscopy (x), along with the determined crystal density for all $(FA)_{1-x}(en)_x(Pb)_{1-0.7x}(I)_{3-0.4x}$ materials and the theoritical crystal density if all the nomimal amount of *en* entered the structure. The experimental crystal density was determined using a commercial available pycnometer.

FAPbI$_3$ + *en%*	Nominal *en* amount	NMR *en* (x)	Exp. crystal density (g cm^{-3}) Based on (x)	Theor. crystal density (g cm^{-3}) Based on nomimal amount
0			4.106(2)	4.101
10	0.1	0.07	4.024(1)	3.989
20	0.2	0.11	4.000(2)	3.876
50	0.5	0.21	3.880(1)	3.547
70	0.7	0.27	3.642(2)	3.337
100	1	0.39	3.620(1)	3.010

Table S31. Comparison of the initial, nominal ratio of *en* (the amount that was used in the synthesis) and the experimental determined one from ^{1}H-NMR spectroscopy (x), along with the determined crystal density for all $(MA)_{1-x}(en)_x(Pb)_{1-0.7x}(I)_{3-0.4x}$ materials and the theoritical crystal density if all the nomimal amount of *en* entered the structure. The experimental crystal density was determined using a commercial available pycnometer.

MAPbI$_3$ + *en*%	Nominal *en* amount	NMR *en* (x)	Exp. crystal density (g cm^{-3}) Based on (x)	Theor. crystal density (g cm^{-3}) Based on nomimal amount
0			4.151(2)	4.146
10	0.1	0.03	4.121(3)	4.025
20	0.2	0.1	4.058(2)	3.935
50	0.50	0.29	3.710(1)	3.586
60	0.6	0.35	3.640(1)	3.445
70	0.7	0.40	3.624(1)	3.324
100	1	0.44	3.550(1)	2.988
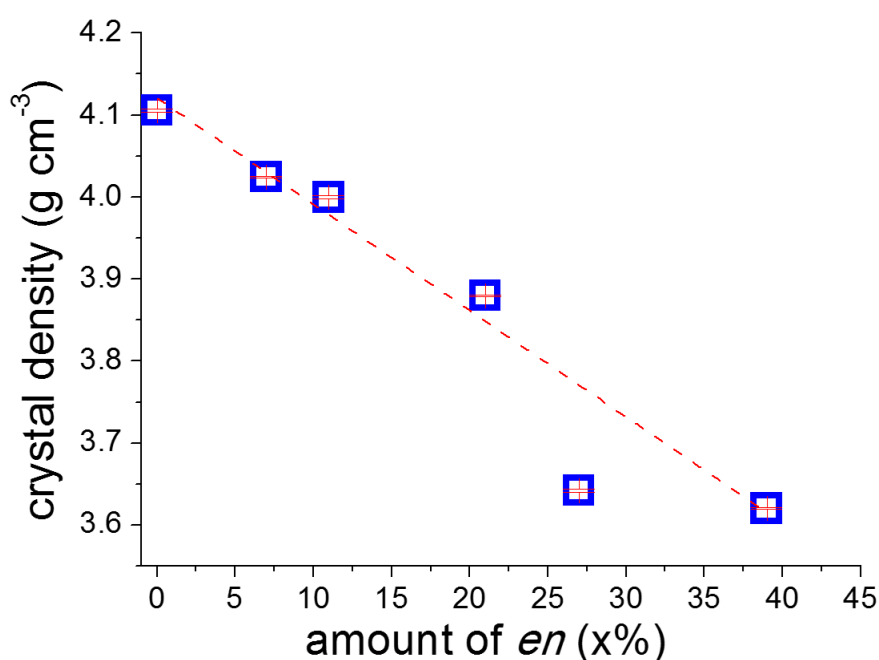
Figure S36. Correlation of the percentage of *en* in $(FA)_{1-x}(en)_x(Pb)_{1-0.7x}(I)_{3-0.4x}$ samples towards the determined crystal density (error bars are inside the blue squares). There is a 12% decrease in the crystal density of the 39% containing *en* material in comparison to the pristine one.

Determination of chemical formulae

Table S32. Case 1, formula: $A_{(1-x)}en_{(x/2)}M_{(1-x/2)}I_{(3-x)}$. Correlation between the calculated crystal density based on the proposed formula and the experimentally determined one using a pycnometer. The amount of *en* (x) is determined by ^{1}H-NMR spectroscopy. Density difference above the threshold value of 0.1 g cm^{-3} is marked with red color.

Amount of *en* (x)	en^{2+}	MA$^+$	Sn^{2+}	I$^-$	MA(1-x) *en*(x/2)Sn(1-x/2)I(3-x) MW	Cell volume V(Å^3)	Calculated density (g cm^{-3})	Exp. Density (g cm^{-3})	Density difference
0	63.1	32	118.7	126.9	531.4	242.7	3.636	3.64	0.004
0.05	63.1	32	118.7	126.9	522.1	243.4	3.562	3.591	0.029
0.09	63.1	32	118.7	126.9	514.6	244.1	3.501	3.536	0.035
0.21	63.1	32	118.7	126.9	492.2	245.8	3.325	3.505	0.179
0.24	63.1	32	118.7	126.9	486.6	246.5	3.278	3.469	0.191
0.36	63.1	32	118.7	126.9	464.2	249.8	3.086	3.301	0.215
0.4	63.1	32	118.7	126.9	456.7	250.1	3.032	3.255	0.226

Amount of *en* (x)	en^{2+}	MA$^+$	Pb^{2+}	I$^-$	MA(1-x) *en*(x/2)Pb(1-x/2)I(3-x) MW	Cell volume V(Å^3)	Calculated density (g cm^{-3})	Exp. Density (g cm^{-3})	Density difference
0	63.1	32	207.2	126.9	619.9	248.3	4.146	4.151	0.005
0.03	63.1	32	207.2	126.9	613.0	249.5	4.08	4.121	0.041
0.1	63.1	32	207.2	126.9	596.8	248.8	3.983	4.058	0.075
0.29	63.1	32	207.2	126.9	552.9	252	3.643	3.71	0.066
0.35	63.1	32	207.2	126.9	539.1	255	3.51	3.64	0.129
0.4	63.1	32	207.2	126.9	527.5	256.7	3.412	3.624	0.211
0.44	63.1	32	207.2	126.9	518.3	260.3	3.306	3.55	0.244

Amount of *en* (x)	en^{2+}	FA$^+$	Pb^{2+}	I$^-$	FA(1-x) *en*(x/2)Pb(1-x/2)I(3-x) MW	Cell volume V(Å^3)	Calculated density (g cm^{-3})	Exp. Density (g cm^{-3})	Density difference
0	63.1	45.07	207.2	126.9	633.0	256.3	4.101	4.106	0.005
0.07	63.1	45.07	207.2	126.9	615.9	256.9	3.981	4.024	0.043
0.11	63.1	45.07	207.2	126.9	606.1	257.6	3.907	4	0.093
0.21	63.1	45.07	207.2	126.9	581.7	259.3	3.725	3.88	0.154
0.27	63.1	45.07	207.2	126.9	567.1	259.9	3.623	3.642	0.019
0.39	63.1	45.07	207.2	126.9	537.8	261.97	3.409	3.62	0.211

Table S33. Case 2, formula: $A_{(1-x)}en_{(x/2)}M_{(1-x/2)}I_{(3-x)}$, (charge of *en*:+1). Correlation between the calculated crystal density based on the proposed formula and the experimentally determined one using a pycnometer. The amount of *en* (x) is determined by ^{1}H-NMR spectroscopy. Density difference above 0.1 g cm^{-3} is marked with red color.

Amount of *en* (x)	en^{2+}	MA$^+$	Sn^{2+}	I$^-$	MA(1-x)*en*(x)Sn(1-x/2)I(3-x) MW	Cell volume V(Å^3)	Calculated density (g cm^{-3})	Exp. Density (g cm^{-3})	Density difference
0	63.1	32	118.7	126.9	531.4	242.7	3.636	3.64	0.004
0.05	63.1	32	118.7	126.9	523.6	243.4	3.572	3.591	0.018
0.09	63.1	32	118.7	126.9	517.4	244.1	3.520	3.536	0.016
0.21	63.1	32	118.7	126.9	498.8	245.8	3.370	3.505	0.135
0.24	63.1	32	118.7	126.9	494.2	246.5	3.329	3.469	0.140
0.36	63.1	32	118.7	126.9	475.5	249.8	3.161	3.301	0.140
0.4	63.1	32	118.7	126.9	469.3	250.1	3.116	3.255	0.139

Amount of *en* (x)	en^{2+}	MA$^+$	Pb^{2+}	I$^-$	MA(1-x) *en*(x)Pb(1-x/2)I(3-x) MW	Cell volume V(Å^3)	Calculated density (g cm^{-3})	Exp. Density (g cm^{-3})	Density difference
0	63.1	32	207.2	126.9	619.9	248.3	4.146	4.151	0.005
0.03	63.1	32	207.2	126.9	613.9	249.5	4.086	4.121	0.035
0.1	63.1	32	207.2	126.9	600.0	248.8	4.004	4.058	0.054
0.29	63.1	32	207.2	126.9	562.1	252	3.704	3.71	0.006
0.35	63.1	32	207.2	126.9	550.1	255	3.582	3.64	0.058
0.4	63.1	32	207.2	126.9	540.1	256.7	3.494	3.624	0.130
0.44	63.1	32	207.2	126.9	532.2	260.3	3.395	3.55	0.155

Amount of *en* (x)	en^{2+}	FA$^+$	Pb^{2+}	I$^-$	FA(1-x) *en*(x)Pb(1-x/2)I(3-x) MW	Cell volume V(Å^3)	Calculated density (g cm^{-3})	Exp. Density (g cm^{-3})	Density difference
0	63.1	45.07	207.2	126.9	633.0	256.3	4.101	4.106	0.005
0.07	63.1	45.07	207.2	126.9	618.1	256.9	3.995	4.024	0.029
0.11	63.1	45.07	207.2	126.9	609.6	257.6	3.930	4	0.070
0.21	63.1	45.07	207.2	126.9	588.3	259.3	3.768	3.88	0.112
0.27	63.1	45.07	207.2	126.9	575.6	259.9	3.678	3.642	-0.036
0.39	63.1	45.07	207.2	126.9	550.1	261.97	3.487	3.62	0.133

Table S34. Case 3, formula: $Aen_{(x/2)}M_{(1-x)}I_{(3-x)}$. Correlation between the calculated crystal density based on the proposed formula and the experimentally determined one using a pycnometer. The amount of *en* (x) is determined by ^1H-NMR spectroscopy. Density difference above 0.1 g cm^{-3} is marked with red color.

Amount of *en* (x)	en^{2+}	MA$^+$	Sn^{2+}	I$^-$	MA *en*(x/2)Sn(1-x)I(3-x) MW	Cell volume V(Å^3)	Calculated density (g cm^{-3})	Exp. Density (g cm^{-3})	Density difference
0	63.1	32	118.7	126.9	531.4	242.7	3.636	3.64	0.004
0.05	63.1	32	118.7	126.9	520.7	243.4	3.552	3.591	0.038
0.09	63.1	32	118.7	126.9	512.1	244.1	3.484	3.536	0.052
0.21	63.1	32	118.7	126.9	486.4	245.8	3.286	3.505	0.219
0.24	63.1	32	118.7	126.9	480.0	246.5	3.234	3.469	0.235
0.36	63.1	32	118.7	126.9	454.3	249.8	3.020	3.301	0.281
0.4	63.1	32	118.7	126.9	445.8	250.1	2.960	3.255	0.295

Amount of *en* (x)	en^{2+}	MA$^+$	Pb^{2+}	I$^-$	MA *en*(x/2)Pb(1-x)I(3-x) MW	Cell volume V(Å^3)	Calculated density (g cm^{-3})	Exp. Density (g cm^{-3})	Density difference
0	63.1	32	207.2	126.9	619.9	248.3	4.146	4.151	0.005
0.03	63.1	32	207.2	126.9	610.8	249.5	4.065	4.121	0.055
0.1	63.1	32	207.2	126.9	589.6	248.8	3.935	4.058	0.122
0.29	63.1	32	207.2	126.9	532.2	252	3.507	3.71	0.203
0.35	63.1	32	207.2	126.9	514.0	255	3.347	3.64	0.293
0.4	63.1	32	207.2	126.9	498.9	256.7	3.227	3.624	0.397
0.44	63.1	32	207.2	126.9	486.8	260.3	3.105	3.55	0.445

Amount of *en* (x)	en^{2+}	FA$^+$	Pb^{2+}	I$^-$	FA *en*(x/2)Pb(1-x)I(3-x) MW	Cell volume V(Å^3)	Calculated density (g cm^{-3})	Exp. Density (g cm^{-3})	Density difference
0	63.1	45.07	207.2	126.9	633.0	256.3	4.101	4.106	0.005
0.07	63.1	45.07	207.2	126.9	611.8	256.9	3.954	4.024	0.069
0.11	63.1	45.07	207.2	126.9	599.7	257.6	3.866	4	0.134
0.21	63.1	45.07	207.2	126.9	569.4	259.3	3.647	3.88	0.233
0.27	63.1	45.07	207.2	126.9	551.3	259.9	3.522	3.642	0.120
0.39	63.1	45.07	207.2	126.9	515.0	261.97	3.264	3.62	0.356

Table S35. Case 4, formula: A$en_{(x)}$M$_{(1-x/2)}$I$_{(3-x/2)}$. Correlation between the calculated crystal density based on the proposed formula and the experimentally determined one using a pycnometer. The amount of *en* (x) is determined by ^{1}H-NMR spectroscopy. Density difference above 0.1 g cm^{-3} is marked with red color.

Amount of *en* (x)	en^{2+}	MA^+	Sn^{2+}	I^-	MA en(x)Sn(1-x/2)I(3-x/2) MW	Cell volume V(Å³)	Calculated density (g cm^{-3})	Exp. Density (g cm^{-3})	Density difference
0	63.1	32	118.7	126.9	531.4	242.7	3.636	3.64	0.004
0.05	63.1	32	118.7	126.9	526.8	243.4	3.594	3.591	-0.003
0.09	63.1	32	118.7	126.9	523.2	244.1	3.559	3.536	-0.023
0.21	63.1	32	118.7	126.9	512.2	245.8	3.460	3.505	0.044
0.24	63.1	32	118.7	126.9	509.5	246.5	3.432	3.469	0.0367
0.36	63.1	32	118.7	126.9	498.6	249.8	3.314	3.301	-0.013
0.4	63.1	32	118.7	126.9	495.0	250.1	3.286	3.255	-0.031

Amount of *en* (x)	en^{2+}	MA^+	Pb^{2+}	I^-	MA en(x)Pb(1-x/2)I(3-x/2) MW	Cell volume V(Å³)	Calculated density (g cm^{-3})	Exp. Density (g cm^{-3})	Density difference
0	63.1	32	207.2	126.9	619.9	248.3	4.146	4.151	0.005
0.03	63.1	32	207.2	126.9	615.8	249.5	4.099	4.121	0.022
0.1	63.1	32	207.2	126.9	606.4	248.8	4.047	4.058	0.011
0.29	63.1	32	207.2	126.9	580.6	252	3.826	3.71	-0.116
0.35	63.1	32	207.2	126.9	572.5	255	3.728	3.64	-0.088
0.4	63.1	32	207.2	126.9	565.7	256.7	3.659	3.624	-0.035
0.44	63.1	32	207.2	126.9	560.3	260.3	3.574	3.55	-0.024

Amount of *en* (x)	en^{2+}	FA^+	Pb^{2+}	I^-	FA en(x)Pb(1-x/2)I(3-x/2) MW	Cell volume V(Å³)	Calculated density (g cm^{-3})	Exp. Density (g cm^{-3})	Density difference
0	63.1	45.07	207.2	126.9	633.0	256.3	4.101	4.106	0.005
0.07	63.1	45.07	207.2	126.9	623.5	256.9	4.030	4.024	-0.006
0.11	63.1	45.07	207.2	126.9	618.1	257.6	3.984	4	0.016
0.21	63.1	45.07	207.2	126.9	604.5	259.3	3.871	3.88	0.009
0.27	63.1	45.07	207.2	126.9	596.4	259.9	3.810	3.642	-0.168
0.39	63.1	45.07	207.2	126.9	580.1	261.97	3.677	3.62	-0.057

Table S36. Case 5, formula: $A_{(1-x/2)}en_{(x)}M_{(1-x)}I_{(3-x/2)}$. Correlation between the calculated crystal density based on the proposed formula and the experimentally determined one using a pycnometer. The amount of *en* (x) is determined by ^{1}H-NMR spectroscopy. Density difference above 0.1 g cm^{-3} is marked with red color.

Amount of *en* (x)	en²⁺	MA⁺	Sn²⁺	I⁻	MA(1-x/2) *en*(x)Sn(1-x)I(3-x/2) MW	Cell volume V(Å³)	Calculated density (g cm⁻³)	Exp. Density (g cm⁻³)	Density difference
0	63.1	32	118.7	126.9	531.4	242.7	3.636	3.64	0.004
0.05	63.1	32	118.7	126.9	524.6	243.4	3.579	3.591	0.012
0.09	63.1	32	118.7	126.9	519.2	244.1	3.532	3.536	0.004
0.21	63.1	32	118.7	126.9	503.0	245.8	3.398	3.505	0.107
0.24	63.1	32	118.7	126.9	499.0	246.5	3.361	3.469	0.108
0.36	63.1	32	118.7	126.9	482.8	249.8	3.209	3.301	0.092
0.4	63.1	32	118.7	126.9	477.4	250.1	3.170	3.255	0.085

Amount of *en* (x)	en²⁺	MA⁺	Pb²⁺	I⁻	MA(1-x/2) *en*(x)Pb(1-x)I(3-x/2) MW	Cell volume V(Å³)	Calculated density (g cm⁻³)	Exp. Density (g cm⁻³)	Density difference
0	63.1	32	207.2	126.9	619.9	248.3	4.146	4.151	0.005
0.03	63.1	32	207.2	126.9	613.2	249.5	4.081	4.121	0.040
0.1	63.1	32	207.2	126.9	597.5	248.8	3.988	4.058	0.070
0.29	63.1	32	207.2	126.9	555.1	252	3.658	3.71	0.052
0.35	63.1	32	207.2	126.9	541.6	255	3.527	3.64	0.113
0.4	63.1	32	207.2	126.9	530.5	256.7	3.432	3.624	0.192
0.44	63.1	32	207.2	126.9	521.5	260.3	3.327	3.55	0.223

Amount of *en* (x)	en²⁺	FA⁺	Pb²⁺	I⁻	FA(1-x/2) *en*(x)Pb(1-x)I(3-x/2) MW	Cell volume V(Å³)	Calculated density (g cm⁻³)	Exp. Density (g cm⁻³)	Density difference
0	63.1	45.07	207.2	126.9	633.0	256.3	4.101	4.106	0.005
0.07	63.1	45.07	207.2	126.9	616.9	256.9	3.987	4.024	0.037
0.11	63.1	45.07	207.2	126.9	607.7	257.6	3.917	4	0.083
0.21	63.1	45.07	207.2	126.9	584.7	259.3	3.744	3.88	0.136
0.27	63.1	45.07	207.2	126.9	570.8	259.9	3.647	3.642	-0.005
0.39	63.1	45.07	207.2	126.9	543.2	261.97	3.443	3.62	0.177

Table S37. Case 6, formula: $A_{(1-x)}en_{(x/2)}[M_{(1-y/2)}I_{(3-y)}]$, y = 0.05. Correlation between the calculated crystal density based on the proposed formula and the experimentally determined one using a pycnometer. The amount of *en* (x) is determined by ^{1}H-NMR spectroscopy. Density difference above 0.1 g cm^{-3} is marked with red color.

Amount of *en* (x)	en^{2+}	MA$^+$	Sn^{2+}	I$^-$	MA$_{(1-x)}$en$_{(x/2)}$[Sn$_{0.975}$I$_{2.95}$] MW	Cell volume V(Å^3)	Calculated density (g cm^{-3})	Exp. Density (g cm^{-3})	Density difference
0	63.1	32	118.7	126.9	531.4	242.7	3.636	3.64	0.004
0.05	63.1	32	118.7	126.9	522.1	243.4	3.562	3.591	0.029
0.09	63.1	32	118.7	126.9	522.0	244.1	3.551	3.536	-0.015
0.21	63.1	32	118.7	126.9	522.0	245.8	3.526	3.505	-0.021
0.24	63.1	32	118.7	126.9	522.0	246.5	3.516	3.469	-0.047
0.36	63.1	32	118.7	126.9	521.9	249.8	3.469	3.301	-0.168
0.4	63.1	32	118.7	126.9	521.9	250.1	3.465	3.255	-0.210

Amount of *en* (x)	en^{2+}	MA$^+$	Pb^{2+}	I$^-$	MA$_{(1-x)}$en$_{(x/2)}$[Pb$_{0.975}$I$_{2.95}$] MW	Cell volume V(Å^3)	Calculated density (g cm^{-3})	Exp. Density (g cm^{-3})	Density difference
0	63.1	32	207.2	126.9	619.9	248.3	4.146	4.151	0.005
0.03	63.1	32	207.2	126.9	608.4	249.5	4.049	4.121	0.072
0.1	63.1	32	207.2	126.9	608.3	248.8	4.060	4.058	-0.002
0.29	63.1	32	207.2	126.9	608.2	252	4.008	3.71	-0.298
0.35	63.1	32	207.2	126.9	608.2	255	3.961	3.64	-0.321
0.4	63.1	32	207.2	126.9	608.2	256.7	3.934	3.624	-0.310
0.44	63.1	32	207.2	126.9	608.2	260.3	3.880	3.55	-0.330

Amount of *en* (x)	en^{2+}	FA$^+$	Pb^{2+}	I$^-$	FA$_{(1-x)}$en$_{(x/2)}$[Pb$_{0.975}$I$_{2.95}$] MW	Cell volume V(Å^3)	Calculated density (g cm^{-3})	Exp. Density (g cm^{-3})	Density difference
0	63.1	45.07	207.2	126.9	633.0	256.3	4.101	4.106	0.005
0.07	63.1	45.07	207.2	126.9	620.5	256.9	4.011	4.024	0.013
0.11	63.1	45.07	207.2	126.9	619.9	257.6	3.996	4	0.003
0.21	63.1	45.07	207.2	126.9	618.6	259.3	3.962	3.88	-0.082
0.27	63.1	45.07	207.2	126.9	617.8	259.9	3.947	3.642	-0.305
0.39	63.1	45.07	207.2	126.9	616.2	261.97	3.906	3.62	-0.286

Table S38. Case 7, formula: A$en_{(x)}$M$_{(1-x)}$I$_3$. Correlation between the calculated crystal density based on the proposed formula and the experimentally determined one using a pycnometer. The amount of *en* (x) is determined by ^{1}H-NMR spectroscopy. Density difference above 0.1 g cm^{-3} is marked with red color.

Amount of *en* (x)	en^{2+}	MA^+	Sn^{2+}	I^-	MA *en*(x)Sn(1-x)I3 MW	Cell volume V(Å^3)	Calculated density (g cm^{-3})	Exp. Density (g cm^{-3})	Density difference
0	63.1	32	118.7	126.9	531.4	242.7	3.636	3.64	0.004
0.05	63.1	32	118.7	126.9	528.6	243.4	3.606	3.591	-0.015
0.09	63.1	32	118.7	126.9	526.4	244.1	3.581	3.536	-0.045
0.21	63.1	32	118.7	126.9	519.7	245.8	3.511	3.505	-0.006
0.24	63.1	32	118.7	126.9	518.1	246.5	3.490	3.469	-0.021
0.36	63.1	32	118.7	126.9	511.4	249.8	3.399	3.301	-0.098
0.4	63.1	32	118.7	126.9	509.2	250.1	3.381	3.255	-0.126

Amount of *en* (x)	en^{2+}	MA^+	Pb^{2+}	I^-	MA *en*(x)Pb(1-x)I3 MW	Cell volume V(Å^3)	Calculated density (g cm^{-3})	Exp. Density (g cm^{-3})	Density difference
0	63.1	32	207.2	126.9	619.9	248.3	4.146	4.151	0.005
0.03	63.1	32	207.2	126.9	615.6	249.5	4.097	4.121	0.024
0.1	63.1	32	207.2	126.9	605.5	248.8	4.041	4.058	0.017
0.29	63.1	32	207.2	126.9	578.1	252	3.809	3.71	-0.099
0.35	63.1	32	207.2	126.9	569.5	255	3.708	3.64	-0.068
0.4	63.1	32	207.2	126.9	562.3	256.7	3.637	3.624	-0.013
0.44	63.1	32	207.2	126.9	556.5	260.3	3.550	3.55	-0.000

Amount of *en* (x)	en^{2+}	FA^+	Pb^{2+}	I^-	FA *en*(x)Pb(1-x)I3 MW	Cell volume V(Å^3)	Calculated density (g cm^{-3})	Exp. Density (g cm^{-3})	Density difference
0	63.1	45.07	207.2	126.9	633.0	256.3	4.101	4.106	0.005
0.07	63.1	45.07	207.2	126.9	622.9	256.9	4.026	4.024	-0.002
0.11	63.1	45.07	207.2	126.9	617.1	257.6	3.978	4	0.022
0.21	63.1	45.07	207.2	126.9	602.7	259.3	3.860	3.88	0.020
0.27	63.1	45.07	207.2	126.9	594.1	259.9	3.795	3.642	-0.154
0.39	63.1	45.07	207.2	126.9	576.8	262.0	3.656	3.62	-0.036

Table S39. Case 8, formula: $A_{(1-x/2)}en_{(x/2)}M_{(1-x/2)}I_{(3-x/2)}$. Correlation between the calculated crystal density based on the proposed formula and the experimentally determined one using a pycnometer. The amount of *en* (x) is determined by ^{1}H-NMR spectroscopy. Density difference above 0.1 g cm^{-3} is marked with red color.

Amount of *en* (x)	en^{2+}	MA$^+$	Sn^{2+}	I$^-$	MA(1-x/2) *en*(x/2)Sn(1-x/2)I(3-x/2) MW	Cell volume V(Å^3)	Calculated density (g cm^{-3})	Exp. Density (g cm^{-3})	Density difference
0	63.1	32	118.7	126.9	531.4	242.7	3.636	3.64	0.004
0.05	63.1	32	118.7	126.9	526.0	243.4	3.589	3.591	0.002
0.09	63.1	32	118.7	126.9	521.7	244.1	3.549	3.536	-0.013
0.21	63.1	32	118.7	126.9	508.9	245.8	3.438	3.505	0.067
0.24	63.1	32	118.7	126.9	505.7	246.5	3.406	3.469	0.062
0.36	63.1	32	118.7	126.9	492.8	249.8	3.276	3.301	0.025
0.4	63.1	32	118.7	126.9	488.5	250.1	3.243	3.255	0.012

Amount of *en* (x)	en^{2+}	MA$^+$	Pb^{2+}	I$^-$	MA(1-x/2) *en*(x/2)Pb(1-x/2)I(3-x/2) MW	Cell volume V(Å^3)	Calculated density (g cm^{-3})	Exp. Density (g cm^{-3})	Density difference
0	63.1	32	207.2	126.9	619.9	248.3	4.146	4.151	0.005
0.03	63.1	32	207.2	126.9	615.3	249.5	4.095	4.121	0.025
0.1	63.1	32	207.2	126.9	604.8	248.8	4.036	4.058	0.022
0.29	63.1	32	207.2	126.9	576.0	252	3.795	3.71	-0.085
0.35	63.1	32	207.2	126.9	566.9	255	3.691	3.64	-0.051
0.4	63.1	32	207.2	126.9	559.3	256.7	3.618	3.624	0.006
0.44	63.1	32	207.2	126.9	553.2	260.3	3.529	3.55	0.021

Amount of *en* (x)	en^{2+}	FA$^+$	Pb^{2+}	I$^-$	FA(1-x/2) *en*(x/2)Pb(1-x/2)I(3-x/2) MW	Cell volume V(Å^3)	Calculated density (g cm^{-3})	Exp. Density (g cm^{-3})	Density difference
0	63.1	45.07	207.2	126.9	633.0	256.3	4.101	4.106	0.005
0.07	63.1	45.07	207.2	126.9	621.9	256.9	4.020	4.024	0.004
0.11	63.1	45.07	207.2	126.9	615.6	257.6	3.968	4	0.032
0.21	63.1	45.07	207.2	126.9	599.8	259.3	3.841	3.88	0.039
0.27	63.1	45.07	207.2	126.9	590.3	259.9	3.772	3.642	-0.130
0.39	63.1	45.07	207.2	126.9	571.3	262.0	3.621	3.62	-0.001

Table S40. Case 9, formula: $A_{(1-x)}en_{(x)}M_{(1-x/2)}I_{(3)}$. Correlation between the calculated crystal density based on the proposed formula and the experimentally determined one using a pycnometer. The amount of *en* (x) is determined by ^{1}H-NMR spectroscopy. Density difference above 0.1 g cm^{-3} is marked with red color.

Amount of *en* (x)	en^{2+}	MA$^+$	Sn^{2+}	I$^-$	MA(1-x)*en*(x)Sn(1-x/2)I(3) MW	Cell volume V(Å^3)	Calculated density (g cm^{-3})	Exp. Density (g cm^{-3})	Density difference
0	63.1	32	118.7	126.9	531.4	242.7	3.636	3.64	0.004
0.05	63.1	32	118.7	126.9	529.9	243.4	3.616	3.591	-0.025
0.09	63.1	32	118.7	126.9	528.8	244.1	3.598	3.536	-0.062
0.21	63.1	32	118.7	126.9	525.5	245.8	3.549	3.505	-0.044
0.24	63.1	32	118.7	126.9	524.6	246.5	3.534	3.469	-0.065
0.36	63.1	32	118.7	126.9	521.2	249.8	3.465	3.301	-0.164
0.4	63.1	32	118.7	126.9	520.1	250.1	3.453	3.255	-0.198

Amount of *en* (x)	en^{2+}	MA$^+$	Pb^{2+}	I$^-$	MA(1-x)*en*(x)Pb(1-x/2)I(3) MW	Cell volume V(Å^3)	Calculated density (g cm^{-3})	Exp. Density (g cm^{-3})	Density difference
0	63.1	32	207.2	126.9	619.9	248.3	4.146	4.151	0.005
0.03	63.1	32	207.2	126.9	617.7	249.5	4.111	4.121	0.010
0.1	63.1	32	207.2	126.9	612.6	248.8	4.089	4.058	-0.031
0.29	63.1	32	207.2	126.9	598.9	252	3.946	3.71	-0.236
0.35	63.1	32	207.2	126.9	594.5	255	3.871	3.64	-0.231
0.4	63.1	32	207.2	126.9	590.9	256.7	3.822	3.624	-0.198
0.44	63.1	32	207.2	126.9	588	260.3	3.751	3.55	-0.201

Amount of *en* (x)	en^{2+}	FA$^+$	Pb^{2+}	I$^-$	FA(1-x)*en*(x)Pb(1-x/2)I(3) MW	Cell volume V(Å^3)	Calculated density (g cm^{-3})	Exp. Density (g cm^{-3})	Density difference
0	63.1	45.07	207.2	126.9	633	256.3	4.101	4.106	0.005
0.07	63.1	45.07	207.2	126.9	627.0	256.9	4.053	4.024	-0.029
0.11	63.1	45.07	207.2	126.9	623.5	257.6	4.020	4	-0.020
0.21	63.1	45.07	207.2	126.9	615.0	259.3	3.938	3.88	-0.058
0.27	63.1	45.07	207.2	126.9	609.9	259.9	3.897	3.642	-0.255
0.39	63.1	45.07	207.2	126.9	599.6	262.0	3.801	3.62	-0.181

Table S41. Case 10, formula: $A_{(1-x)}en_{(x)}M_{(1-0.7x)}I_{(3-0.4x)}$. Correlation between the calculated crystal density based on the proposed formula and the experimentally determined one using a pycnometer. The amount of *en* (x) is determined by ^{1}H-NMR spectroscopy. Density difference above 0.1 g cm^{-3} is marked with red color.

Amount of *en* (x)	en^{2+}	MA$^+$	Sn^{2+}	I$^-$	MA(1-x)*en*(x)Sn(1-0.7x)I(3-0.4x) MW	Cell volume V(Å^3)	Calculated density (g cm^{-3})	Exp. Density (g cm^{-3})	Density difference
0	63.1	32	118.7	126.9	531.4	242.7	3.636	3.64	0.004
0.05	63.1	32	118.7	126.9	526.3	243.4	3.590	3.591	0.001
0.09	63.1	32	118.7	126.9	522.1	244.1	3.552	3.536	-0.016
0.21	63.1	32	118.7	126.9	509.8	245.8	3.444	3.505	0.061
0.24	63.1	32	118.7	126.9	506.7	246.5	3.414	3.469	0.055
0.36	63.1	32	118.7	126.9	494.4	249.8	3.287	3.301	0.014
0.4	63.1	32	118.7	126.9	490.3	250.1	3.255	3.255	-0.000

Amount of *en* (x)	en^{2+}	MA$^+$	Pb^{2+}	I$^-$	MA(1-x)*en*(x)Pb(1-0.7x)I(3-0.4x) MW	Cell volume V(Å^3)	Calculated density (g cm^{-3})	Exp. Density (g cm^{-3})	Density difference
0	63.1	32	207.2	126.9	619.9	248.3	4.146	4.151	0.005
0.03	63.1	32	207.2	126.9	614.9	249.5	4.093	4.121	0.028
0.1	63.1	32	207.2	126.9	603.4	248.8	4.027	4.058	0.030
0.29	63.1	32	207.2	126.9	572.1	252	3.770	3.71	-0.060
0.35	63.1	32	207.2	126.9	562.2	255	3.661	3.64	-0.021
0.4	63.1	32	207.2	126.9	554.0	256.7	3.584	3.624	0.040
0.44	63.1	32	207.2	126.9	547.4	260.3	3.492	3.55	0.058

Amount of *en* (x)	en^{2+}	FA$^+$	Pb^{2+}	I$^-$	FA(1-x)*en*(x)Pb(1-0.7x)I(3-0.4x) MW	Cell volume V(Å^3)	Calculated density (g cm^{-3})	Exp. Density (g cm^{-3})	Density difference
0	63.1	45.07	207.2	126.9	633	256.3	4.101	4.106	0.005
0.07	63.1	45.07	207.2	126.9	620.5	256.9	4.011	4.024	0.013
0.11	63.1	45.07	207.2	126.9	613.4	257.6	3.954	4	0.046
0.21	63.1	45.07	207.2	126.9	595.6	259.3	3.814	3.88	0.065
0.27	63.1	45.07	207.2	126.9	584.9	259.9	3.737	3.642	-0.095
0.39	63.1	45.07	207.2	126.9	563.6	262.0	3.573	3.62	0.047

EDX measurements
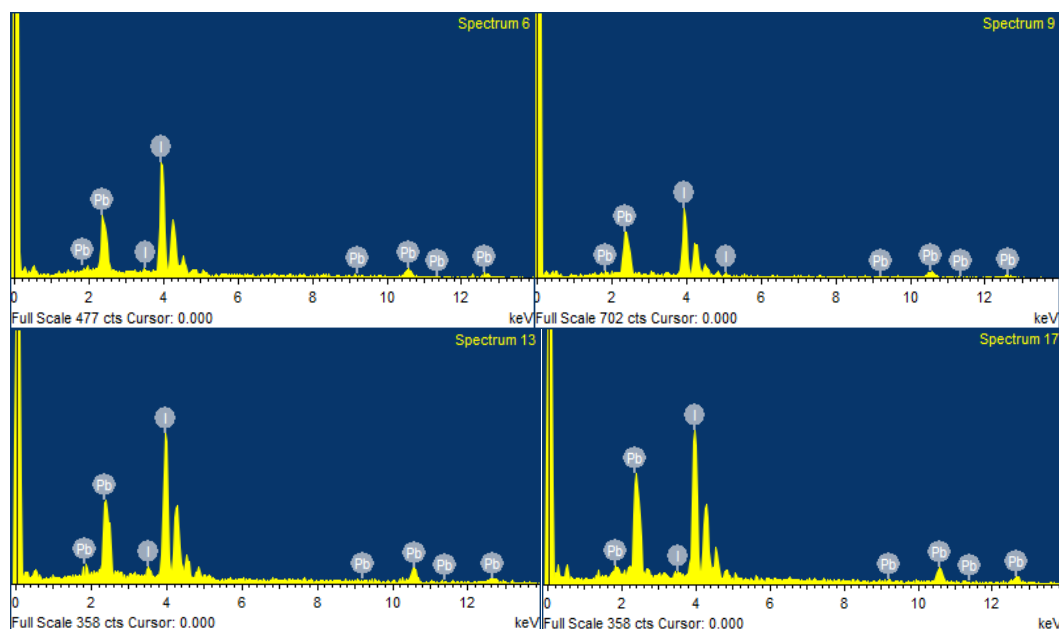
Figure S37. Representative EDX spectra of compounds $(FA)_{0.61}(en)_{0.39}(Pb)_{0.727}(I)_{2.844}$ (spectrum 6), α-FAPbI$_3$ (spectrum 9), $(MA)_{0.56}(en)_{0.44}(Pb)_{0.692}(I)_{2.824}$ (spectrum 13), and β-MAPbI$_3$ (spectrum 17).

Table S42. Quantitative EDX analysis table. The % atomic ratio for I and Pb was determined based on data collected on an average of 5 different sampling areas for each sample. The I/Pb ratio for the pristine materials FAPbI$_3$ and MAPbI$_3$ was found to be ~3 as it was expected from the crystal formula. However the most hollow *en* analogues exhibited a ratio of ~4 indicative of the lower amount of Pb in the structure.

Compound	Atomic % I (Lα)	Atomic % Pb (M)	Ratio I/ Pb
α-FAPbI$_3$	75.27	24.73	3.04
$(FA)_{0.61}(en)_{0.39}(Pb)_{0.727}(I)_{2.844}$	80.26	19.74	4.06
β-MAPbI$_3$	76.12	23.88	3.19
$(MA)_{0.56}(en)_{0.44}(Pb)_{0.692}(I)_{2.824}$	80.43	19.57	4.11

Thermogravimetric analysis

x = 0%
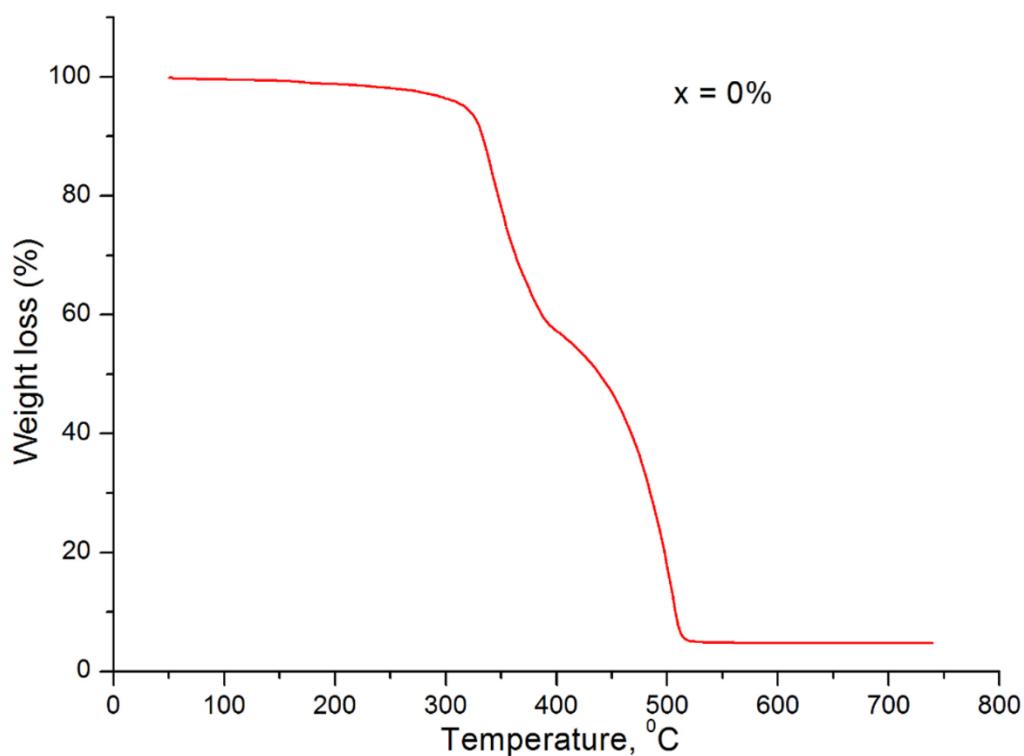
Figure S38. TGA curve for the compound with 0% nominal percentage of *en*, pristine MASnI$_3$ compound, recorded under helium flow with a heating rate of 8 deg/min.

x = 5%
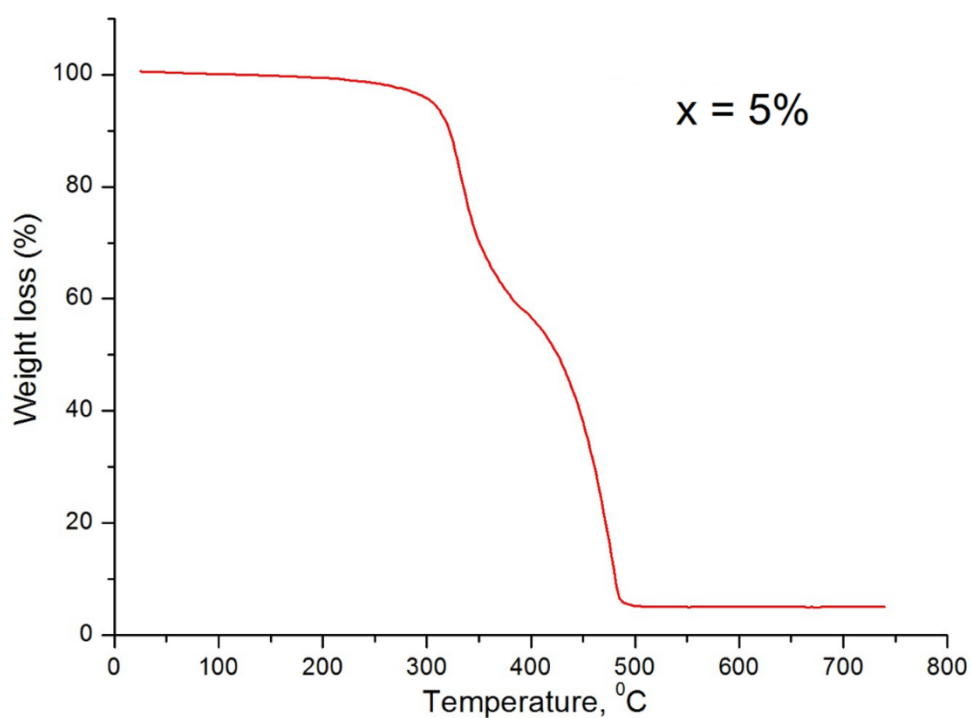
Figure S39. TGA curve for the (MA)$_{0.95}$(*en*)$_{0.05}$(Sn)$_{0.965}$(I)$_{2.98}$ compound recorded under helium flow with a heating rate of 8 deg/min.
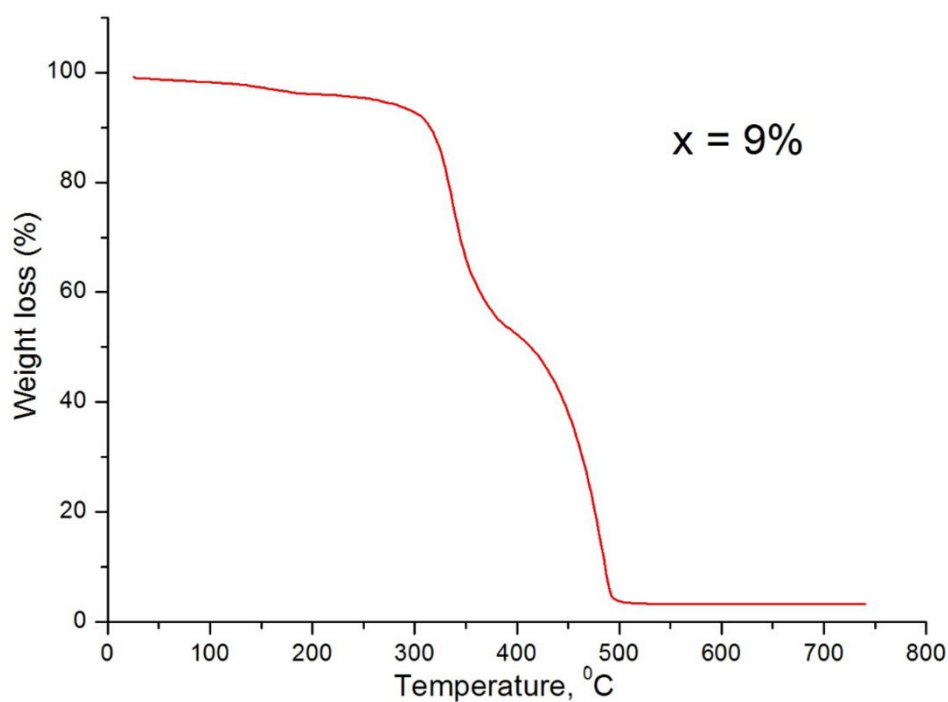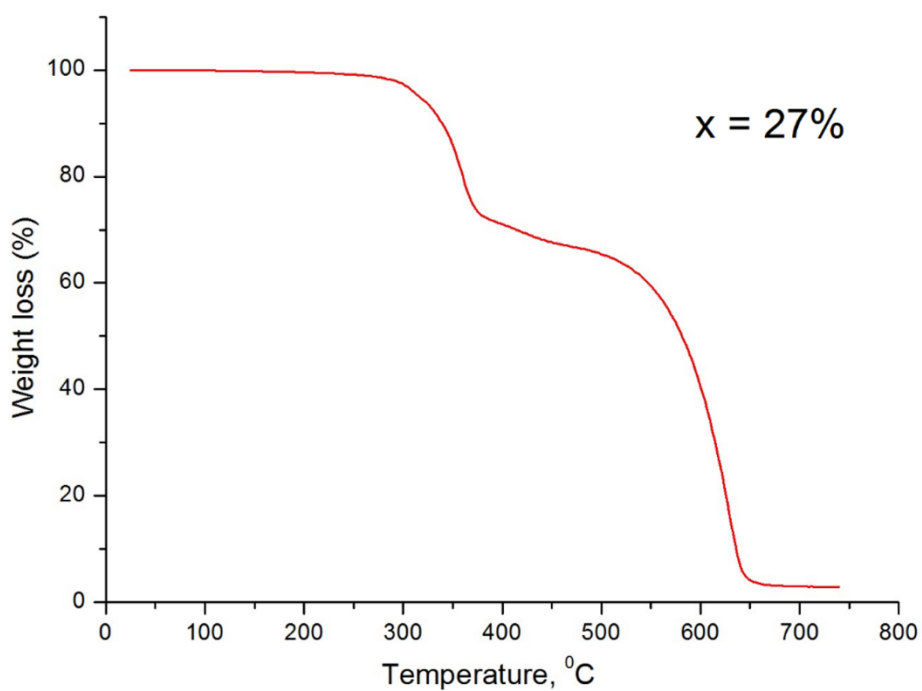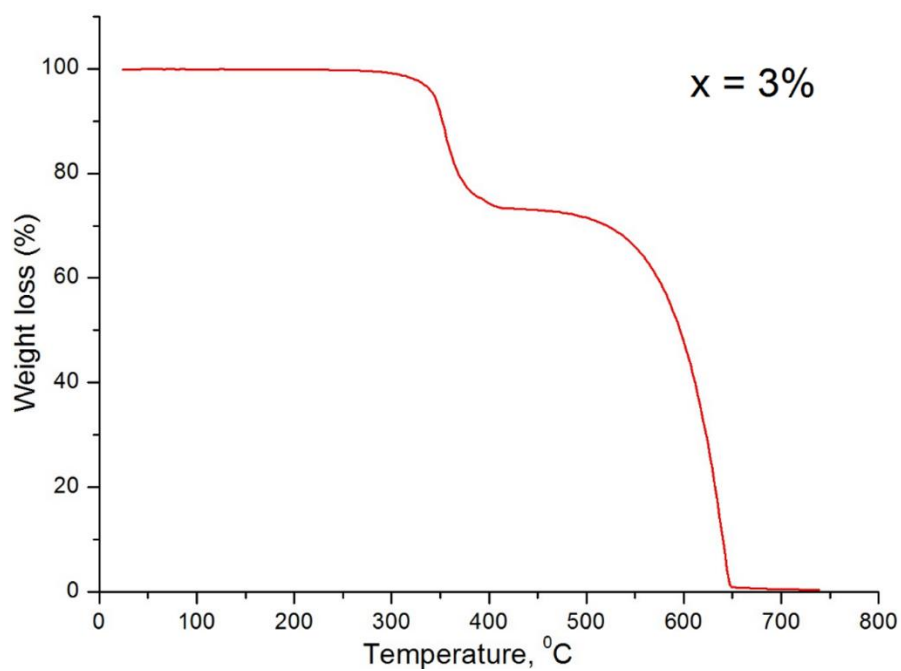
Figure S40. TGA curve for the $(MA)_{0.91}(en)_{0.09}(Sn)_{0.937}(I)_{2.964}$ compound recorded under helium flow with a heating rate of 8 deg/min.
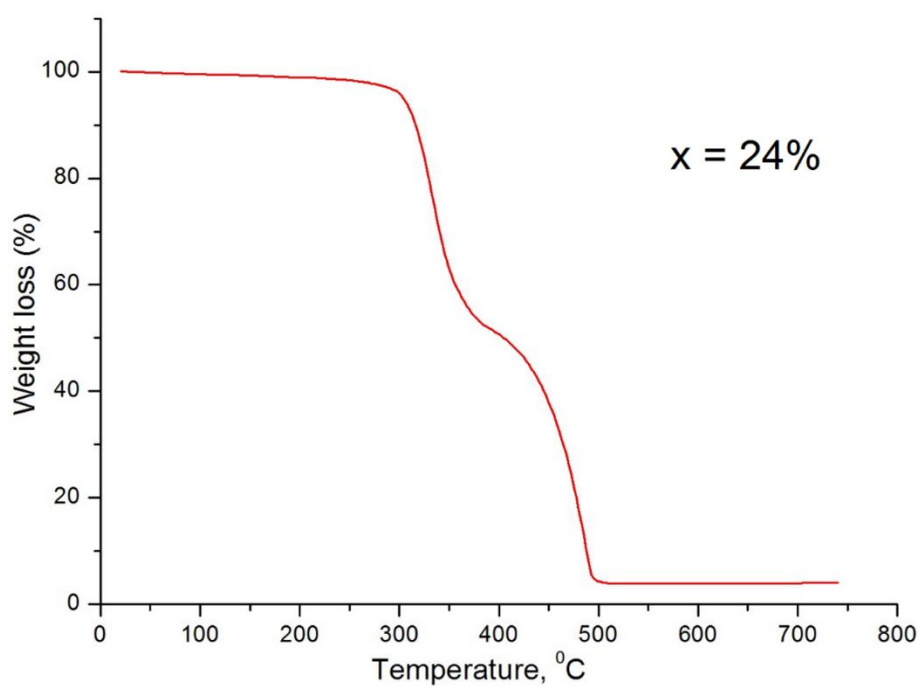
Figure S41. TGA curve for the $(MA)_{0.76}(en)_{0.24}(Sn)_{0.832}(I)_{2.904}$ compound recorded under helium flow with a heating rate of 8 deg/min.
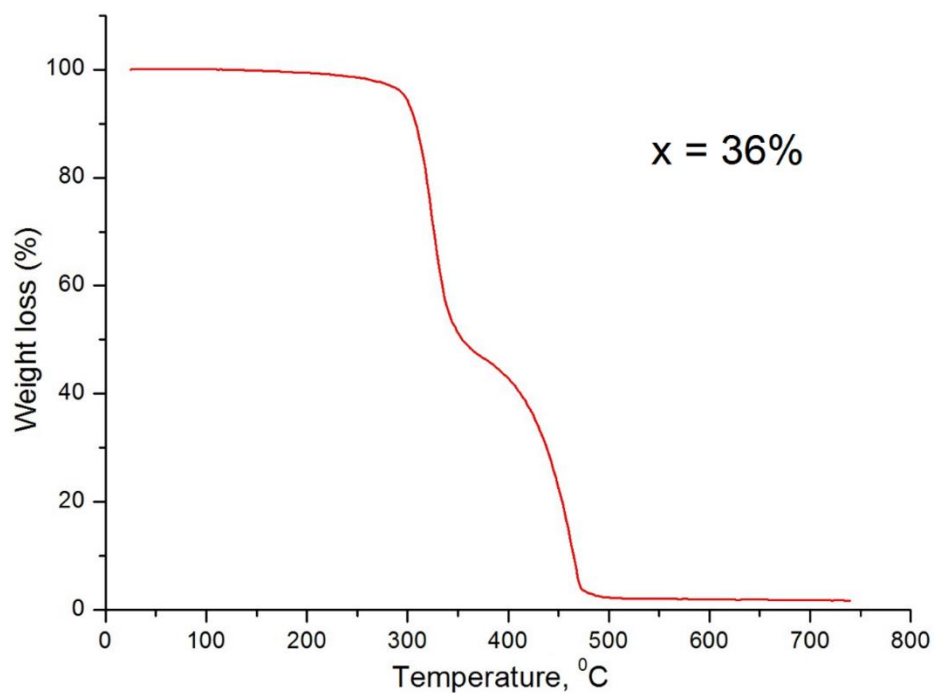
Figure S42. TGA curve for the $(MA)_{0.64}(en)_{0.36}(Sn)_{0.748}(I)_{2.856}$ compound recorded under helium flow with a heating rate of 8 deg/min.
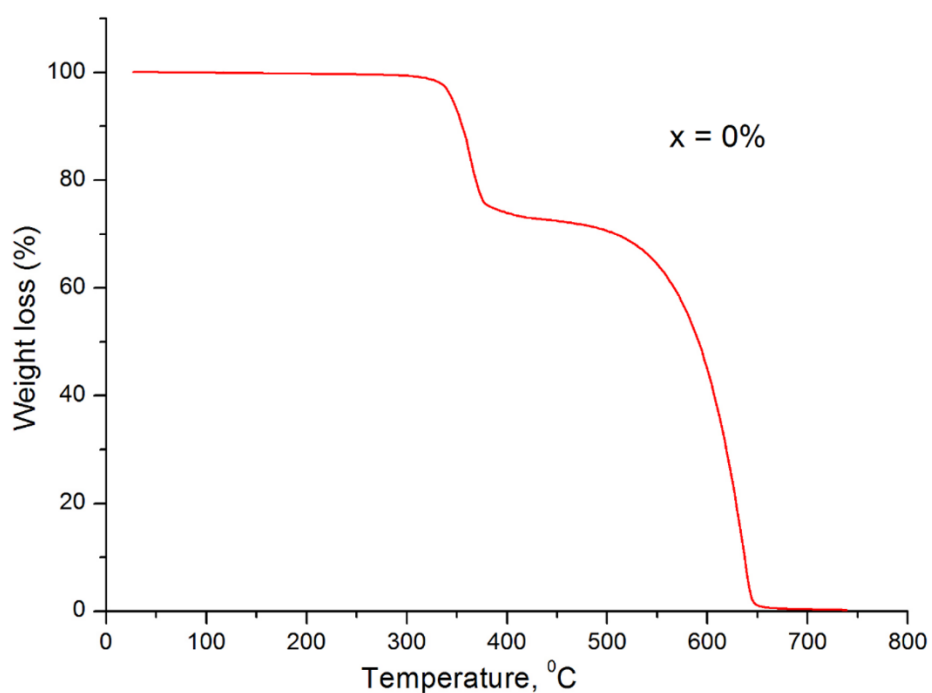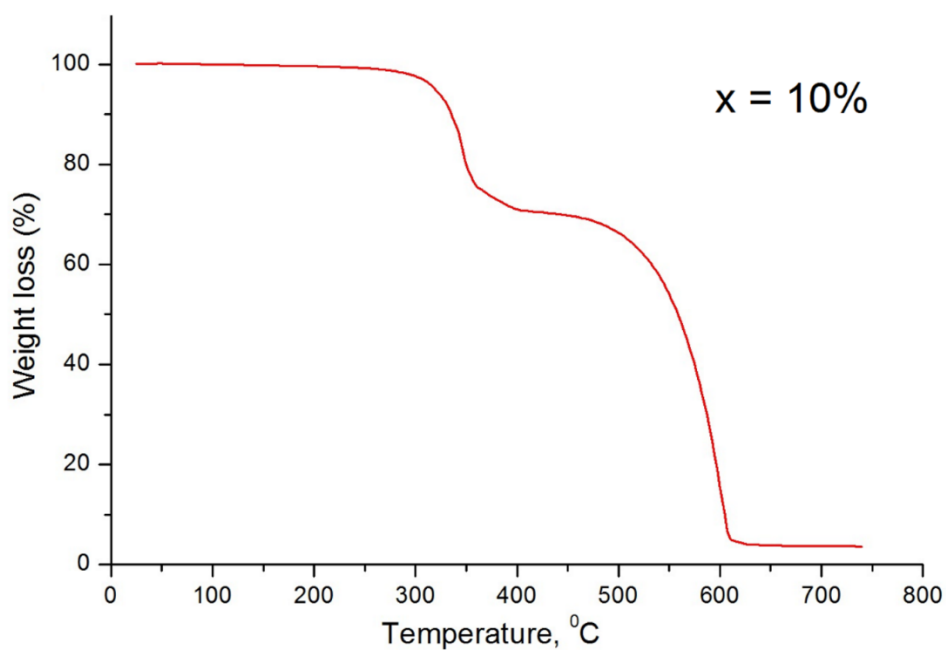

Figure S43. TGA curve for the pristine α-FAPbI$_3$ compound recorded under helium flow with a heating rate of 8 deg/min.
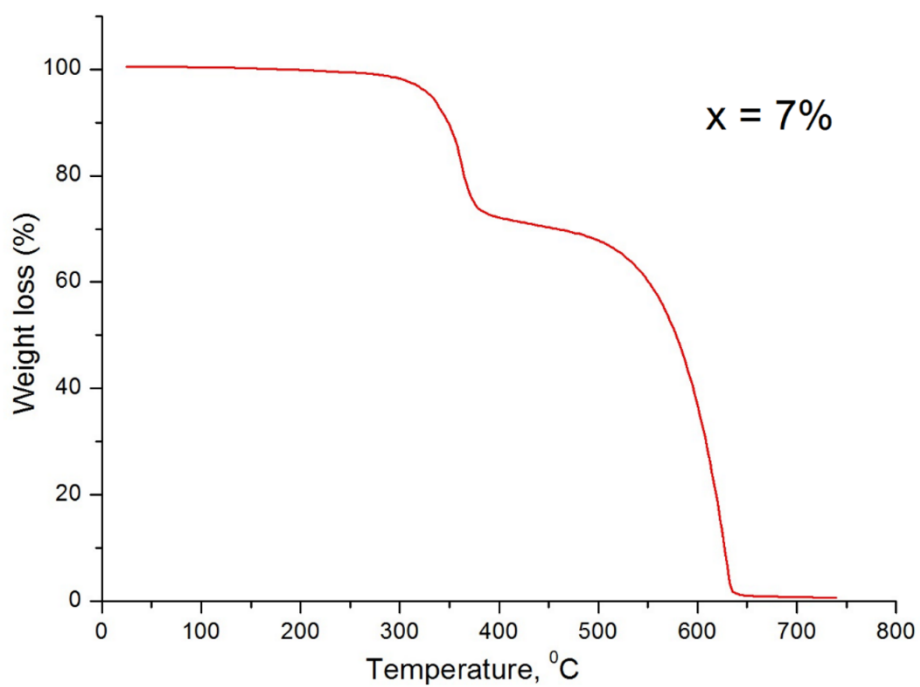
Figure S44. TGA curve for the $(FA)_{0.93}(en)_{0.07}(Pb)_{0.951}(I)_{2.972}$ compound recorded under helium flow with a heating rate of 8 deg/min.
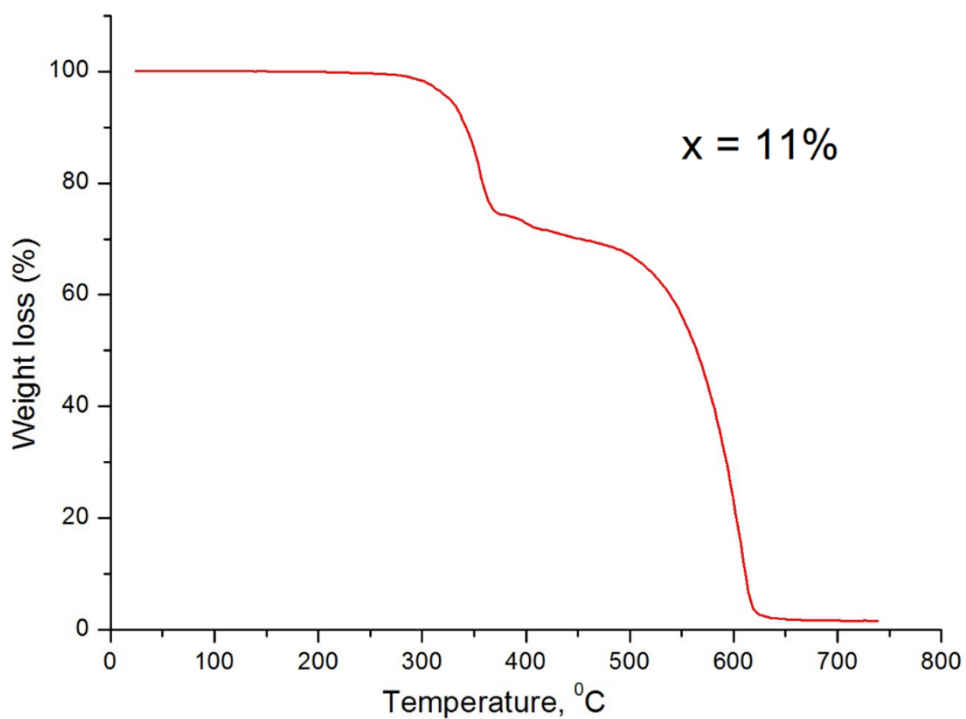
Figure S45. TGA curve for the $(FA)_{0.89}(en)_{0.11}(Pb)_{0.923}(I)_{2.956}$ compound recorded under helium flow with a heating rate of 8 deg/min.
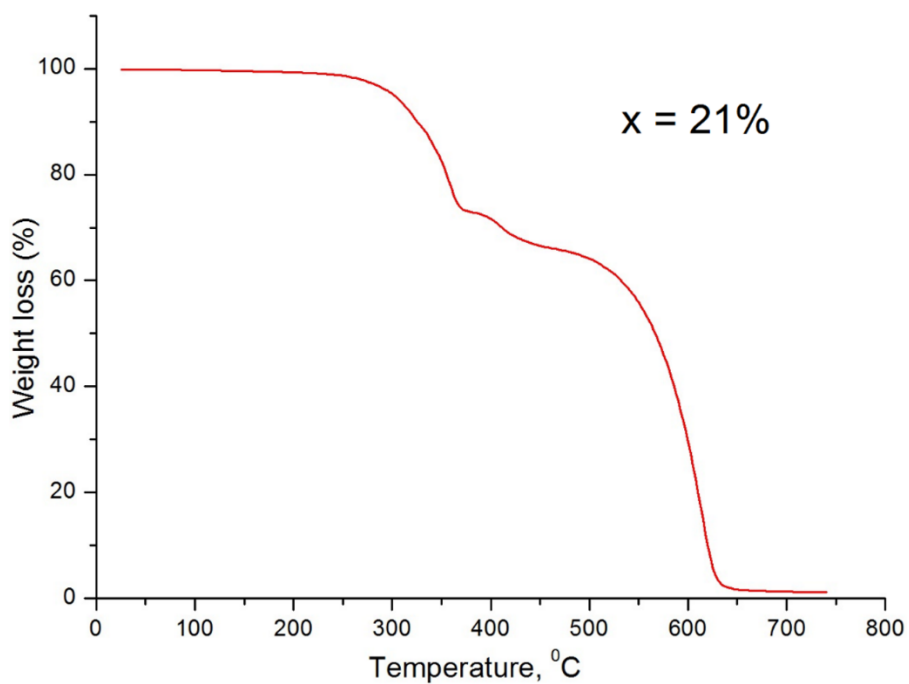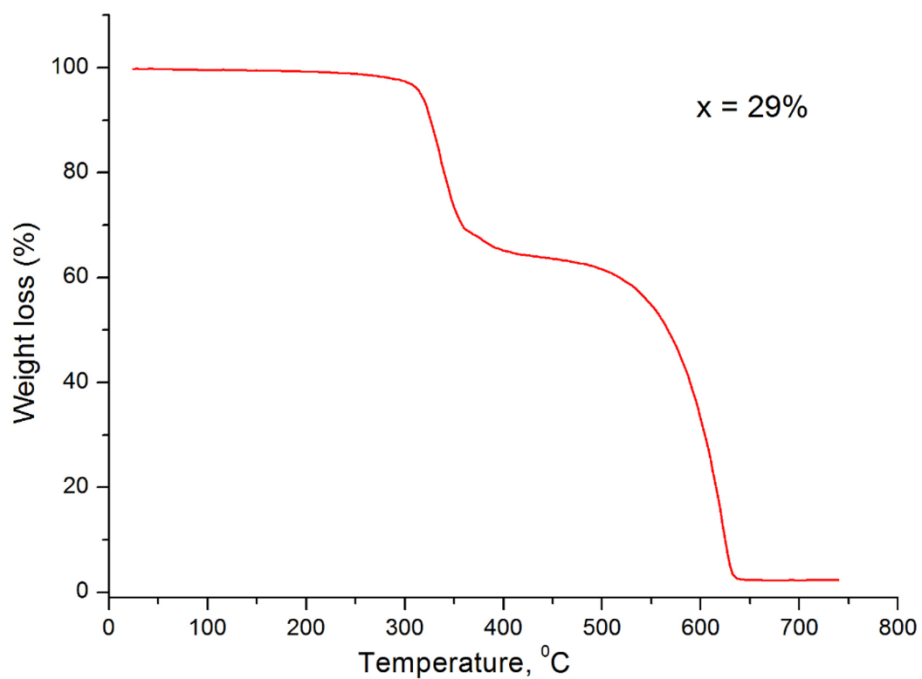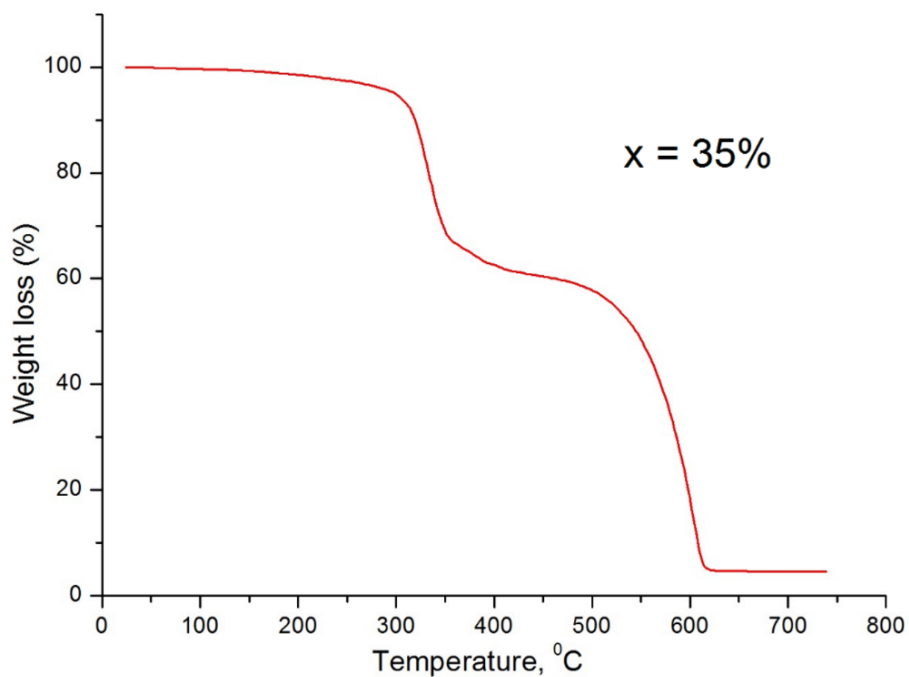
Figure S46. TGA curve for the $(FA)_{0.79}(en)_{0.21}(Pb)_{0.853}(I)_{2.916}$ compound recorded under helium flow with a heating rate of 8 deg/min.
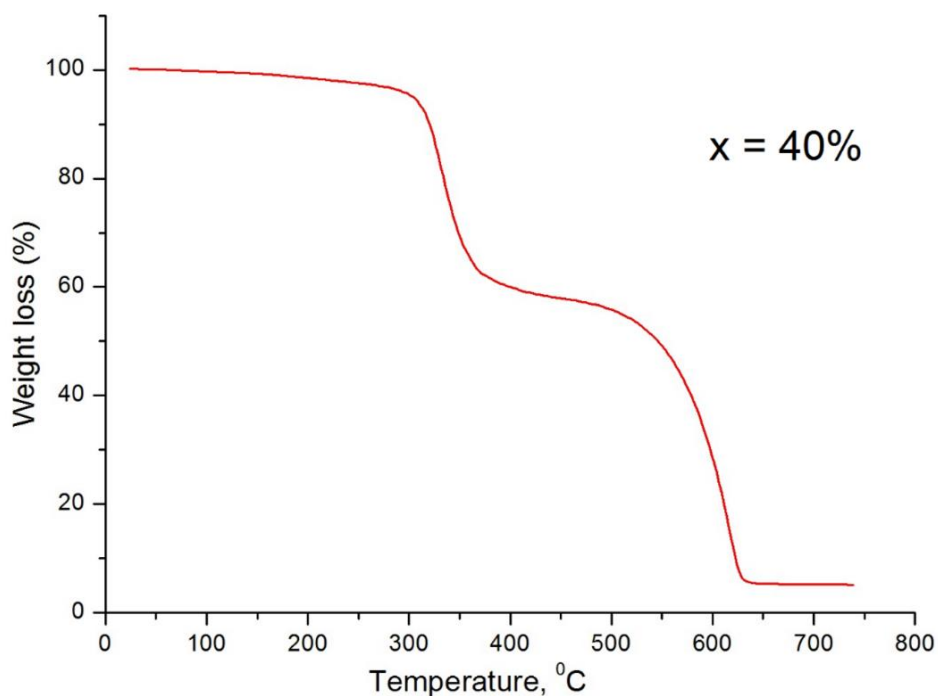

Figure S47. TGA curve for the $(FA)_{0.73}(en)_{0.27}(Pb)_{0.811}(I)_{2.892}$ compound recorded under helium flow with a heating rate of 8 deg/min.
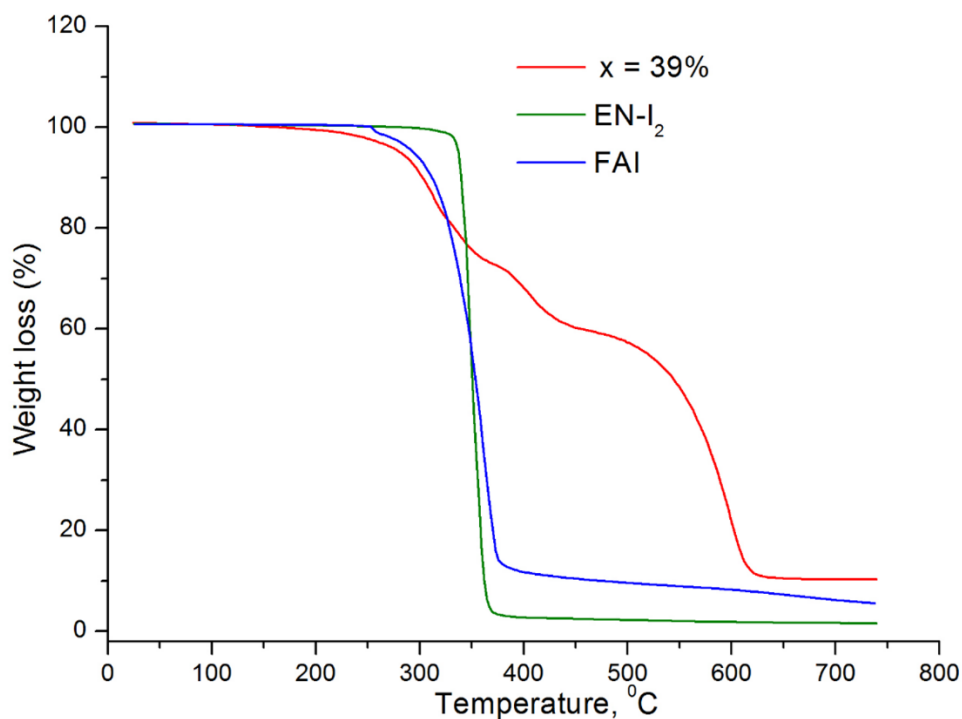
Figure S48. TGA curves for the $(FA)_{0.61}(en)_{0.39}(Pb)_{0.727}(I)_{2.844}$ compound, along with formamidinium iodide and ethylenediamonium iodide, recorded under helium flow with a heating rate of 8 deg/min.
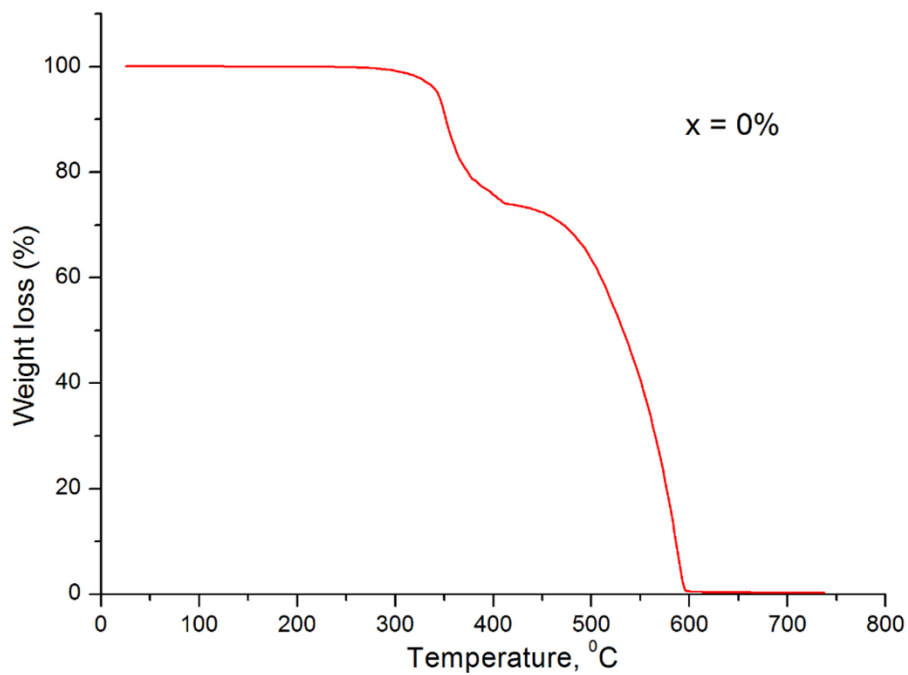
Figure S49. TGA curve for the pristine β-MAPbI$_3$ compound recorded under helium flow with a heating rate of 8 deg/min.

Figure S50. TGA curve for the $(MA)_{0.97}(en)_{0.03}(Pb)_{0.979}(I)_{2.988}$ compound recorded under helium flow with a heating rate of 8 deg/min.

Figure S51. TGA curve for the $(MA)_{0.9}(en)_{0.1}(Pb)_{0.93}(I)_{2.96}$ compound recorded under helium flow with a heating rate of 8 deg/min.

Figure S52. TGA curve for the $(MA)_{0.71}(en)_{0.29}(Pb)_{0.797}(I)_{2.884}$ compound recorded under helium flow with a heating rate of 8 deg/min.
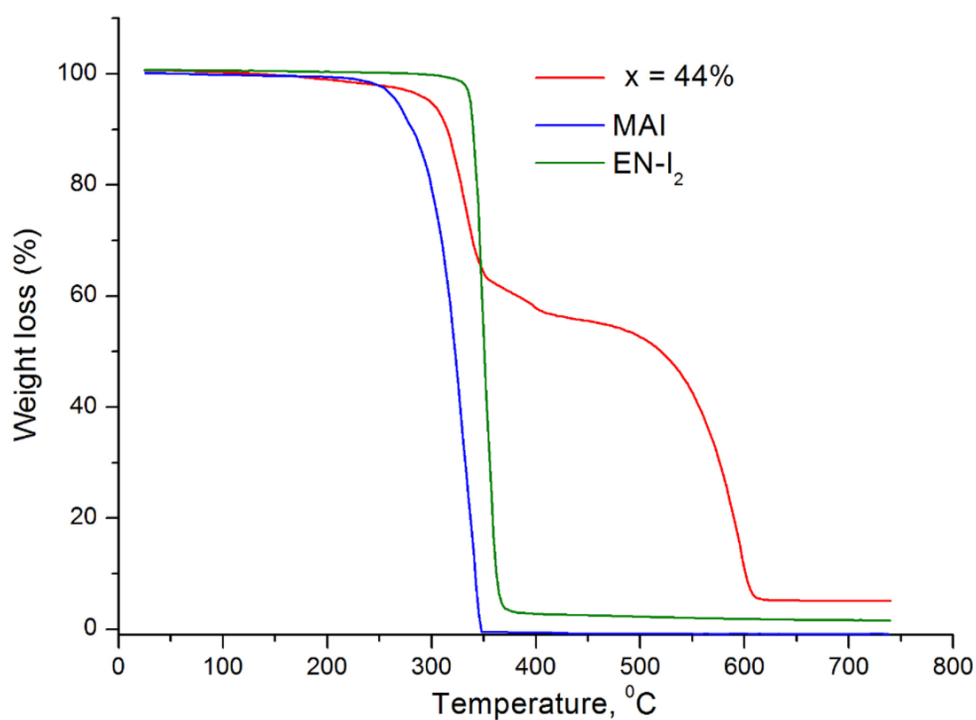

Figure S53. TGA curve for the $(MA)_{0.65}(en)_{0.35}(Pb)_{0.755}(I)_{2.86}$ compound recorded under helium flow with a heating rate of 8 deg/min.

Figure S54. TGA curve for the $(MA)_{0.6}(en)_{0.4}(Pb)_{0.72}(I)_{2.84}$ compound recorded under helium flow with a heating rate of 8 deg/min.

Figure S55. TGA curves for the $(MA)_{0.56}(en)_{0.44}(Pb)_{0.692}(I)_{2.824}$ compound, along with methyl ammonium iodide and ethylene diammonium iodide, recorded under helium flow with a heating rate of 8 deg/min.

Table S43. Correlation between the % weight loss of the organic and inorganic part of the $(MA)_{1-x}(en)_x(Sn)_{1-0.7x}(I)_{3-0.4x}$ compounds, along with the solid residue.

MASnI$_3$ + *en*%	MAI+ENI$_2$ loss%	SnI$_2$ loss%	residue %
0	45	50.3	4.7
5	46	49.1	4.9
9	49.1	47.6	3.3
24	50.1	45.5	4.4
36	55.7	42.3	2

Table S44. Correlation between the % weight loss of the organic and inorganic part of the $(FA)_{1-x}(en)_x(Pb)_{1-0.7x}(I)_{3-0.4x}$ compounds, along with the solid residue.

FAPbI$_3$ + *en*%	FAI+ENI$_2$ loss%	PbI$_2$ loss%	residue %
0	28	72	0
7	30	69.5	0.5
11	30.5	68	1.5
21	33.2	65.5	1.3
27	33.4	63.4	3.2
39	41.4	48.7	10.2

Table S45. Correlation between the % weight loss of the organic and inorganic part of the $(MA)_{1-x}(en)_x(Pb)_{1-0.7x}(I)_{3-0.4x}$ compounds, along with the solid residue.

MAPbI$_3$ + *en*%	MAI+ENI$_2$ loss%	PbI$_2$ loss%	residue %
0	26.5	73.5	0
3	27.3	72.4	0.3
10	30.3	66.5	3.2
29	36.3	61.2	2.5
35	39.6	55.9	4.5
40	41.9	52.9	5.2
44	44.6	50	5.4

PDF studies
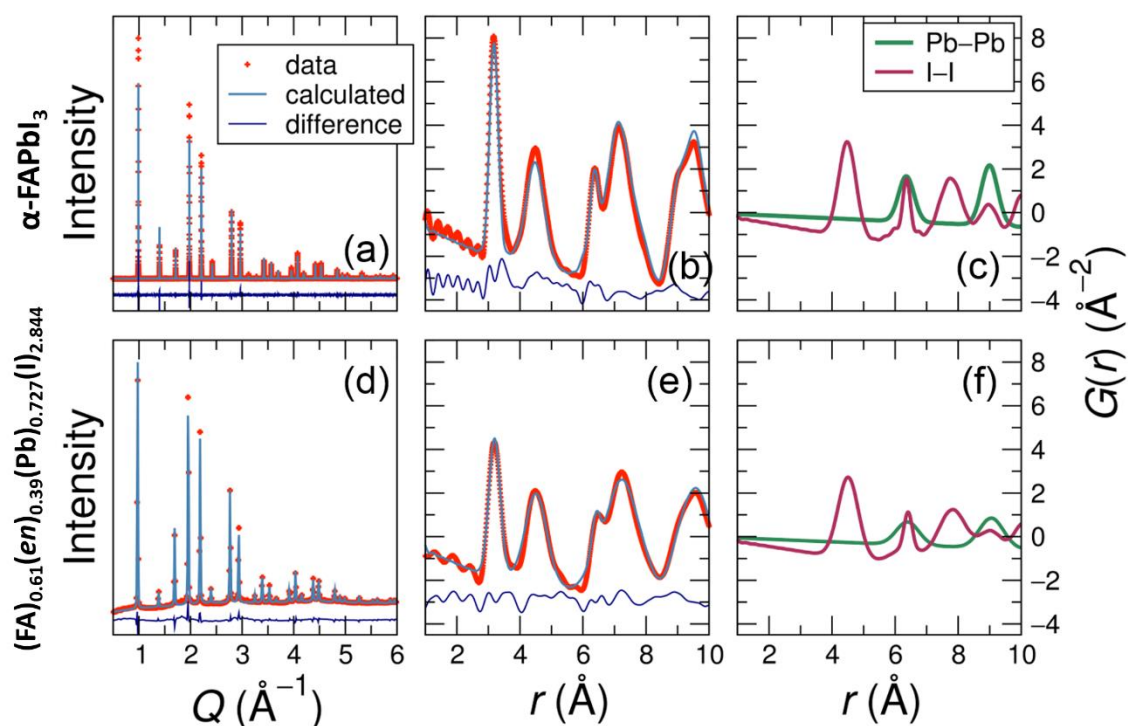
Figure S56. Experimental structure functions for the α-FAPbI$_3$ (a) and (FA)$_{0.61}$(*en*)$_{0.39}$(Pb)$_{0.727}$(I)$_{2.844}$ (d). Real space PDF refinement results, corresponding to the average structure of α-FAPbI$_3$ (b) and (FA)$_{0.61}$(*en*)$_{0.39}$(Pb)$_{0.727}$(I)$_{2.844}$ (e), Pb-Pb partial PDF (green line) and I-I partial PDF (red line) for the pristine (c) and the hollow material respectively (f).
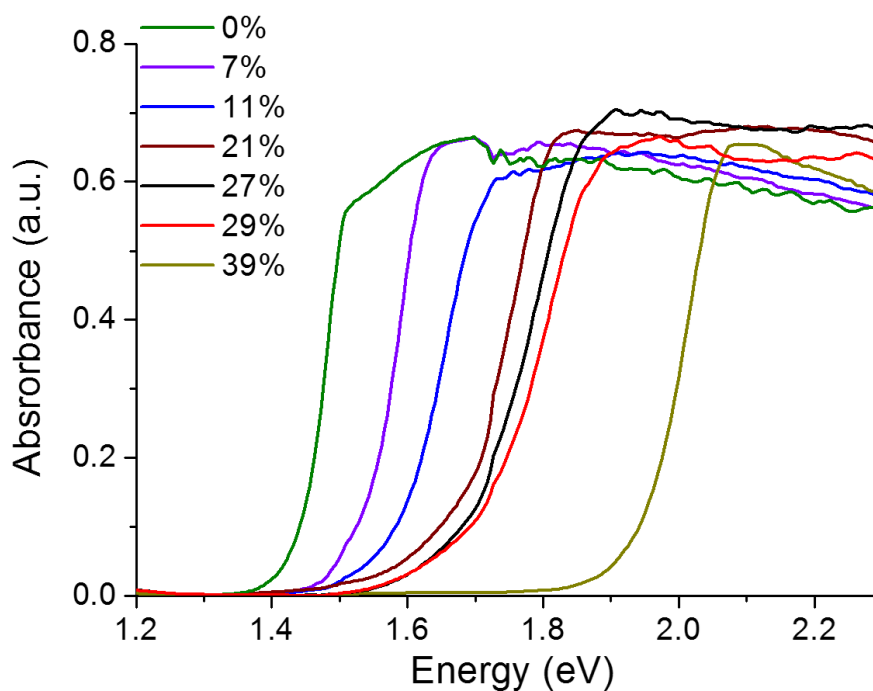
Absorption spectroscopy measurements

Figure S57. Optical absorption spectra of compounds $(FA)_{1-x}(en)_x(Pb)_{1-0.7x}(I)_{3-0.4x}$ with increasing amount of *en*, up to 39%.

Photoluminescence measurements
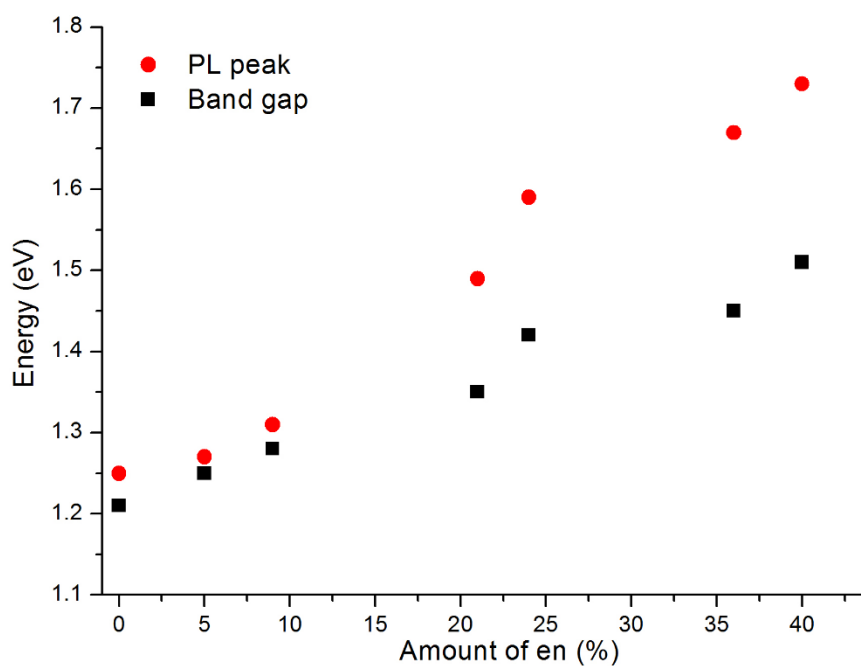
Figure S58. Correlation of the determined energy (eV) from the absorption and emission spectra of $(MA)_{1-x}(en)_x(Sn)_{1-0.7x}(I)_{3-0.4x}$ materials.
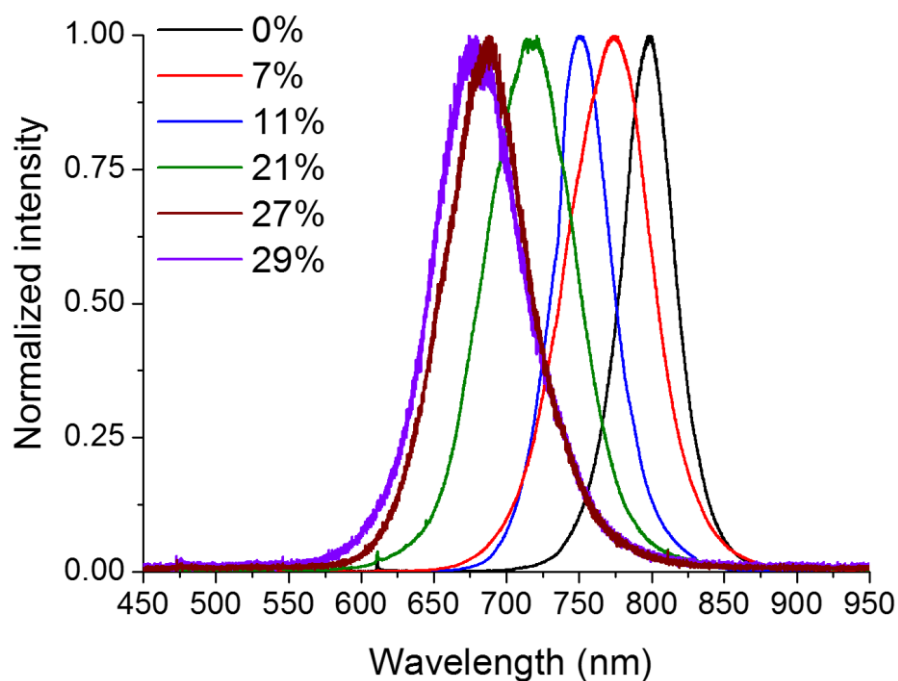
Figure S59. Photoluminescence spectra of $(FA)_{1-x}(en)_x(Pb)_{1-0.7x}(I)_{3-0.4x}$ materials. The increasing amount of *en* in the samples results into the shift of the PL peaks to lower wavelengths.
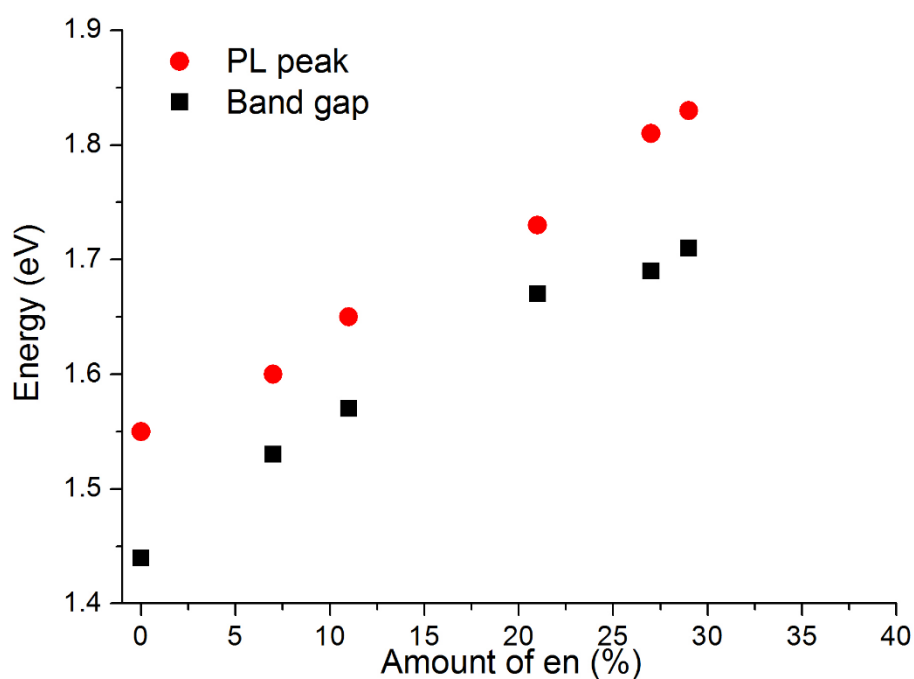

Figure S60. Correlation of the determined energy (eV) from the absorption and emission spectra of $(FA)_{1-x}(en)_x(Pb)_{1-0.7x}(I)_{3-0.4x}$ materials.
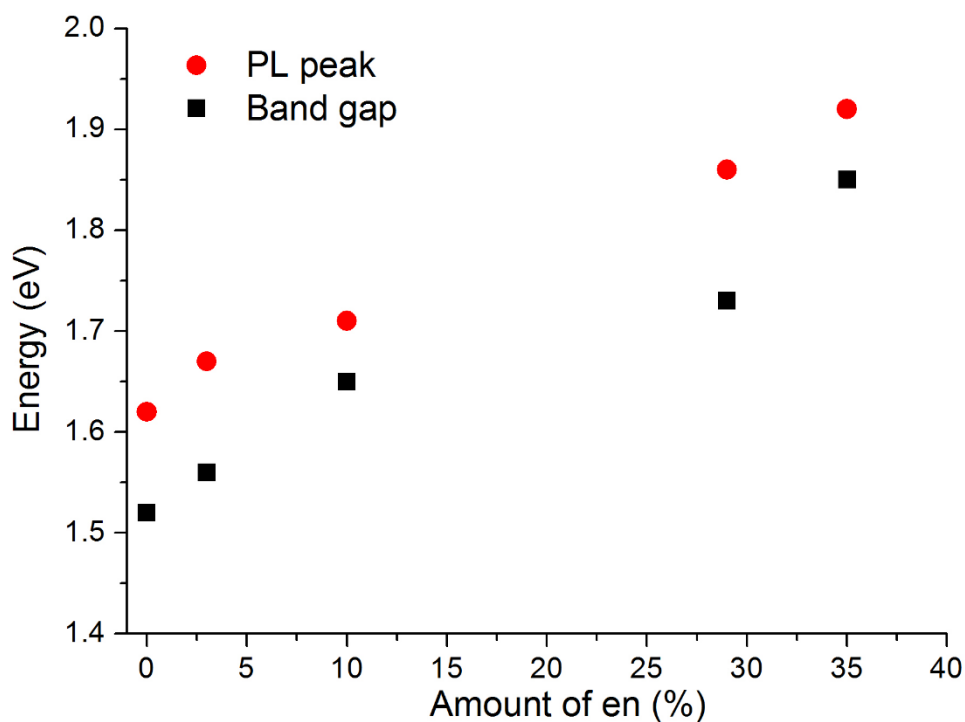
Figure S61. Correlation of the determined energy (eV) from the absorption and emission spectra of $(MA)_{1-x}(en)_x(Pb)_{1-0.7x}(I)_{3-0.4x}$ materials.

4. References

1. Petrícek, V.; Dušek, M.; Palatinus, L., *Z. Kristallogr.* **2014,** *229*, 345.
2. Toby, B., *J. Appl. Crystallogr.* **2005,** *38*, 1040.
3. Gate, L. F., *Appl. Opt.* **1974,** *13*, 236.
4. Prochowicz, D.; Franckevicius, M.; Cieslak, A. M.; Zakeeruddin, S. M.; Gratzel, M.; Lewinski, J., *J. Mater. Chem. A* **2015,** *3*, 20772.
5. Stoumpos, C. C.; Malliakas, C. D.; Kanatzidis, M. G., *Inorg. Chem.* **2013,** *52*, 9019.
6. Blöchl, P. E., *Phys. Rev. B* **1994,** *50*, 17953.
7. Kresse, G.; Furthmüller, J., *Phys. Rev. B* **1996,** *54*, 11169.
8. Perdew, J. P.; Burke, K.; Ernzerhof, M., *Phys. Rev. Lett.* **1996,** *77*, 3865.